Applications of Synthetic Aperture Radar Interferometry in the Study of the Nahanni Earthquake Region

by

Johannes P. Ristau

A Thesis Submitted to the Faculty of Graduate Studies in

Partial Fulfillment of the Requirements for the Degree of

MASTER OF SCIENCE (M. Sc.)

in Geophysics

Department of Geological Sciences

University of Manitoba

Winnipeg, Manitoba

THE UNIVERSITY OF MANITOBA

FACULTY OF GRADUATE STUDIES

*****

COPYRIGHT PERMISSION PAGE

Applications of Synthetic Aperture Radar Interferometry in the Study of the Nahanni Earthquake Region

BY

Johannes P. Ristau

A Thesis/Practicum submitted to the Faculty of Graduate Studies of The University of Manitoba in partial fulfillment of the requirements of the degree of Master of Science

For Kaitlyn and Zachary

Even though she's only six,

Katie promised to read the entire thing.

Table of Contents

Abstract

Two earthquakes of unprecedented magnitude ($M_s > 6.0$) occurred in late 1985 near the North Nahanni River in the Northwest Territories, Canada, and a third occurred in early 1988. These earthquakes were followed by extensive aftershock sequences. The earthquakes occurred within a small relatively undeformed plateau, the Mackenzie Plain, in the Foreland Fold Belt created along the northeastern Cordillera during the Columbian or Laramide Orogeny. The two major faults in the region are the Iverson Thrust Fault, located in the study area, and the Battlement Thrust Fault, located to the east of the study area.

In this thesis, Synthetic Aperture Radar (SAR) Interferometry (InSAR) is used to monitor ground displacement in the North Nahanni River region and create digital elevation models (DEM's). InSAR has been shown to be a valuable tool for monitoring relative surface displacement due to various crustal movements and for creating accurate DEM's using pairs of SAR images. In this thesis SAR data from Canada's RADARSAT and European Space Agency's ERS-1 satellites were used to create differential interferograms and DEM's. The main objectives of this study included measurement of fault slips caused by a large earthquake(s) with magnitude(s) larger than 6.0. However, there were no large earthquakes during the acquisition of the InSAR data pairs and therefore there was no detectable crustal movements caused by earthquakes. Consequently this study was more focused on the creation of accurate DEM's of the study area from the interferograms.

DEM's created from the RADARSAT and ERS-1 images were compared with a DEM provided by Geomatics Canada Centre for Topographic Information and 1:50 000 topographic maps of the Nahanni region. Comparison of a number of control points from each of the sources showed latitude values that were generally within 0.005° of each other and longitude values that were 0.01° of each other which amounts to errors of about 500 m. RMS errors were also calculated for flat areas in the RADARSAT and ERS-1 DEM's to see how close they remained to a constant value. The rms errors were around 5 m or less in both the RADARSAT and ERS-1 DEM's when the coherence between the two SAR images was around 0.20 or higher. This result shows that it is possible to create DEM's with errors of 5 m rms from interferometric data collected by RADARSAT or ERS-1 if the coherence is high enough.

Both two-pass and three-pass differential interferometry was attempted using ERS-1 and RADARSAT imagery. The two-pass differential interferograms created from ERS-1 and RADARSAT imagery showed potential for detecting surface movements even though the images available were not acquired under conditions favorable for interferometry. The three-pass differential interferogram created using ERS-1 imagery was extremely noisy and did not show the same potential for detecting surface displacement due to extremely low coherence between the ERS-1 images. There were encouraging signs however with the coherence between certain pairs of images being higher than expected. InSAR can be a valuable and effective too for studying remote ares such as the Nahanni region.

Acknowledgements

I would like to thank my advisor, Dr. Wooil Moon, for proposing this research topic and for his suggestions and encouragement during the completion of this thesis. I would also like to thank Dr. Ian Ferguson for taking the time to read this thesis and for all the helpful advice he has given me during my time in this department. Also thank you to Dr. W.H. Lehn for taking time to read this thesis.

Funding for this research came from an NSERC operating grant to W.M. Moon and by the Canadian Space Agency as part of the ADRO program #495. The RADARSAT data was provided by the Canadian Space Agency as part of the ADRO program.

I would also like to thank Dr. Paris Vachon at the Canada Centre for Remote Sensing for providing the ERS-1 and ERS-2 SAR data used in this thesis as well as providing valuable technical advice along the way. Also Bernie Armour at Atlantis Scientific provided many helpful troubleshooting suggestions for processing the InSAR data.

A special thanks to all my friends in the department and at the university in general, to those that are still here and those that have moved on. They have provided helpful suggestions and I've had alot of fun with them over the years and they are much appreciated. And finally to my family who have put up with me during my time at university and have always provided encouragement. Without them I could not have made it this far.

List of Figures

List of Tables

List of Symbols

A_i	Amplitude of SAR signal i
α	Tilt angle of SAR system
B	Baseline (orbital separation)
B_n	Normal component of the baseline
c	Speed of light
$\Delta\varphi$	Phase variation within the interferogram
δ	Path difference between two imaging locations
δf_a, δf_r	Frequency band shift in azimuth and range
$d\Phi$	Measured difference in phase between two points

dR	Change in range
dz	Change in surface height
F	Chirp bandwidth
F_A, F_R	Azimuth and range bandwidths
$g_i(x, y)$	Complex image i with azimuth and range coordinates (x, y)
I_o	Earthquake intensity
k	Radar wavenumber
L_a	Length of the antenna on a radar satellite
L_s	Length of synthetic aperture antenna
Λ	Lame's constant
λ	Radar wavelength
M	Earthquake moment
M_s	Surface wave magnitude
M_w	Revised magnitude

m_b	Body wave magnitude
Φ	Unwrapped phase
ϕ_i	Phase of SAR signal i
R	Range distance to the first point
ρ_a	Azimuth resolution
ρ_r	Slant range resolution
$\rho\varsigma$	Resolution cell size
$s(x, y)$	Interferogram produced from two SLC images
σ	Shear modulus
θ	Local incidence angle
θ_H	Angular spread of a real aperture radar beam
$\mathbf{u}$	Displacement field for the double-couple model
u	Surface slope in the plane of observation
u_{max}	Maximum slope that may be unambiguously measured

Υ_H	Spectral misalignment
$\Upsilon_{rotation}$	Rotation induced decorrelation
$\Upsilon(x, y)$	Coherence between two SLC images
$\frac{\partial \phi}{\partial R}$	Slope sensitivity for a given baseline

List of Acronyms

CCRS	Canada Centre for Remote Sensing
CNES	Centre National d'Etudes Spatiales (French Space Agency)
DEM	Digital Elevation Model
ERS-1/2	Earth Resources Satellite-1/2 launched by the European Space Agency
GPS	Global Positioning System
HCMM	Heat Capacity Mapping Mission
HH	Horizontal-Horizontal polarization mode
InSAR	SAR Interferometry or Interferometric SAR
JPL	Jet Propulsion Laboratory
LS	Least Squares

MM	Modified Mercalli (Scale)
PRF	Pulse Repetition Frequency
RADAR	RAdio Detection And Ranging
RADARSAT	Radar satellite launched by the Canadian Space Agency
RAR	Real Aperture Radar
SAR	Synthetic Aperture Radar
SCN	Scene (radar data)
SLC	Single Look Complex
SLR	Side Looking Radar
SPOT	Systeme Pour l'Observation de la Terre (French satellite)
TOPSAR	Topographic SAR
UCM	Unwrapping Control Mask
VV	Vertical-Vertical polarization mode

CHAPTER 1 Introduction

1.1 Introduction

Two earthquakes of unprecedented magnitude occurred in late 1985 near the North Nahanni River in the Northwest Territories, and a third took place in early 1988. These earthquakes were followed by extensive aftershock sequences. The earthquakes occurred within a small relatively undeformed plateau, the Mackenzie Plain, in the Foreland Fold Belt created along the northeastern Cordillera during the Columbian or Laramide Orogeny (Wetmiller et. al., 1988). The two major faults in the region are the Iverson Thrust Fault, located in the study area, and the Battlement Thrust Fault, located to the east of the study area (Moon et. al., 1991). These earth-

quakes generated a great deal of interest due to their unusually large magnitude (M > 6.0), and as an opportunity to study the characteristics and effects of large magnitude intraplate earthquakes in the northern Cordillera.

The epicentral region for the earthquakes is logistically difficult to access. The only access is by air with the closest community being Fort Simpson which is approximately 160 km to the east by air. Relatively few geological or geophysical surveys have been carried out in the region. For this reason remote sensing using satellites is ideal for studying the tectonic patterns and structure in the area. The resulting satellite information can be combined with other geophysical data such as seismological data sets in order to provide a better picture of the tectonic setting of the region. Li (1993) carried out a preliminary analysis of the Nahanni area using satellite images and seismic data and this thesis expands on that work using different techniques and newly available remote sensing platforms.

1.2 Remote Sensing Overview

Remote sensing involves obtaining images of the earth's surface using sensors on board an aircraft or spacecraft. The first type of sensors used for remote sensing were optical sensors which operate in the visual portion of the electromagnetic (e/m) spectrum. In terms of earthquake related studies, structural geological interpretation has traditionally been the most useful and common application for remote sensing images. Airphotos were used extensively for structural geological interpretations for decades to map linear features and other large scale

structures. Structural geological interpretations using spaceborne sensors began with Landsat-1 when Lowman (1976) made a structural geological interpretation of the San Andreas fault system using Landsat colour composite images.

Spaceborne radar remote sensing began when SEASAT was launched in 1978 and continued with the Shuttle Imaging Radar (SIR) missions in the early 1980's. The first earth-orbiting radar system intended for use on a commercial basis was the Almaz-1 satellite launched by the Soviet Union in 1991. Almaz-1 operated for 18 months before returning to earth in late 1992 (Lillesand & Kiefer, 1994). The 1990's have seen the launching of RADARSAT, ERS-1/ERS-2, and JERS-1 which have made synthetic aperture radar (SAR) images widely available and have opened up new possibilities for the use of remote sensing in geological applications (Lillesand & Kiefer, 1994).

The field of remote sensing has been rapidly progressing over the last few decades. It is now possible to combine digital satellite images and sophisticated processing techniques using powerful workstations in order to extract the maximum amount of information possible from the images. As a result, a number of significant advances have been made in the field of remote sensing. Of these, perhaps the most exciting is the recent discovery that synthetic aperture radar (SAR) images can be used to create very accurate digital elevation models (DEM's) and detect centimetre scale ground displacement. This is one application of SAR interferometry (InSAR).

Graham (1974) first showed that the phase measurement between airborne radar images could be used to produce topographic maps. In the early 1980's this technique was adopted to SEASAT radar images by the Jet Propulsion Laboratory (JPL) by taking the phase difference between two satellite images of the same location on the ground but taken at different times. Massonnet et. al., (1993) of the Centre National d'Etudes Spatiales (CNES) first demonstrated that SAR images could be used to detect centimetre scale ground displacement due to an earthquake. Since then InSAR has been used to detect and monitor crustal displacement due to earthquakes (i.e. Peltzer & Rosen, 1995), volcano inflation and deflation (i.e. Massonnet et. al., 1995), and glacier and ice movement (i.e. Vachon et. al., 1996).

InSAR is a method that is still in its infancy, but a number of significant advances have been made over the past several years that indicate InSAR can be an extremely valuable tool. With its ability to detect centimetre scale ground displacement, InSAR is an ideal method for monitoring earthquake activity in remote locations such as the North Nahanni River area. Since it has not yet been determined if InSAR can be effective in areas where the surface can change considerably over a short period of time, e.g. due to snowfall, part of the goal of this thesis is to determine the effectiveness of InSAR in an area where snowfall and surface vegetation changes are prevalent.

For this thesis, SAR data from RADARSAT (Canadian Space Agency), ERS-1 (European Space Agency), ERS-1/ERS-2 tandem mode, and JERS-1 (NASDA of Japan) were used. Each of the satellites has both advantages and disadvantages for use in InSAR and these affect the results in various ways. JERS-1(SAR) has the longest wavelength which means that

small changes on the ground surface will not affect the images to the same extent as the other platforms, but it has the longest repeat period (44 days) between image acquisition which means there is a much greater chance for changes to occur on the surface. RADARSAT has the best resolution of the satellites but it also has a fairly long repeat period (24 days). ERS-1 has a repeat period of 3, 35, or 168 days and has been used successfully in other studies to detect surface displacement. ERS-1/ERS-2 operating in tandem mode has only a one day repeat period however the chances of any earthquake related ground displacement occurring during the time window are very low.

1.3 Outline

In Chapter 2, earthquake theory is reviewed, focusing the elastic rebound theory and the double-couple model. Then the history of remote sensing in earthquakes related studies is briefly reviewed including airphotos, electro-optical satellite platforms, and SAR systems. Also the first instances of InSAR being used in earthquake related studies are discussed. In Chapter 3 the geologic setting of the North Nahanni River study area is described including the physiography, regional geological setting, structural geological setting, and stratigraphic setting. Then the previous earthquake activity and faulting mechanism in the area are reviewed.

Chapter 4 discusses the theory of SAR and InSAR. The geometry of the interferometric technique is described and the mathematical principles used for creating interferograms

and DEM's are discussed. Also the limits of the InSAR method are described along with the ways that these limits can be minimized. Finally a description of the different SAR platforms is presented. Chapters 5 and 6 describe the data processing techniques used for the SAR image formation and for creating interferograms and DEM's. A number of processing steps are required in order to generate interferograms and DEM's and these are described in detail. Chapter 7 presents the results, interpretation, and discussion, and Chapter 8 presents the conclusions of these studies.

CHAPTER 2

Earthquake Theory and Remote Sensing in Earthquake Research

2.1 Introduction

Earthquakes are one of the most powerful and devastating forces in nature. Earthquakes play a key role in building mountains over the course of millennia and are also capable of razing entire city blocks in a matter of seconds. As a result, earthquakes have been under intense scrutiny for centuries by both scientists and non-scientists alike. Unlike other natural disasters such as hurricanes or tornadoes it is virtually impossible to predict precisely where or when an earthquake will strike and how large it will be. As recently as the 1960's and early 1970's it was expected that after a decade or so of intensive research there would be a methodology in place

for predicting earthquakes. Scholz et. al. (1973) stated that "earthquake prediction...appears to be on the verge of practical reality...". Unfortunately the physical mechanism of earthquakes is not as simple as once thought and earthquake prediction is still far from reality.

Over the past few decades though great strides have been made in understanding the earthquake mechanism. The theory of plate tectonics for example has played a large role in understanding why most earthquakes occur where they do. Modern remote sensing satellites have opened up an entirely new realm of information gathering, and may contribute a great deal to further understanding the earthquake related tectonic precesses and perhaps, one day, towards a systematic methodology for predicting earthquakes.

2.2 Earthquake Mechanism

2.2.1 The Elastic Rebound Theory

Earthquakes are a result of rapid movement or slip along a fault. It is widely accepted that a shallow earthquake is shear faulting on a finite fault on which the rupture spreads with a finite velocity (Koyama, 1997). The central idea about the earthquake mechanism is the elastic rebound theory proposed by Reid (1911) to explain the 1906 San Francisco earthquake. The elastic rebound theory is shown diagrammatically in Figure 2.1. Reid (1911) proposed a slow, progressive buildup of elastic strain along a fault causing elastic deformation

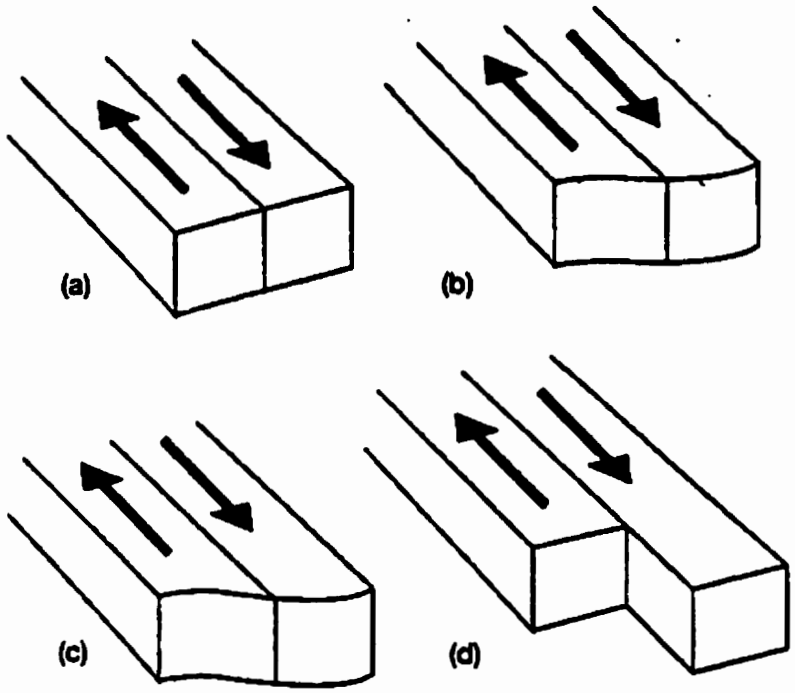

Figure 2.1 Sequence of events in the elastic rebound theory of an earthquake. Due to regional shearing movement, elastic strain is slowly built up from the unstrained state (**a**) to state (**c**) at which time it is suddenly released across the fault, producing displacement, as in (**d**), and releasing stored elastic energy (Stacey, 1992).

of the ground until a breaking point is reached. Displacement occurs across the fault due to the fracturing of the rocks with the only mass movements being the sudden elastic rebounds on the sides of the fracture toward positions of no elastic strain. The movements along the fracture are generally limited to distances of only a few kilometres from the fracture. The energy released at the time of the earthquake is initially in the form of elastic strain energy stored in the rock mass.

2.2.2 The Double-Couple Model

The elastic rebound theory is a somewhat simplistic theory particularly due to the concept of a breaking point. An earthquake may be considered to be a dynamically running shear crack (Scholz, 1990). For an arbitrarily oriented shear dislocation, alternating quadrants will exist in which static motions will occur and initial motions of the *P* wave arrival will be compressional (push) or dilatational (pull) as shown in Figure 2.2 (Lay & Wallace, 1995).

The simplest way to model an earthquake is as a single-couple model such as the one in Figure 2.3a. The single-couple model consists of two forces acting in opposite direction. The problem with the single-couple model is that it introduces a net unbalanced moment into the medium when the dislocation has occurred. Therefore the double-couple model, shown in Figure 2.3b, is the preferred model for a dislocation source. The double-couple model uses a second force couple to balance the moment of the force system so that no net moment is added to the medium, and so that the force couple is directed along the auxiliary

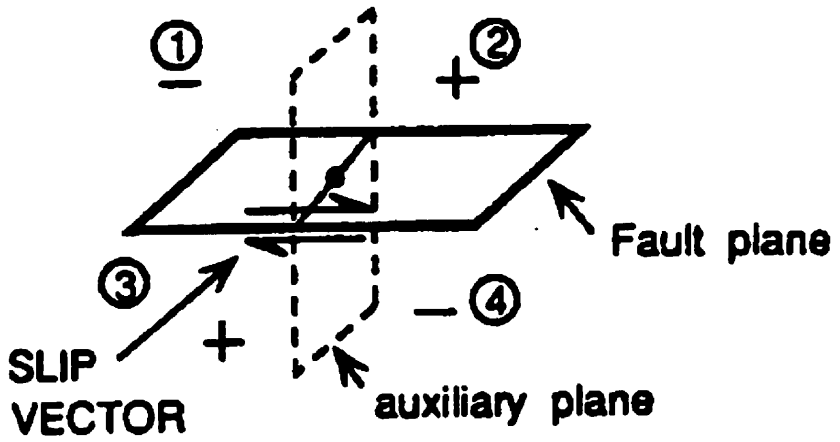

Figure 2.2 Sense of initial *P*-wave motion with respect to the fault plane and auxiliary plane (Lay & Wallace, 1995).

plane (Lay & Wallace, 1995). Figure 2.3c shows the equivalent force to a double-couple point force.

The displacement field $\bar{u}$ on a spherical surface for the double-couple model in the x_1x_2 plane as shown in Figure 2.4 can be described by the following equations

$$u_1 = \frac{M}{4\pi\mu r^2}\frac{x_2}{r}\left[1-\Gamma\left(1-\frac{3x_1^2}{r^2}\right)\right] \tag{2.1}$$

$$u_2 = \frac{M}{4\pi\mu r^2}\frac{x_1}{r}\left[1-\Gamma\left(1-\frac{3x_2^2}{r^2}\right)\right] \tag{2.2}$$

$$u_3 = \frac{M}{4\pi\mu r^2}\left(3\Gamma\frac{x_1x_2x_3}{r^3}\right) \tag{2.3}$$

where

$$\Gamma = \frac{\Lambda+\sigma}{\Lambda+2\sigma}, \tag{2.4}$$

σ is the shear modulus, Λ is Lame's constant, M is the moment, and r is the radius of the sphere, and

$$\bar{u} = (u_1, u_2, u_3). \tag{2.5}$$

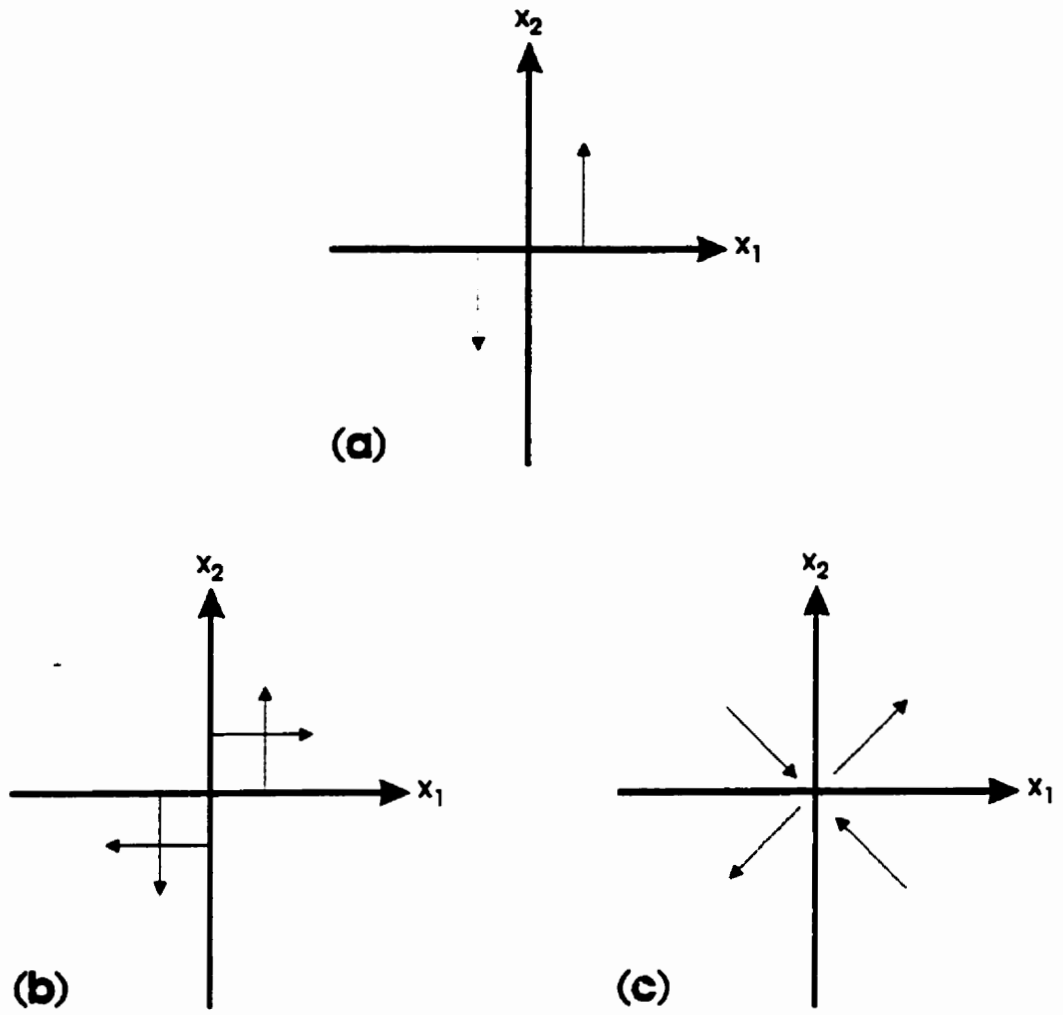

Figure 2.3 Orientation of (a) a single-couple force, (b) a double-couple force and, (c) the equivalent force to a double-couple point force. The smaller arrows represent force vectors (modified from Koyama, 1997).

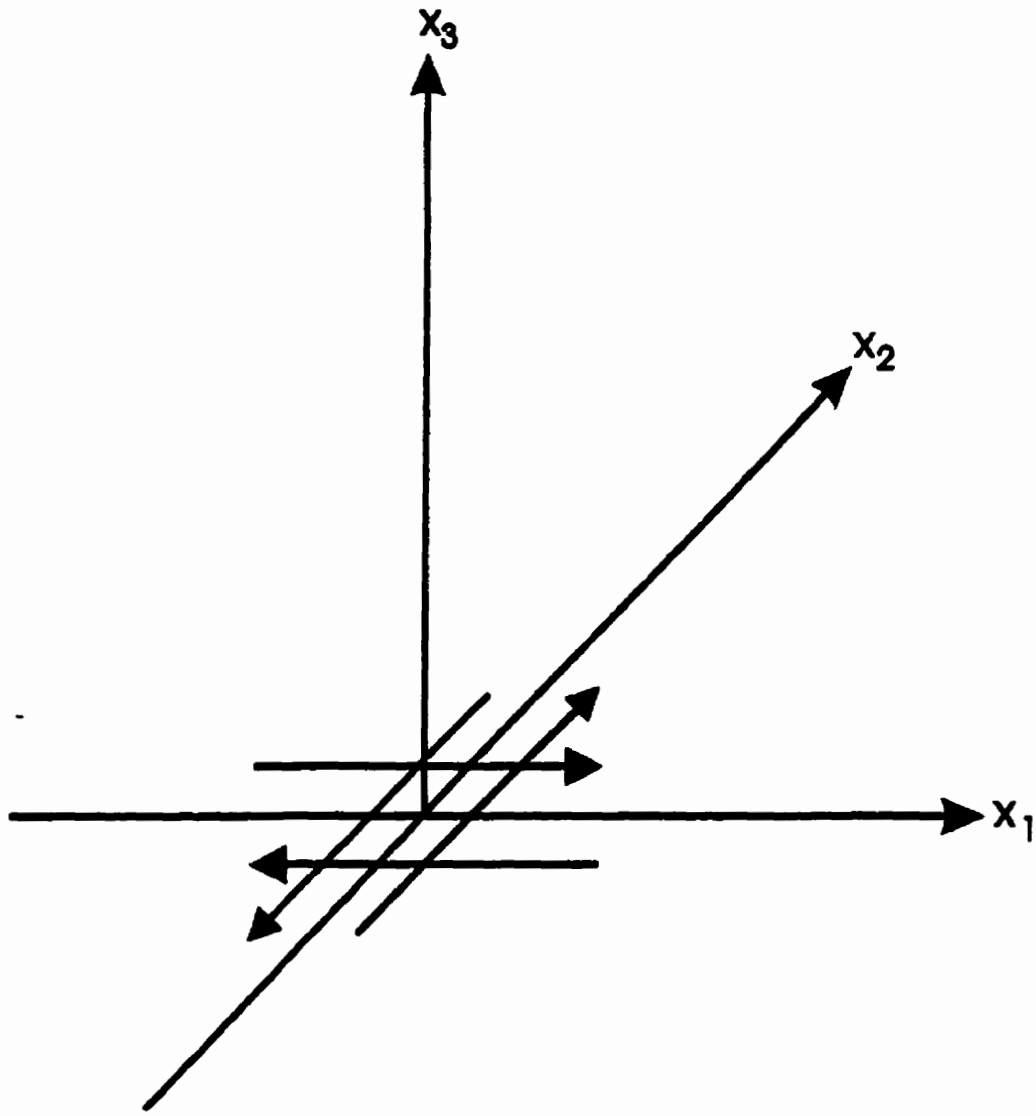

Figure 2.4 A double-couple in the x_1x_2 plane. The x_1 axis is along the slip direction, the x_2 axis is also in the plane of the fault, and x_3 is perpendicular to the fault (modified from Lay & Wallace, 1995).

Since the displacement field due to a shear dislocation can be given by the displacement field due to a distribution of equivalent double couples that are placed in a medium without any dislocations, these results can be used to calculate the deformation of the Earth around a slipped fault (Lay & Wallace, 1995).

2.3 Remote Sensing in Earthquake Research

2.3.1 Electromagnetic Spectrum

Before discussing remote sensing it is important to briefly review the electromagnetic spectrum. The electromagnetic (EM) spectrum represents a continuum across the wavelength or frequency of EM radiation. Figure 2.5 shows the major spectral bands that are important for remote sensing. The most important spectral bands for geological remote sensing are, in order of increasing wavelength, ultraviolet (UV), visible, infrared (IR), and microwave. The spectral band that is used will depend on the platform and the type of information required. The visible band is used for conventional airphotos or conventional photographs taken from orbiting spacecraft. The UV, visible, and IR bands are used in various combinations on electro-optical satellite platforms such as Landsat, SPOT (Systeme Pour l'Observation de la Terre), and the HCMM (Heat Capacity Mapping Mission). Since different geological materials interact differently with each of the spectral bands, much geological information can be obtained from combining information from the different bands.

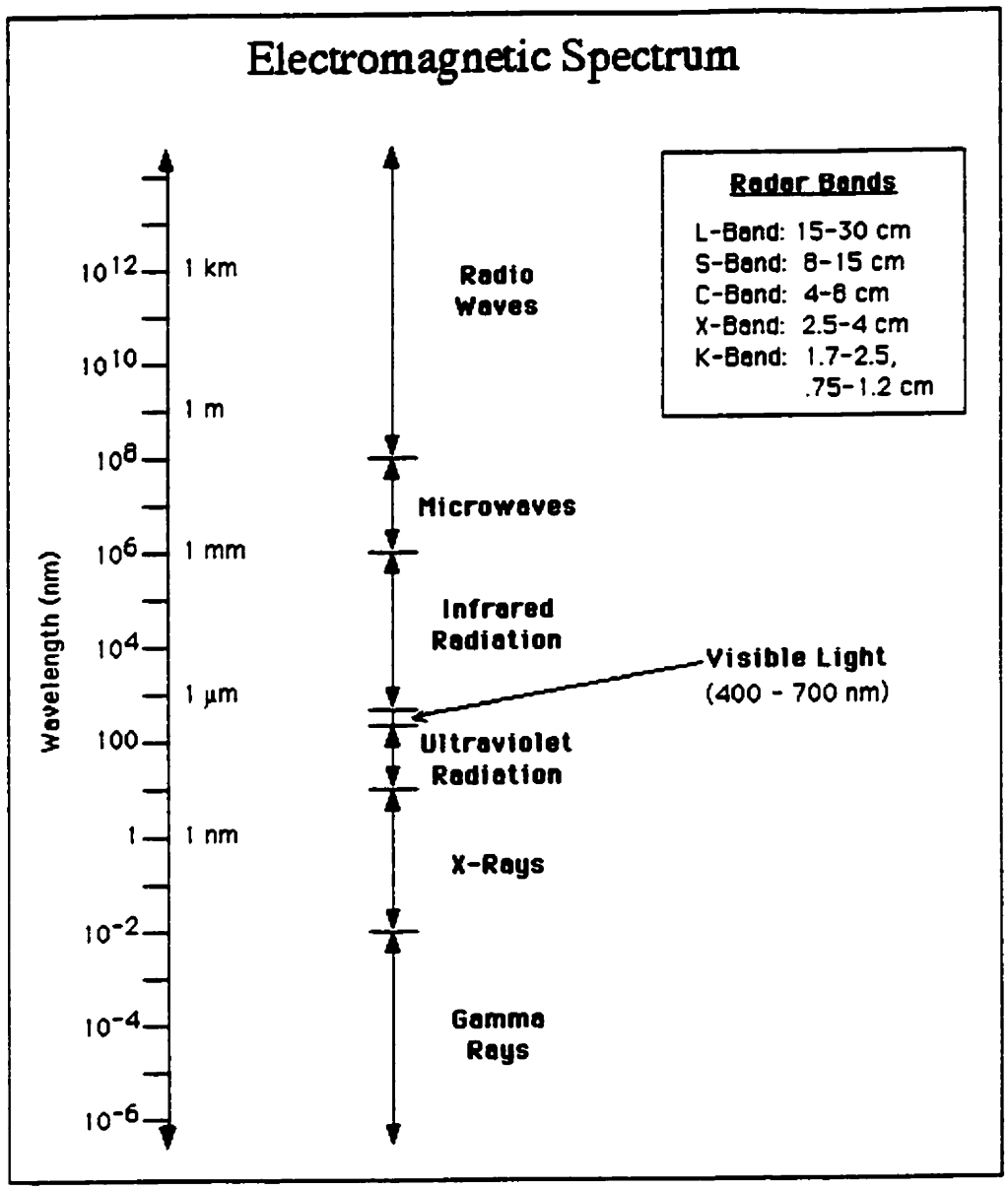

Figure 2.5 Major electromagnetic spectral regions pertinent to remote sensing (Alaska SAR Facility, 1996a).

UV, visible, and IR radiation cannot penetrate clouds and are often completely obscured by rain and snow which limits its usefulness under these conditions. Also sensors for these wavelengths rely on reflected sunlight so images cannot be obtained at night. Microwave radiation is not affected by clouds, rain, or snow, and most platforms that utilize microwave radiation generate their own signal which means they can be used day or night. The microwave band is used by radar satellites such as RADARSAT, ERS-1/ERS-2, and JERS-1. Since using SAR is essential to this thesis, the focus of further discussion will be on microwave radiation and SAR.

2.3.2 - Aerial Photographs

Remote sensing is defined as the technique of obtaining information about objects through the analysis of data collected by special instruments that are not in physical contact with the objects of investigation (Avery & Berlin, 1992). In the geological sense, remote sensing refers to measuring or monitoring various physical and/or chemical features and processes on the surface of the earth and in the atmosphere. Traditionally studying earthquakes by remote sensing involved identifying linear features such as faults on the surface by way of airphotos. Mapping lineaments on remote sensing imagery is, however, only an effective procedure for recognizing *possible* faults. O'Leary et. al. (1976) define a lineament as a "mappable, simple, or composite feature of a surface whose parts are aligned in a rectilinear or slightly

curvilinear relationship and which differs distinctly from the pattern of adjacent features and presumably reflects a subsurface phenomenon." Aerial photographs are also subject to constraints dealing with weather and the logistics associated with flying over a particular area.

2.3.3 Satellite Images

Optical Satellites

The first space image of the earth using optical sensors was collected by Explorer-6 in August, 1959 and in 1960 the first orbital photography became available (Lowman et. al., 1967). During NASA's space program of the 1960's and early 1970's (Mercury, Gemini, and Apollo missions), remote sensing from space developed from using simple hand held cameras to using a four-camera array to acquire multispectral photographs (Lillesand & Kiefer, 1994). In 1973, Skylab was launched and took over 35 000 image of the earth with the Earth Resources Experiment Package (EREP) on board. The EREP included a six-camera multispectral array, a long focal length earth terrain camera, a 13-channel multispectral scanner, and two microwave systems (Lillesand & Kiefer, 1994)

Landsat-1, launched in 1972, became the first unmanned satellite specifically designed to acquire data about earth resources on a systematic, repetitive medium resolution, multispectral basis (Lillesand & Kiefer, 1994). The Landsat series uses electro-optical sensors which convert the reflected and/or emitted radiation from a ground scene to proportional electrical signals that are ultimately used to construct 2-D images for conventional viewing. Elec-

tro-optical sensors are non-film detectors (Avery & Berlin, 1992). Five other satellites in the Landsat series have been launched and Landsat-7 is in the planning stages. The CNES launched SPOT-1 in 1986 which also used electro-optical sensors and led to the launch of 4 other satellites in the series.

SAR History

Remote sensing using radar began with side-looking radar which was developed for military reconnaissance in the early 1950's, and the first large-scale terrain mapping project was a complete survey of the Darien province of Panama in 1967 using airborne radar (Lewis, 1976). The era of space-borne radar remote sensing began with the launch of SEASAT-1 in 1978. SEASAT-1 was the first of a proposed series of satellites oriented towards oceanographic research. System failure 105 days after launch ended the mission and no further satellites in the series were ever launched (Lillesand & Kiefer, 1994). NASA's SIR (Shuttle Imaging Radar) missions took place during November 1991 and October 1994. These were designed to be more experimental missions to test the potential of radar remote sensing systems and determine the effects of different parameters such as varying look angles (Lillesand & Kiefer, 1994).

Almaz-1, launched by the former Soviet Union in early 1991, was the first earth-orbiting radar satellite to operate on a commercial basis. The Almaz-1 mission ended 18 months later when the satellite returned to earth (Lillesand & Kiefer, 1994). In the 1990's

RADARSAT, ERS-1/ERS-2, and JERS-1 have been launched which have initiated a new era in the availability of SAR imagery (Lillesand & Kiefer, 1994).

Satellite Images for Geological Interpretation

The first colour composite image produced from Landsat-1 data was over the Monterey Bay area, California and the structural geological interpretation was made by Lowman (1976). His results provided an important view of the San Andreas fault system and gave a better understanding of the tectonic setting associated with earthquakes and associated seismic activities. Remote sensing studies of the North Nahanni study area have been previously carried out by Li (1993) using SPOT, CCRS-airborne C-SAR, Landsat MSS, and JERS-1 SAR data. SAR sensors have a limited capability for penetration into the surface. Under certain conditions, and if the frequency of the radar wave is sufficiently low, penetration through dry surficial materials of up to 4 m has been reported e.g. Cannon (1980) and McCauley et. al. (1982). This means that SAR images are limited to examining surface or near-surface structures. However, with the increasing spatial resolution of satellite remote sensing platforms, satellite images have become useful in earthquake investigations.

As is the case with aerial photographs, both the Lowman (1976) and Li (1993) studies focused on picking linear features on the surface and identifying faults. As mentioned in section 2.2, earthquakes are caused by a slow, progressive buildup of elastic strain along a fault which is suddenly released. The deformation associated with the elastic strain buildup is normally not very large and therefore monitoring the deformation by only examining structural

features on a satellite image can be exceedingly difficult, if not impossible. Normally sophisticated measuring equipment must be in place on the surface before-hand in order the measure the deformation associated with the elastic strain build-up.

Recently SAR interferometry (InSAR) has become popular for studying potential earthquake regions. Graham (1974) first demonstrated that it was possible to take advantage of the phase measured by airborne radar. In the early 1980's, scientists at JPL showed that they could extract similar results by measuring the phase from Seasat-1 SAR data. This was accomplished by comparing two radar images taken of the same area on the ground but at different times. Although the phase appeared random every time, the phase differences between corresponding pixels in the two radar images produced a relatively straightforward interference pattern (Massonnet, 1997).

The first application of InSAR for detecting small scale displacements due to an earthquake was carried out by Massonnet et. al. (1993) of the CNES to detect surface displacement due to the June 28, 1992 earthquake near Landers, California (M_s 7.3). The French group at CNES used ERS-1 SAR data over the epicentral area to map co-seismic and some post-seismic deformation with a resolution of 34 mm. A DEM of the area was used to calculate and remove the topographic effect. Since then InSAR has become a common tool for monitoring tectonic activity e.g. Massonnet et al. (1996), Meyer et al. (1996), Massonnet & Feigl (1995), and Peltzer & Rosen (1995).

CHAPTER 3

Geologic Setting and Earthquake Activities in the North Nahanni River Study Area

3.1 Introduction

The study area is located in the southwestern NWT between longitudes 122°W and 128°W, and latitudes 61°N and 64°N (Figure 3.1). Figure 3.2 shows a more detailed map of the study area with many of the lakes and rivers. The epicentral area is logistically difficult to access. Access is limited to helicopter or small fixed wing aircraft. The area is mountainous and heavily forested, and there are no nearby communities. The closest community is Fort Simpson which is approximately 160 km to the east by air. Earthquakes with magnitudes lower than 6 have occurred frequently in

★ Location of North Nahanni River study area

N

Figure 3.1 Location of the North Nahanni River study area.

North Nahanni and Mackenzie River Map Area

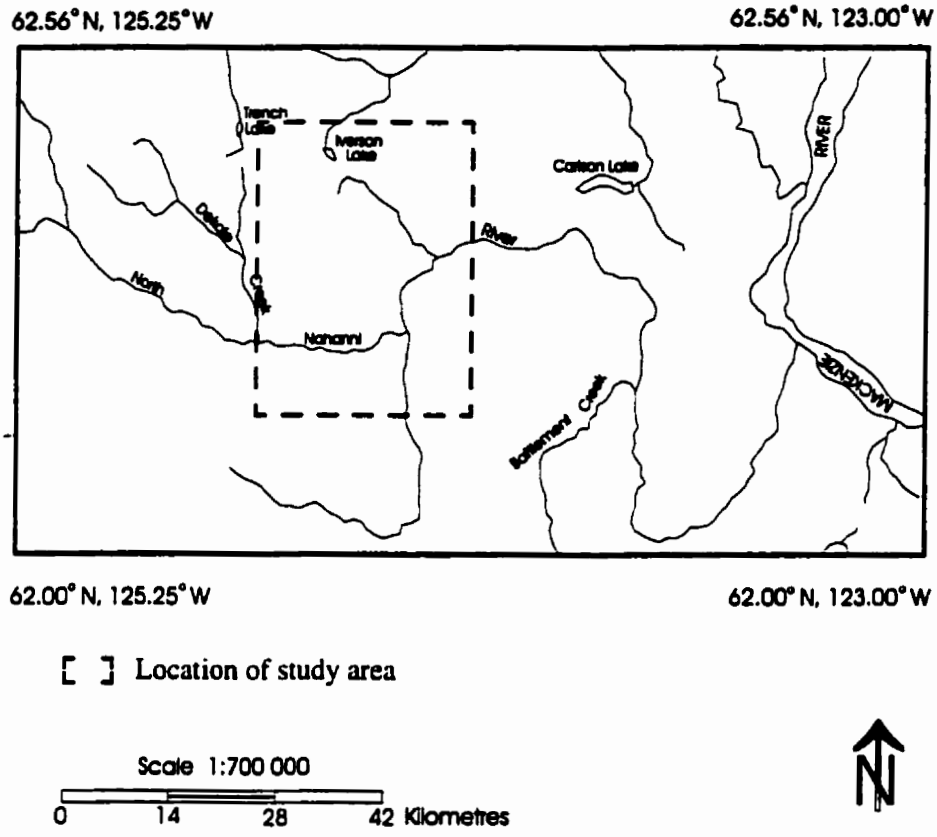

Figure 3.2 Detailed map of the North Nahanni River study area.

the area, and this century a small number of earthquakes with magnitudes greater than 6 have been recorded.

3.2 Physiography

A portion of a 1:250 000 topographic map of the Nahanni study area is shown in Figure 3.3. The eastern part of the study area is dominated by the Great Slave Plain which lies between the mountain ranges west of longitude 124°W and the uplands of the Precambrian Shield. Elevations vary from about 150 m to 300 m over most of the Plain. The entire Plain has been glaciated from east to west leaving behind numerous lakes. Glacial till thickness varies considerably across the area and Pleistocene and Holocene deposits cover the bedrock in most areas (de Wit et. al., 1973).

The western part of the study area is more mountainous consisting of northerly to northwesterly trending ranges and broad valleys. The Franklin Mountains, which comprise the easterly chain, rise suddenly from the adjacent plains and uplands. At the mountain front, upper Precambrian to upper Paleozoic rocks form high cliffs with ridges that reach an elevation of about 1500 m. In the northern part of the area these front ranges are separated from the Mackenzie Mountains by the Mackenzie Plain, which includes the valley of the Mackenzie north of Camsell Bend, where the river turns sharply northward. The mountainous area south of the South Nahanni River is referred to as the Liard Plateau. Elevations here are around 1500 m, slightly lower than the Mackenzie Mountains to the north (de Wit et. al., 1973).

Figure 3.3 Topographic map of the Nahanni study area.

3.3 Regional Geological Setting

No detailed geological maps or survey reports are available for the region, geological information is limited to a few surveys done in the late 1960's and early 1970's. The North Nahanni River study area covers parts of several major tectonic and stratigraphic provinces. The Precambrian Shield is exposed on the eastern edge; the central part, lying within the Interior Platform, is underlain mainly by Devonian and Cretaceous formations; and the western portion is in the Cordilleran belt where the accumulation of Phanerozoic sediments has been the greatest (de Wit et. al., 1973). The total thickness of Phanerozoic sediments increases in a westward direction from the edge of the Canadian Shield. Facies boundaries are not distinct but there is a general trend for Paleozoic carbonate sequences to change to shale towards the west (de Wit et. al., 1973).

Paleozoic sediments generally overlie the granitic Precambrian basement but quartzites and argillites of Proterozoic age have been penetrated by many wells. The Proterozoic beds are overlain with angular unconformity by Cambrian strata. In the Mackenzie Mountains the Cambrian increases in thickness and is essentially a carbonate succession which changes into a sequence of shales farther westward. A thick development of Ordovician carbonates, especially dolomites, is present in the Mackenzie mountains. It varies from more than 600 m in the front ranges to 3500 m in the mountains before passing laterally into a thick shale sequence (de Wit et. al, 1973).

In the mountains, middle Devonian beds of Eifelian age rest unconformably on the lower Devonian. They directly overlie the Silurian in the Franklin Mountains. To the east, on the Plains, middle Devonian beds rest on Precambrian, except where Cambrian and Ordivician strata have been preserved (de Wit et. al., 1973).

3.4 Stratigraphic Setting

A stratigraphic section for the upper crust in the Mackenzie Plain is shown in Figure 3.4. The Mackenzie Plain consists of a Precambrian crystalline basement overlain by a thick sequence of high velocity Proterozoic sedimentary rocks. Depth to the basement is almost 9 km (Canadian Oil and Gas Lands Administration, unpublished data, 1969). The thickness of the Proterozoic layer, extrapolated from Proterozoic units outside the area, suggests a thickness of almost 5 km. The Proterozoic sequence consists of shale interbedded with sandstone and dolomite. The Paleozoic rocks consist primarily of dolomites and limestones of Cambrian to mid-Devonian age. Two oil wells drilled down to the base of the mid-Devonian formations show a thickness of at least 2.3 km for these units (Canadian Oil and Gas Lands Administration, unpublished data, 1969), with an additional kilometre for the earlier Paleozoic unit. Some areas are covered by a weathered sequence of upper-Devonian shales and mudstones named the Fort Simpson Formation. These vary from 0 to 1.5 km. Thus the total thickness of the Paleozoic rocks in the Mackenzie Plain is approximately 5 km and the total thickness of sedimentary rocks is approximately 10 km or less (Wetmiller et. al., 1988)

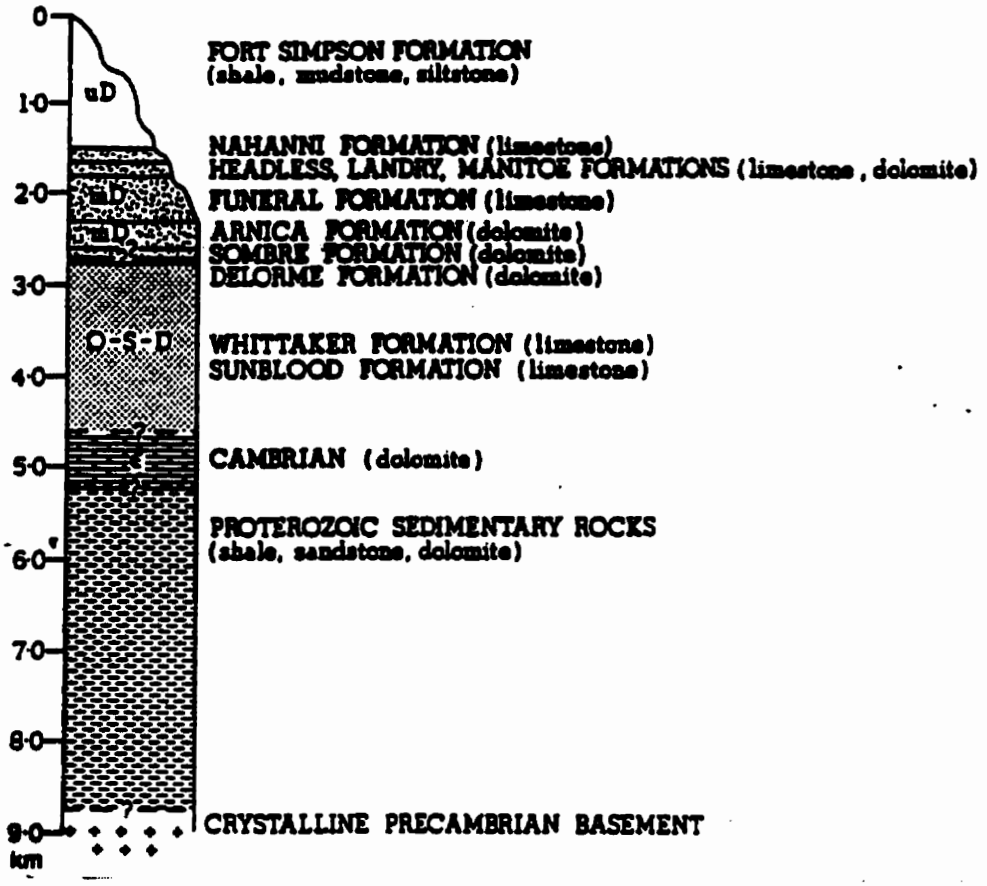

Figure 3.4 Simplified stratigraphic section of the North Nahanni River field area. Ages of rock units are given by D for Devonian, O for Ordivician, and S for Silurian; u and m are upper and middle respectively (after Wetmiller et. al., 1988).

3.5 Structural Geological Setting

Stress indicators in the region suggest crustal rocks in the region are subjected to horizontal compressive stress in the northeast-southwest direction similar to most of northeastern North America. North trending thrust faults and folds of late Cretaceous - early Tertiary Laramide age, associated with the Columbian Orogeny, are prevalent throughout the Foreland Belt of the northeastern Cordillera and represents one of the last major tectonic events in the region (Wetmiller et. al., 1988).

The study area is located in the Mackenzie Fold Belt, part of the larger Foreland Fold Belt of the northeastern Cordillera. The Mackenzie Fold Belt can be divided into four major tectonic units (from east to west): the Interior Platform, the Franklin Mountains, the Mackenzie Plain, and the Mackenzie Mountains (Figure 3.5). These units have similar lithologies, but can be characterized by the varying degrees of deformation each has undergone. The main deformational episode is the late Cretaceous - early Tertiary Laramide Orogeny (Wetmiller et. al., 1988).

Li (1993) examined linear features using the Hough transform in Landsat, CCRS airborne, C-SAR, and SPOT imagery and noted areas of dense linear feature distribution which reflect the complex pattern of the fold belt. Figure 3.6 shows interpreted linear features acquired from Landsat MSS image data. Li (1993) notes that the features are mostly NW-SE trending and may represent structural characteristics of the Precambrian basement.

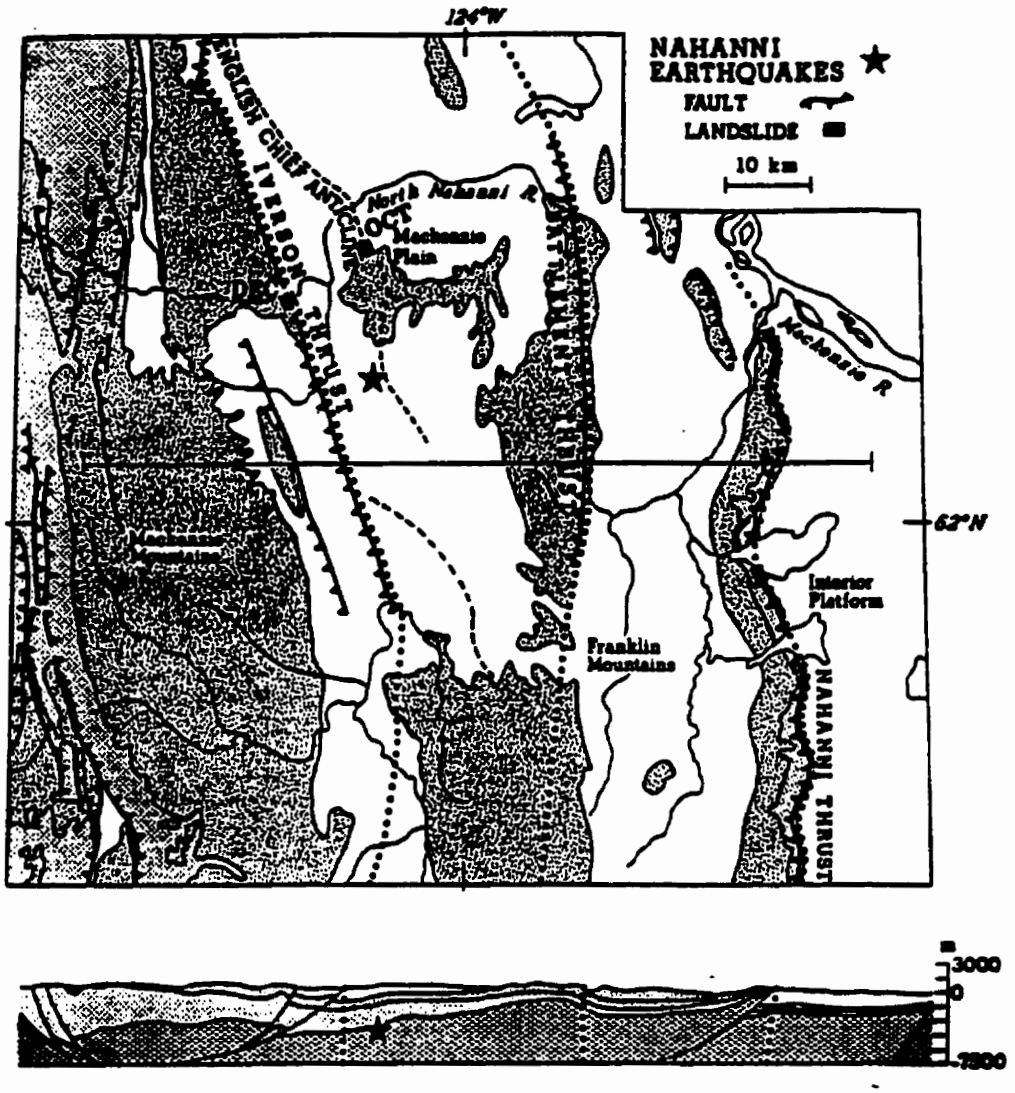

Figure 3.5 Simplified geology of the North Nahanni River study area. The patterns representing stratigraphic units are defined in Figure 3.4. The main physiographic subdivisions and principal faults are shown as well as epicentres for the main shocks (after Wetmiller et. al., 1988).

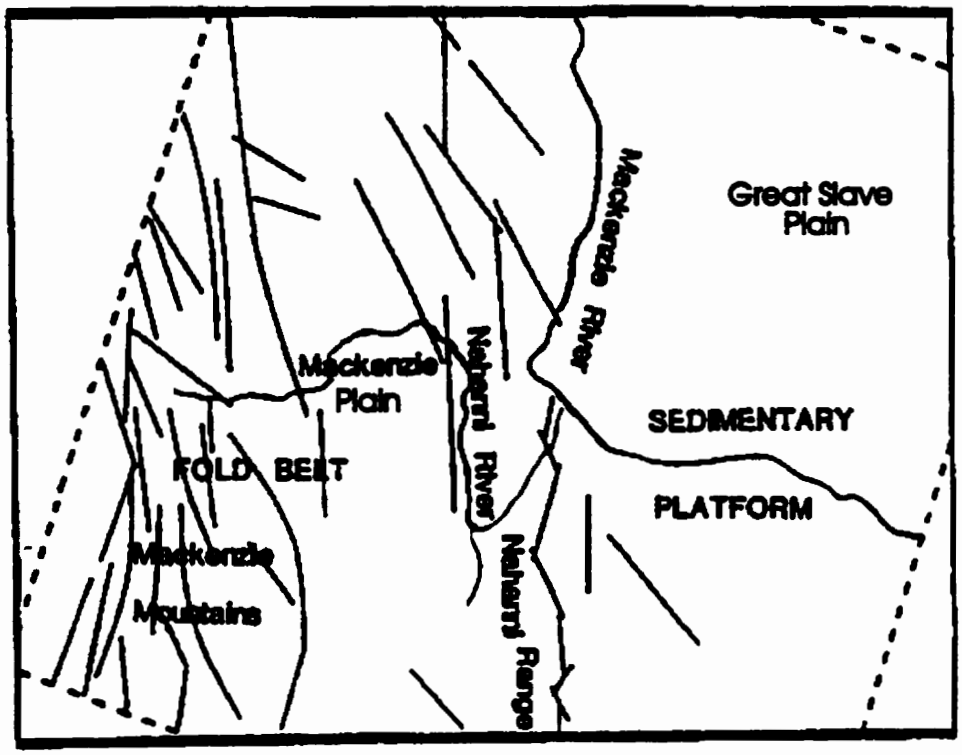

Figure 3.6 Interpreted linear features from Landsat MSS satellite imagery using the Hough transform (Li, 1993).

3.6 Earthquake Activities

Three of the largest earthquakes to have occurred in western Canada took place in the area near the North Nahanni River about 160 km west of Fort Simpson. On October 5, 1985 a M_s 6.6 earthquakes struck the region followed by a M_s 6.9 on December 23, 1985. On March 25, 1988 a M_s 6.2 earthquake took place. The felt area included the Northwest Territories, Yukon Territories, B.C., Alberta, and Saskatchewan (Figure 3.7). These earthquakes were followed by extensive aftershock sequences. The most noteworthy of the effects of these earthquakes was the fourth largest landslide in Canada in this century caused by the October event, and the December event triggered the strongest near-field seismic accelerations (>2g) ever recorded for an earthquake (Wetmiller et. al., 1989). Choy & Boatwright (1988) suggest that the strong near-field seismic accelerations could have been a localized phenomenon as the peak acceleration arrived late in the waveform with a very distinct frequency content. These earthquakes presented a unique opportunity to study intraplate earthquakes, particularly in thrust environments such as the northeast Canadian Cordillera.

3.6.1 Previous Earthquake Activity

Figure 3.8 shows the documented earthquake activity in the northeastern Cordillera. Prior to the Nahanni earthquakes no earthquakes with magnitude greater than 6 had been recorded in the northeast Cordillera although earthquakes with lower magnitudes have occurred frequently. A distinct linear band of epicentres extends south from the Beaufort Sea

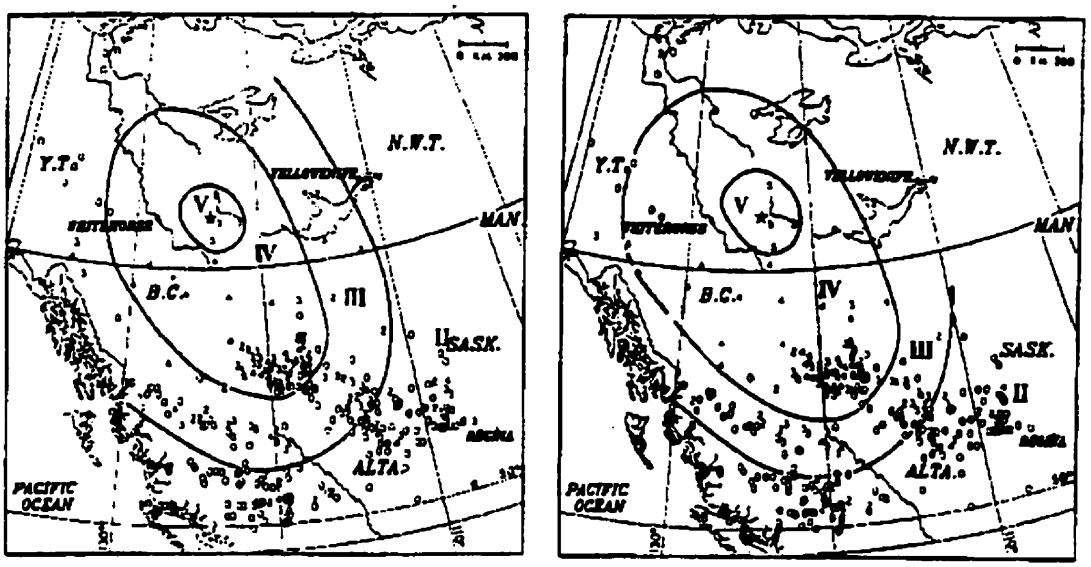

Figure 3.7 Felt reports and isoseismal distribution for the (*left*) October 5, 1985 and (*right*) December 23, 1985 Nahanni earthquakes. Population density in the epicentral region is near zero (after Wetmiller et. al., 1989).

Figure 3.8 Epicentres of Nahanni earthquakes (1985) and the seismicity of the northeastern Cordillera.

along the eastern boundary of the Cordillera to about 65°N. At this latitude the epicentral pattern becomes more diffuse, but activity continues to the southeast into the region where the Nahanni earthquakes occurred. Here, the activity shows two possible linear trends but are confined to the Cordilleran region. The area of the Canadian Shield immediately to the east is relatively aseismic. Three earthquakes of magnitude 6 are known to have occurred in the northeastern Canadian Cordillera; two events in 1940 and one in 1955, and one other magnitude 6 event in 1918 is known in the southeastern Canadian Cordillera (Rogers & Ellis, 1979).

3.6.2 The Faulting Mechanism

Contemporary stress indicators suggest that the crustal rocks in the region are subjected to horizontal compressive stresses in the northeast-southwest direction, similar to that found in most of northeastern North America (Adams, 1985). This kind of stress regime favours thrust and/or strike-slip earthquake activity. Leblanc & Wetmiller (1974) determined a right-lateral, strike-slip mechanism for a magnitude 4.8 earthquake in the northern part of the area near Fort McPherson, and suggested a correlation between the earthquake activity and the dominant set of north-trending faults in their study area. North-trending thrust faults and folds of late Cretaceous - early Tertiary Laramide age, associated with the Columbian Orogeny, are prevalent throughout the Foreland Belt of the northeastern Cordillera (Wheeler & Gabrielse, 1972) and represent one of the last major tectonic events in the region. Herron et. al. (1974) suggested that this tectonic activity was part of a Cenozoic plate boundary thrust zone created in the later stages of the development of the northeastern Cordillera.

The Nahanni region was heavily glaciated in the past which may also play a role in tectonic activity in the area. Wu & Hasegawa (1996) analyzed the effect of stresses caused by glacial loading/unloading and numerically computed the mode of failure. Their results indicate that under all combinations of tectonic stress, crustal loading promotes fault stability directly under the load - which may explain why the interior of central Canada and Greenland, which were covered by ice in the past, are virtually non-seismic at present (Figure 3.9). Upon removal of the load, thrust faulting is predicted within the ice margin. Even though the study area is focused some distance from the centre of the Hudson Bay ice sheet, it is in the western edge of the ice margin (Figure 3.10).

3.6.3 Recent Earthquakes

The analysis of Wetmiller et. al. (1988) of the two Nahanni earthquakes that occurred in 1985 show that the two main shock hypocentres are located within a few kilometres of each other at 62.19^{o}N, 124.24^{o}W and at a focal depth of 6 km. Table 3.1 shows some of the key parameters calculated for the October and December main shocks. The main shocks are north-striking (N175^{o}E), west-dipping (34^o for the October event and 25^o for the December event), closely spaced or possible co-planer listric fault planes. Failure along a pre-existing, but buried, Laramide-aged fault is suspected but no surface fault break was found (Horner et. al., 1990). The close proximity of the two epicentres indicates that the earthquakes ruptured the same fault. Teleseismic analysis of the two Nahanni earthquakes suggests that their rupture processes were dominated by the failure of asperities - localized areas of strong

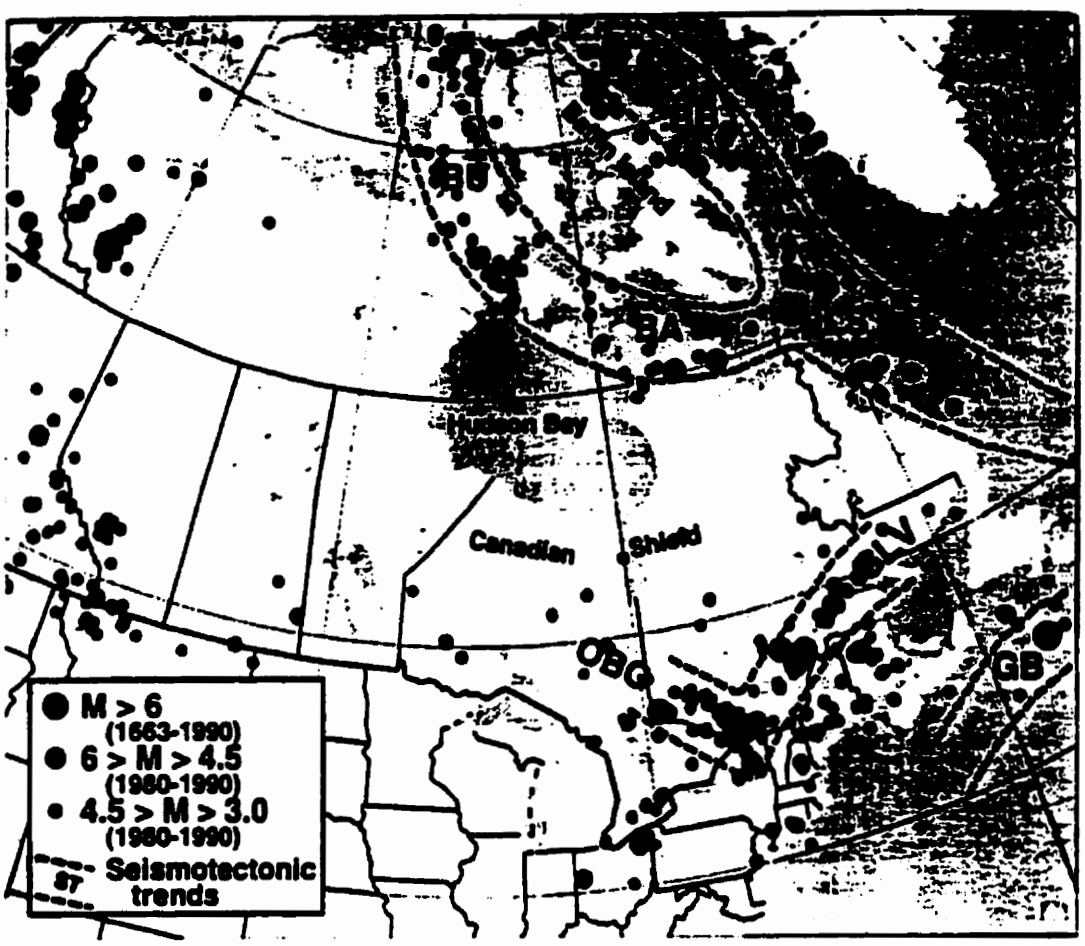

Figure 3.9 Map of eastern Canada showing seismotectonic trends and earthquakes greater than *M* 3.0 over specified time periods. Note that there are virtually no earthquakes in central Canada and Greenland. (after Adams & Basham, 1989).

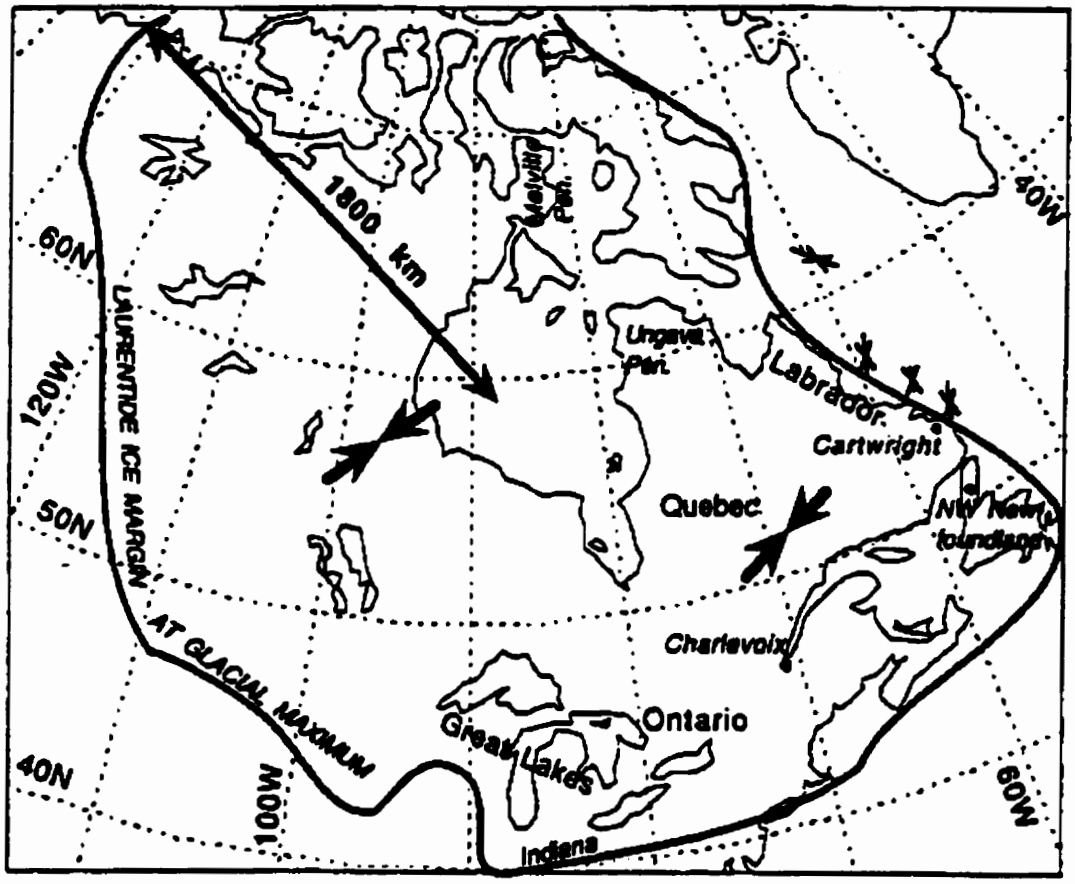

Figure 3.10 Map of eastern Canada showing (1) the margin of the Laurentian ice-sheet during the glacial maximum (18 000 BP), and (2) the orientation of the contemporary stress field in eastern Canada. The study area is located on the western edge of the ice margin (Wu & Hasegawa, 1996).

stress release which are surrounded by areas with little or no stress drop which slip after asperities fail (Choy & Boatwright, 1988).

	October 5, 1985	**December 23, 1985**
Origin time	15:24:05 UTC	05:16:06 UTC
Epicentre	61.19°N, 124.24°W	62.19°N, 124.24°W
Focal Depth	6 km	6 km
Magnitude	6.6 M_w (6.6 M_s, 6.5 m_b)	6.8 M_w (6.9 M_s, 6.4 m_b)
Felt Area	1.5 million km^2	>1.5 million km^2
I_o	MM IX	MM IX
Strike	N175°E	N175°E
Dip	34°W	25°W
Length	25 km	25 km
Width	15 km	15 km
Slide Volume	5-7 million m^3	0.1 million m^3

Table 3.1: Parameters (epicentral coordinates, focal depth, magnitude, etc.) calculated for the October and December main shocks (modified from Wetmiller et. al., 1988).

A total of 323 aftershocks occurred between October 5, 1985 and March 25, 1988 (Figure 3.11). The overall distribution extended over a rectangular area measuring approximately 60 km by 20 km elongated in a north-south direction. The two main shocks occurred in the east-central part of the aftershock zone. The aftershocks are not associated with any of the large Laramide-aged thrust faults mapped at the surface, or with their inferred extension to

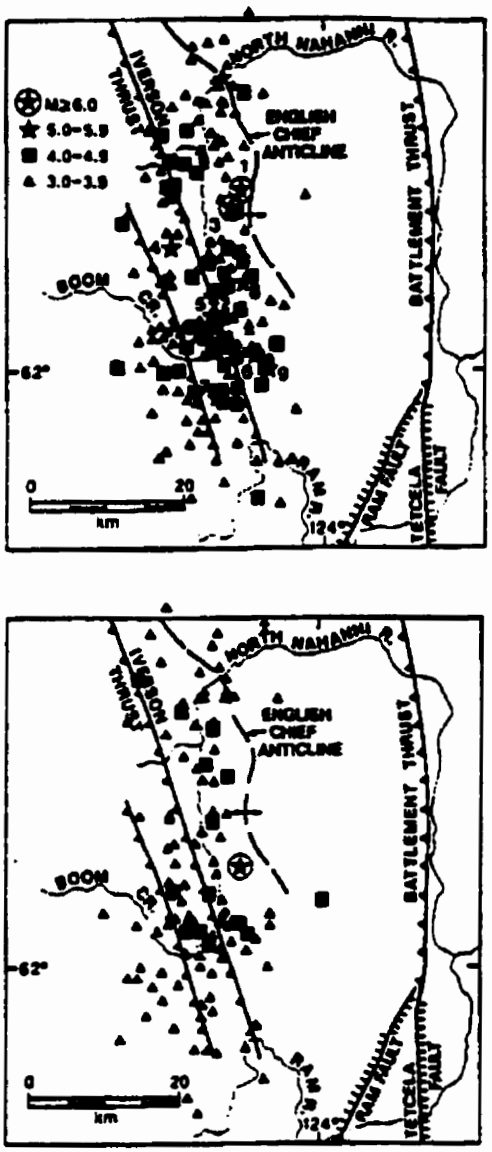

Figure 3.11 Epicentres of 323 Nahanni earthquakes (*M* 3.0 and greater) (*top*) from October 5, 1985 to March 11, 1986 (199 events), and (*bottom*) from March 12, 1986 to March 25, 1988 (124 events). The *M* 5.0 and larger earthquakes are numbered in chronological order up to the *M* 6.2 earthquake that occurred on March 25, 1988. Numbers 1 and 3 are the October 5, 1985 and December 23, 1985 main shocks respectively (Horner et. al., 1990).

depth, but detailed geological information for the epicentral region is lacking (Horner et. al., 1990).

Moon et. al. (1991), using C-SAR/SPOT imagery, have suggested that a fault with a strike of approximately 355^{o} is located along the segment of the North Nahanni River which meets with Boom Creek and intersects the south end of the Iverson Thrust Fault. Moon et. al. (1991) have also suggested that the E-W trending segment of the North Nahanni River between the Iverson Range and the Battlement Thrust Fault to the east may represent another fault. This is supported by the work of Li (1993) in which it was noted that the earthquake epicentres are located along the N-S section of the North Nahanni River and disappear when the river turns east. Li (1993) suggests that a N-S trending tectonic feature may have been truncated by a major E-W trending geological structure between the Iverson Range and the Battlement Thrust Fault.

3.6.4 The Quiescent Zones

There was a seismically quiet zone around each of the main shock epicentres. The rectangles in Figure 3.12 represent idealized aseismic areas of 225 km^2 for the October event and 195 km^2 for the December event, based on seismicity observed in the first 24 hrs (Figure 3.12). The east and north boundaries in particular were poorly defined. Choy and Boatright (1988) determined that the October main shock consisted of two subevents 3.6 s apart. The second subevent was located 5.7 km south of the first. The December main shock consisted of

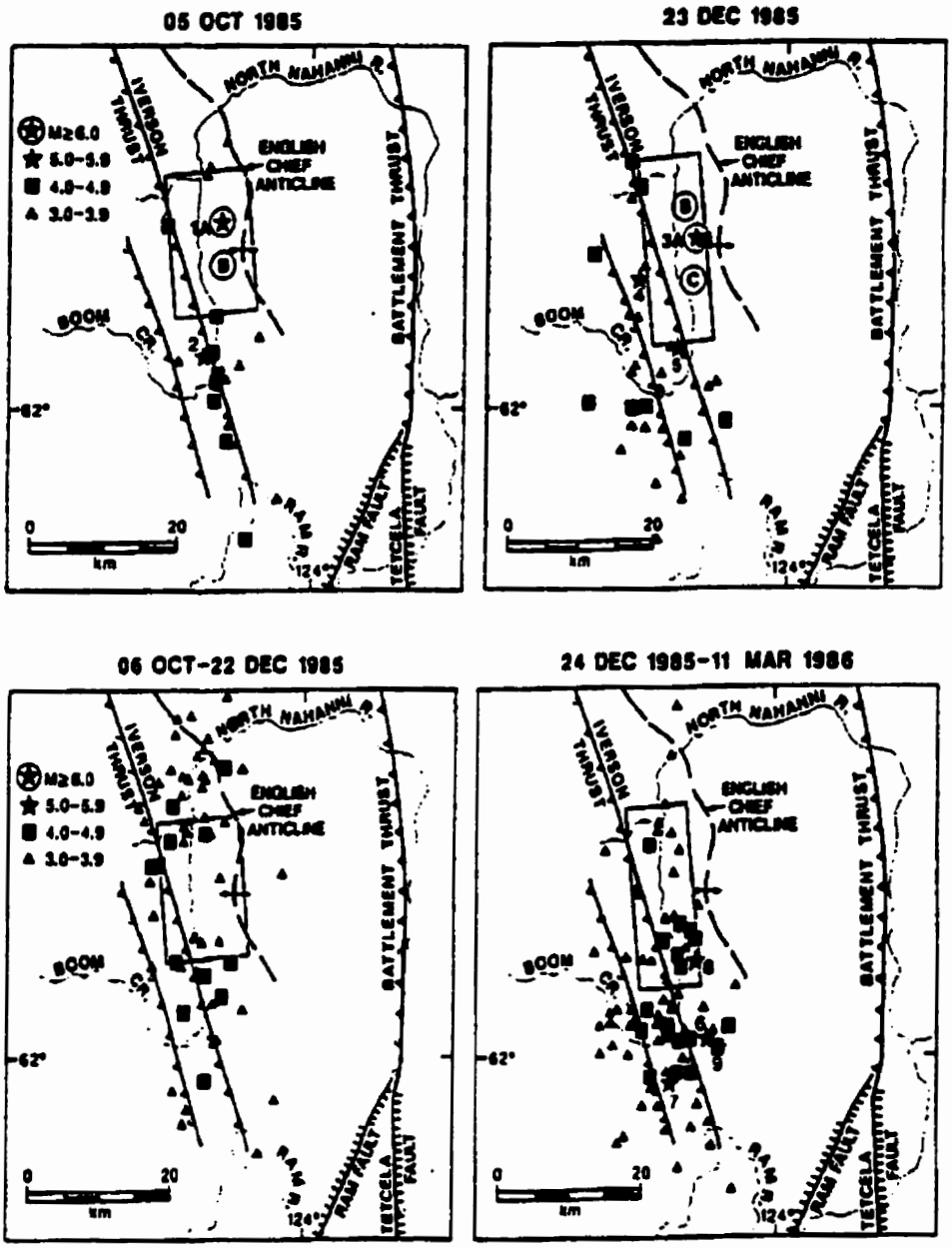

Figure 3.12 (*top*) Comparison of aftershock activity in the first 24 hrs following each main shock. Event numbers are the same as from Figure 3.7. The rectangles approximate the extent of a quiescent zone around each of the main shock epicentres. (*bottom*) Comparison of aftershock activity over a 78 day period from 1 day after each main shock. Event numbers are the same as Figure 3.7 and rectangles are the same as in (*top*) (Horner et. al., 1990)

three subevents. The second subevent occurred 0.8 s after and first and 3.6 km to the NNW of the initial event. The third subevent occurred 3.5 s after the first and 4.9 km to the south of the initial event. The distribution of the subevents corresponded very well with the seismically quiet regions.

Aftershock activity from October 6 to December 22, 1985 and from December 24, 1985 to March 11, 1986 (an equal period of 74 days) is shown in Figure 3.12. The October aftershocks extended about 10 km further north and activity became more evenly distributed north and south of the main shock. The quiescent zone around the main shock continued to be stable however, indicating that it represents an important feature of the earthquake process. The aftershock pattern exhibited by the December sequence was much more asymmetric; intense-aftershocks occurred predominantly to the south of the main shock. The quiescent zone around the main shock filled in during this period, particularly to the south. However this appears to be due to secondary faulting off the main rupture plane and the quiescent zone persisted on the main rupture plane (Horner et. al., 1990).

CHAPTER 4

Synthetic Aperture Radar and Interferometric SAR Theory

4.1 SAR (Synthetic Aperture Radar)

4.1.1 Introduction

Radar (RAdio Detection And Ranging) satellites operate in the microwave portion of the EM spectrum. Therefore they have wavelengths which are many orders of magnitude longer than optical satellites. The longer wavelengths allows the microwave energy to penetrate clouds, snow, haze, smoke, light rain, etc. which are impenetrable to signals operating in the optical portion of the EM spectrum. In addition radar satellites operate

as an active system which means that they generate their own signal, therefore they can obtain images day or night.

Real Aperture Radar

Real aperture radar (RAR) uses a fixed antenna on a platform (aircraft or satellite) which emits pulses of EM energy perpendicular to the azimuth direction (the direction in which the platform is moving). The EM energy is scattered in many directions upon contact with the ground including the direction back to the antenna. Analysis of the amount of energy returned to the satellite and the length of time it takes to return gives the brightness of a particular target and its distance. A smooth object reflects most of the energy away from the antenna and therefore appears dark; a rough object scatters the EM energy, including some back to the antenna and therefore appears bright.

The ability to distinguish between two objects on the ground in the azimuth direction is related to the length of the antenna and the slant range (the line-of-sight distance measured from the antenna to the terrain target). Figure 4.1 shows how the beam from the antenna spreads as it approaches the ground due to the interference of the waves emitted from and received by the dipoles of the antenna. Two objects on the ground, and with the same slant range R, can only be imaged separately if they are not both in the beam at the same time. Therefore the azimuth resolution, the resolution in the direction that the satellite is travelling, can be given by

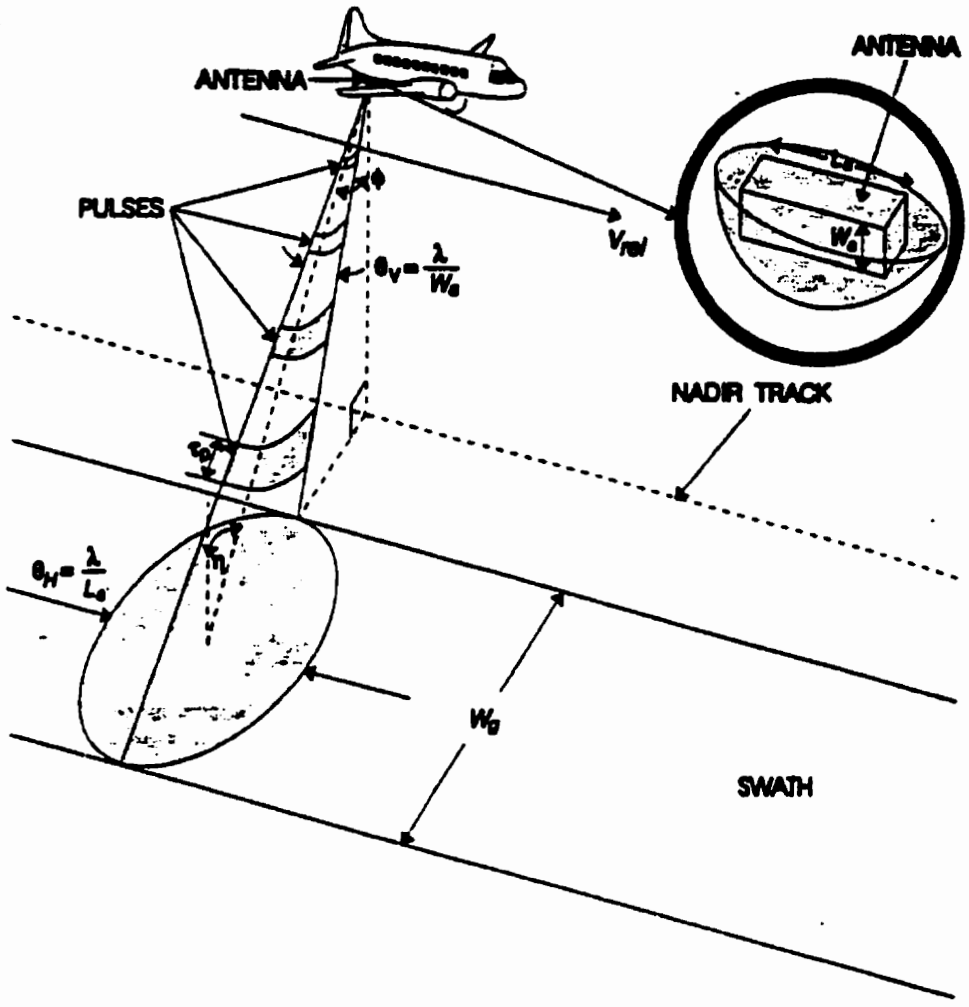

Figure 4.1 Geometry of a side-looking real aperture radar system (EarthView, 1996a).

$$\rho_a = R\theta_H = \frac{R\lambda}{L_a}, \tag{4.1}$$

where λ is the wavelength of the beam, L_a is the length of the antenna, and θ_H is the angular spread of the beam (beam width). Therefore if the antenna length is increased the beam spread becomes tighter and the azimuth resolution is improved. If, for example, RADARSAT operated as a real aperture radar satellite its azimuth resolution would be

$$\rho_a = \frac{(798 \times 10^3 m)(0.0566m)}{15m} = 3.0km. \tag{4.2}$$

The range resolution, the resolution perpendicular to the direction that the satellite is travelling, is independent of the length of the antenna. The range resolution is only dependent on the imaging angle (the angle which the radar beam makes with the ground) and the duration of the radar pulse.

Radar remote sensing is carried out using an antenna which looks perpendicular to the direction that the platform is travelling. These systems are termed Side-Looking Radar (SLR) or Side-Looking Airborne Radar (SLAR). The basic operating principle of a SLAR system is shown in Figure 4.2. Microwave energy is transmitted from an antenna in short pulses (~10^{-6} s/pulse). In Figure 4.2 (*top*) the propagation of one pulse is shown by indicating the wavefront locations at successive increments of time. The solid lines (labeled 1 through 10) show the transmitted pulse moving from the aircraft in a focused beam. After time 6 the pulse reaches the house and a reflected wave (dashed line) is shown beginning at time 7. At

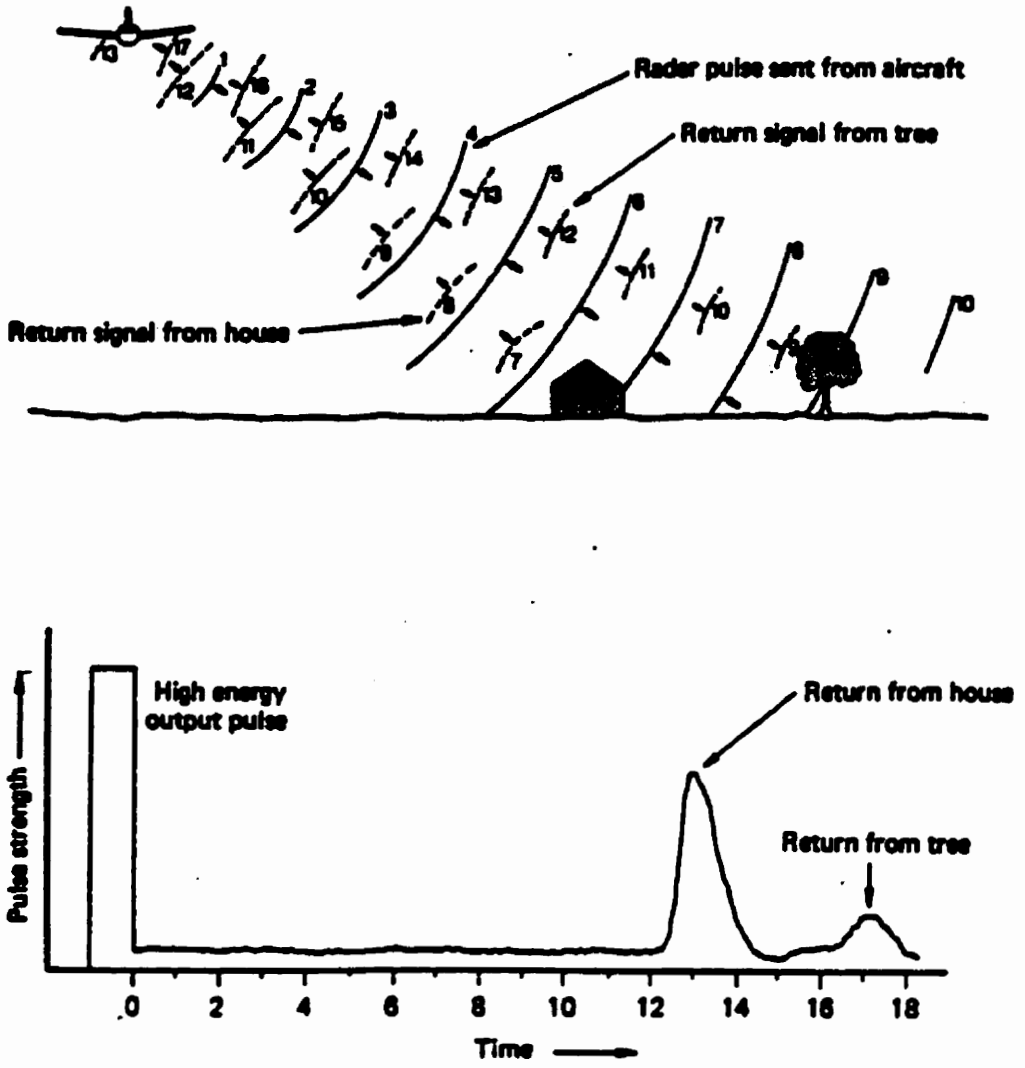

Figure 4.2 Operating principle of SLAR. (*top*) Propagation of one radar pulse (indicating the wavefront location at time intervals 1-17). (*bottom*) Resulting antenna return (Lillesand & Kiefer, 1994).

time 12, this return signal reaches the antenna and is recorded on the antenna response graph (Figure 4.2 (*bottom*)). At time 9, the transmitted wavefront is reflected off the tree and the reflected wave reaches the antenna at time 17. Because the tree is less reflective of radar waves than the house, a weaker response is recorded in Figure 4.2 (*bottom*).

By measuring the return time of the waves, the range, or distance, between the transmitter and reflecting objects can be determined. The slant range to any given object is given by

$$R = \frac{ct}{2} \tag{4.3}$$

where

R = slant range (direct distance between transmitter and object),

c = speed of light

t = time between pulse transmission and echo reception

(Lillesand & Kiefer, 1994).

Synthetic Aperture Radar

SAR overcomes the problems of resolution associated with RAR. As was mentioned earlier, the longer the antenna on a platform is the better the resolution will be. However it is not practical to build an antenna long enough to achieve a resolution of less than 20

m. SAR systems use a relatively short antenna, but through modified data recording and processing techniques (which are discussed in Section 4.1.3) they synthesize the effect of a very long antenna. By using SAR it is possible to achieve resolutions in the range of 10-20 m. A number of earth surface features work together with the wavelength, incidence angle, and polarization of radar signals to determine the intensity of radar returns from various objects. These factors include geometric characteristics (e.g. terrain), electrical characteristics of the surface, soil response, vegetation response, and water and ice response (Lillesand & Kiefer, 1994).

4.1.2 - SAR Imaging Geometry

SAR systems operate as a SLR system where, as the name implies, the ground is imaged at an angle perpendicular to the flight path. Figure 4.3 shows the geometry of a SAR system and the terminology used. The direction that the aircraft or satellite moves is called the azimuth or along-track direction. The range or look direction is the imaging direction which is perpendicular to the azimuth direction. The line projected horizontally on the ground from the flight path is called the nadir line or ground track. The slant range is the line of sight distance measured from the antenna to the target, and the ground range is the distance measured along the surface from the nadir line to the target. The area closest to the ground track where the beam illuminates the surface is the near range while the area farthest away is the far range.

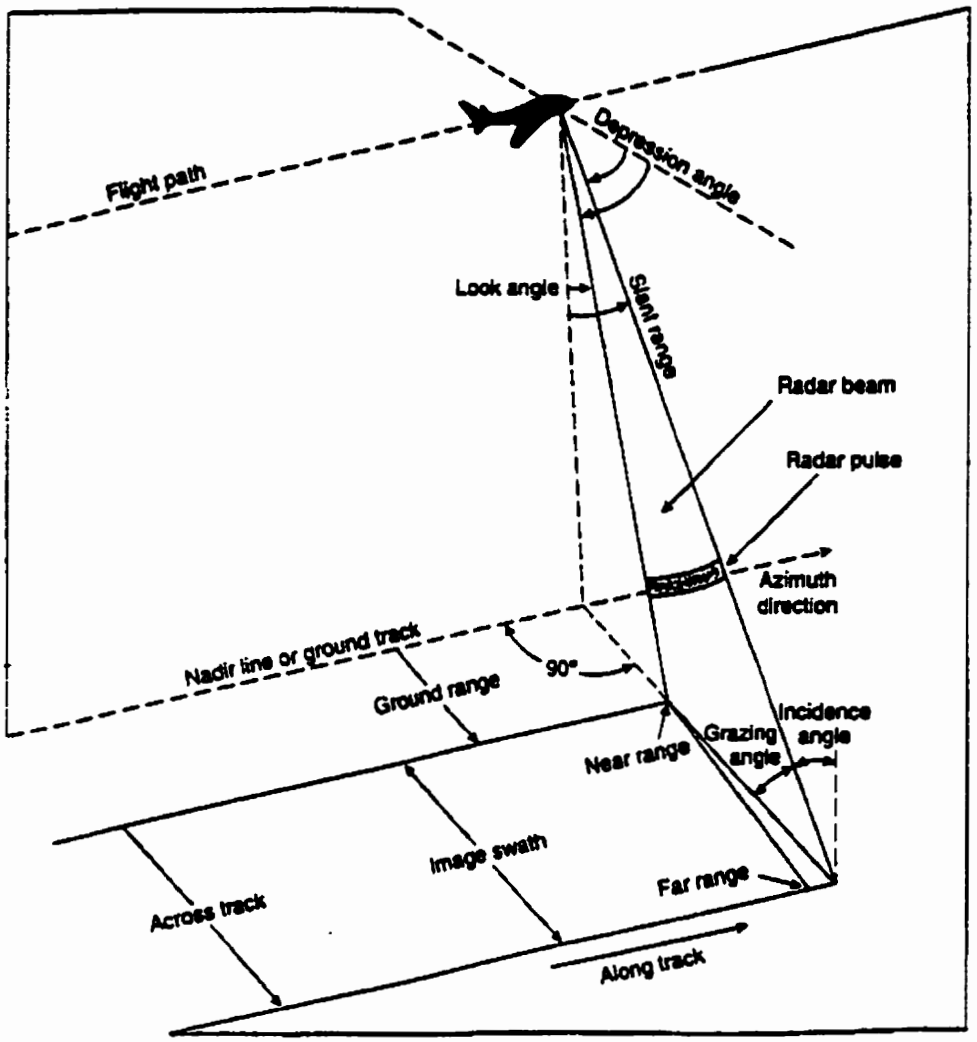

Figure 4.3 Operating principle of a SAR system (Avery & Berlin, 1992).

The depression angle is the angle measured from a horizontal plane downward to a specific part of the beam. The depression angle varies across the image swath from a large angle at near range to a small angle at far range. The angle measured from a vertical plane upward to a specific part of the beam is the look angle which varies in the opposite manner to the depression angle. The incidence angle is measured between the beam axis and a line perpendicular to the ground surface where the beam strikes, and its complement is the grazing angle.

4.1.3 SAR Theory

Introduction

As was mentioned in section 4.1.1 (Equation 4.1), the longer the antenna on a platform is the better the azimuth resolution will be. A SAR system takes advantage of the forward motion of the platform to synthesize a large antenna aperture. The real antenna is carried to successive positions along the flight line and each successive portion is treated electronically as though each were an individual element of the same antenna (Avery & Berlin, 1992). Equation 4.1 gives the beam width, θ_H, of a RAR system. Similarly the beam width of a SAR system with a synthetic antenna of length L_s is

$$\theta_s = \frac{\lambda}{2L_s}. \tag{4.4}$$

The factor of 2 is present in the denominator because of the two-way propagation path from the antenna to the target and back as compared with the one-way path of a conventional antenna (Skolnik, 1980).

There are two fundamental limits to the maximum effective length of a synthetic aperture. One is that the length of the effective aperture L_s can be no greater than the width of the region illuminated at the range R by the real antenna, given by Equation 4.1. Thus $L_s \leq R\theta_H$. The second limit is that the difference between the maximum and minimum (two-way) along-track paths is a quarter wavelength (Figure 4.4). When this condition applies the system is referred to as a *unfocused* SAR system. From this geometry, the effective length L_s of the synthesized antenna is $\sqrt{R\lambda}$ so that the azimuth resolution for a unfocused SAR system is

$$\delta_a = \frac{\sqrt{R\lambda}}{2} \tag{4.5}$$

(Skolnik, 1980). This technique however does not account for the variable rate of phase change that occurs during signal acquisition.

If the received signal is corrected for the curvature of the spherical wavefront then the resolution can be improved even more. At each "element" of the synthetic aperture antenna a phase correction $\Delta\phi = (2\pi x^2)/(\lambda R)$ is applied where x is the distance from the centre of the synthetic aperture. This accounts for the nonlinear phase change and makes it

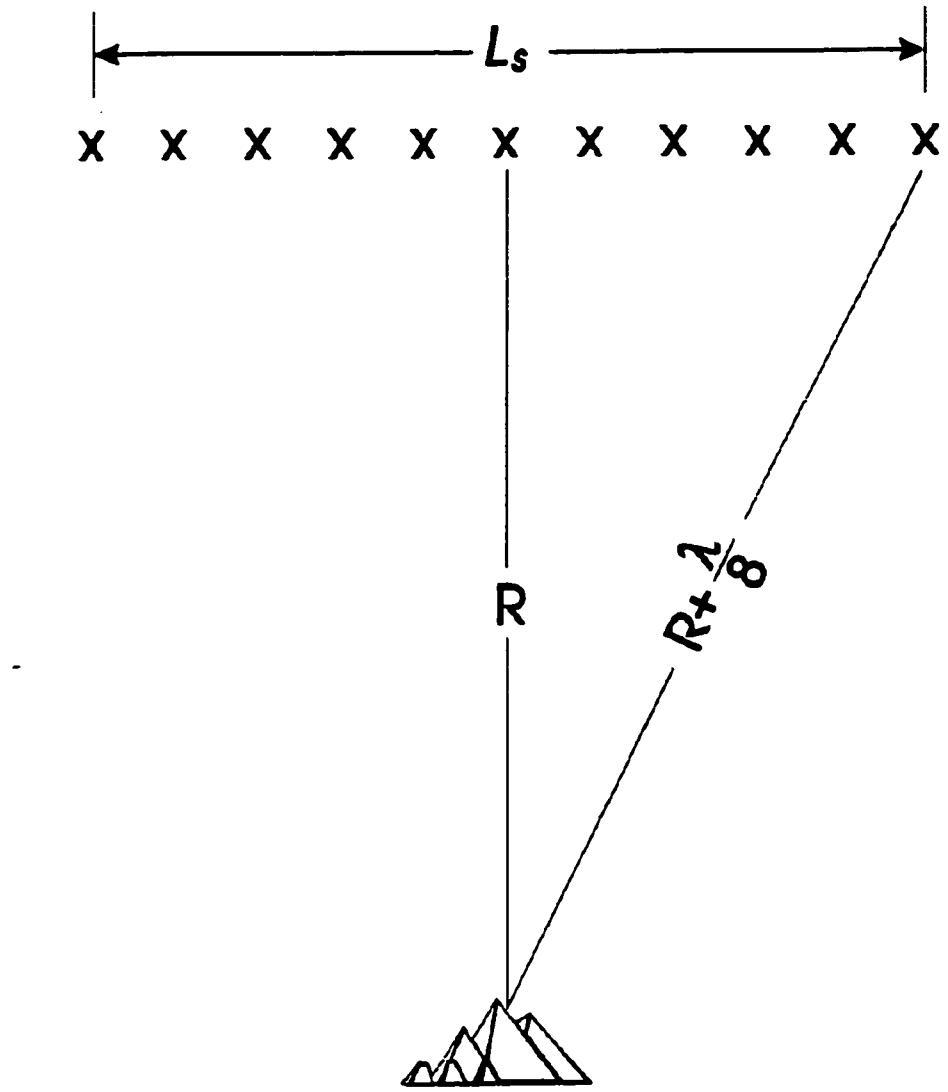

Figure 4.4 Geometry of an unfocused SAR. The radar transmits a pulse at each position marked by an x (modified from Skolnik, 1980).

possible to use all the data collected during the time that the target is within the beam (Earth-View, 1996a). When this correction is applied to each element of the synthetic antenna, the antenna is referred to as *focused* at a distance R and all the received echo signals from a target at that range are in phase. The azimuth resolution of a focused SAR system, using Equation 4.4 with $L_s = (R\lambda)/L_a$ is then given by

$$\delta_a = R\theta_s = \frac{L_a}{2} \tag{4.6}$$

The resolution of a focused SAR system is independent of the range and wavelength, and depends solely on the size of the real antenna (Skolnik, 1980).

An important point to be made is that the signals from the synthetic aperture antenna must be sampled at the proper rate. The sampling rate is referred to as the Pulse Repetition Frequency (PRF). The PRF is determined by the maximum range at which targets are expected. If the PRF is made too high, the likelihood of obtaining target echoes from the wrong pulse transmission is increased. This can result in erroneous range measurements (Skolnik, 1980). Therefore the sampling rate must not be too large; in practice this means that there will be some azimuth signal energy aliased (Harger, 1970). However the PRF must be high enough to avoid angle ambiguities and image-foldover. These two conflicting requirements on the PRF for SAR mean that the resolution and the coverage (swath) cannot be selected independently (Skolnik, 1980).

The Doppler Effect

At this point a discussion of the Doppler effect is in order. When a detector moves with respect to a source of waves a shift in frequency is observed which is known as the Doppler effect. When a source emitting waves with a frequency f recedes from an observer at a velocity v, the observed frequency is

$$f_o = \sqrt{\frac{1-(v/c)}{1+(v/c)}} f_s. \tag{4.7}$$

When the source approaches the observer the observed frequency is

$$f_o = \sqrt{\frac{1+(v/c)}{1-(v/c)}} f_s. \tag{4.8}$$

Therefore a receding source produces a lower frequency and an approaching source produces a higher frequency than the actual emitted frequency. When two targets on the ground are separated in the azimuth direction they are at slightly different angles to the antenna. Therefore they will have slightly different velocities relative to the antenna at a given moment and the signal reflected from each target will have its frequency shifted a different amount from the original due to the Doppler effect (EarthView, 1996a). This is one of the principles under which SAR operates.

SAR

Figure 4.5 shows how a large azimuth beamwidth is employed to illuminate a particular spot on the ground and provide reflections over the length of the synthetic aperture required. If the particular point in Figure 4.5 is isolated its motion can be followed as:

1. it enters the beam ahead of the platform causing a Doppler shift to higher frequencies;
2. when the platform is perpendicular to the point there is no Doppler shift;
3. as the platform moves away from the point the frequencies shift to lower frequencies.

The Doppler shift information is then obtained by electronically comparing the reflected signals from a given point with a reference signal that incorporates the same frequency as the transmitted pulse. This gives the phase history which contains a record of the Doppler frequency changes plus the amplitude of the returns from each ground feature as it passes through the beam of the moving antenna (Avery & Berlin, 1992).

The radiation with which a radar antenna illuminates its subject is referred to as "coherent" radiation, which means that the crests and troughs follow a regular sinusoidal pattern. Therefore, radar instruments can measure both the amplitude and the point in the oscillation - the phase - of the returned waves. Figure 4.6 shows two waves that have the identical wavelength and amplitude but are shifted in phase by $\pi/4$ allowing them to be distinguished from one another.

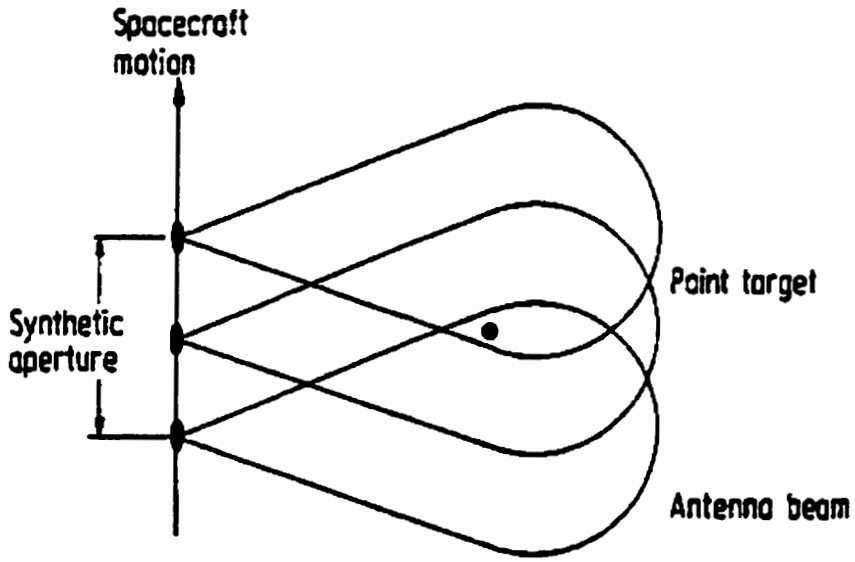

Figure 4.5 The concept of synthesizing a large antenna by utilizing spacecraft motion along its orbital path. Here a view from above is shown, illustrating how a small real antenna is used to ensure a large real beamwidth in azimuth. As a consequence a point on the ground is illuminated by the full synthetic aperture (Richards, 1986).

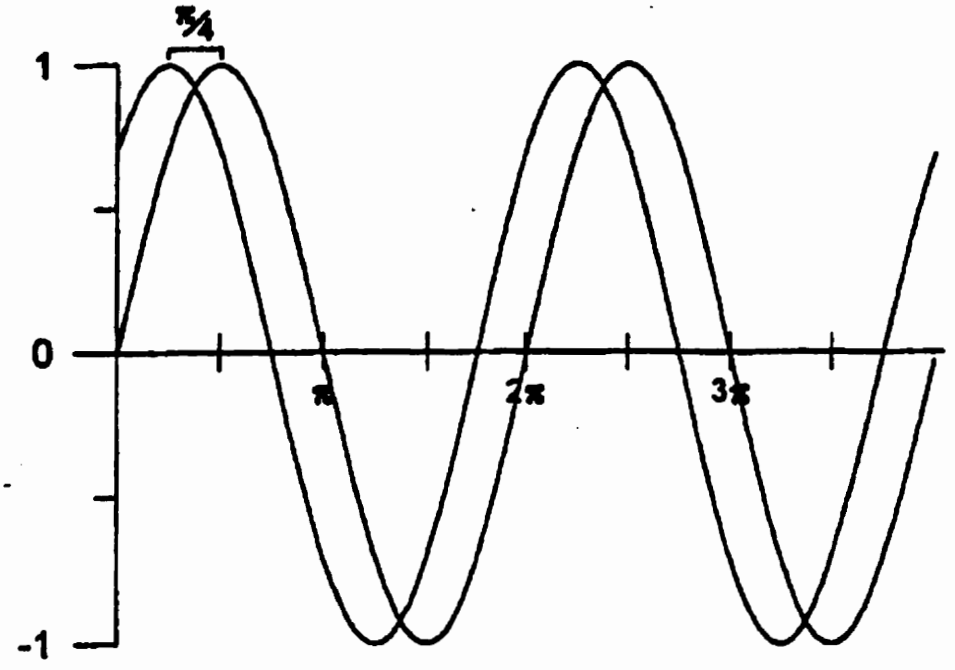

Figure 4.6 Showing two waves with the identical wavelength and amplitude but shifted in phase by $\pi/4$. This allows the two waves to be distinguished from one another.

SAR Azimuth Compression

As a radar beam passes over a point target, as in Figure 4.7, the slant range to the target varies as the platform and real antenna beam first approaches, then recedes, from each scatterer. Thus one target traces a hyperbolic line in the azimuth-slant range plane (EarthView, 1996a). This hyperbola is known as the range migration curve. Range walk is produced when scatterers enter and leave the radar beam at different slant ranges. This is particularly noticeable with spaceborne SAR platforms because of the earth's rotation beneath the satellite (Wehner, 1987). Since this hyperbola is representative of only one point, all the points along this curve must be compressed to form a single pixel in the final image. For airborne SAR, range is relatively small so that the curvature may produce much less than one range-cell (pixel) shift as the beam travels across scatterers. A digital image is composed of a two-dimensional array of discrete pixels that correspond spatially to relatively small terrain areas. For spaceborne SAR multiple range cell shifts may occur (Wehner, 1987).

Speckle

The amplitude of the returned wave depends on the number and type of scatterers on the ground, measurement of the amplitude gives the familiar black and white satellite images. Each pixel on the ground can contain numerous small targets, for example pebbles, rocks, and leaves, which can generate multiple reflections. Radar reflections from a pair of objects can interfere constructively or destructively as shown in Figure 4.8. Minor differences in geometry can therefore cause large changes in the amplitude of the pixels in a radar image. The indi-

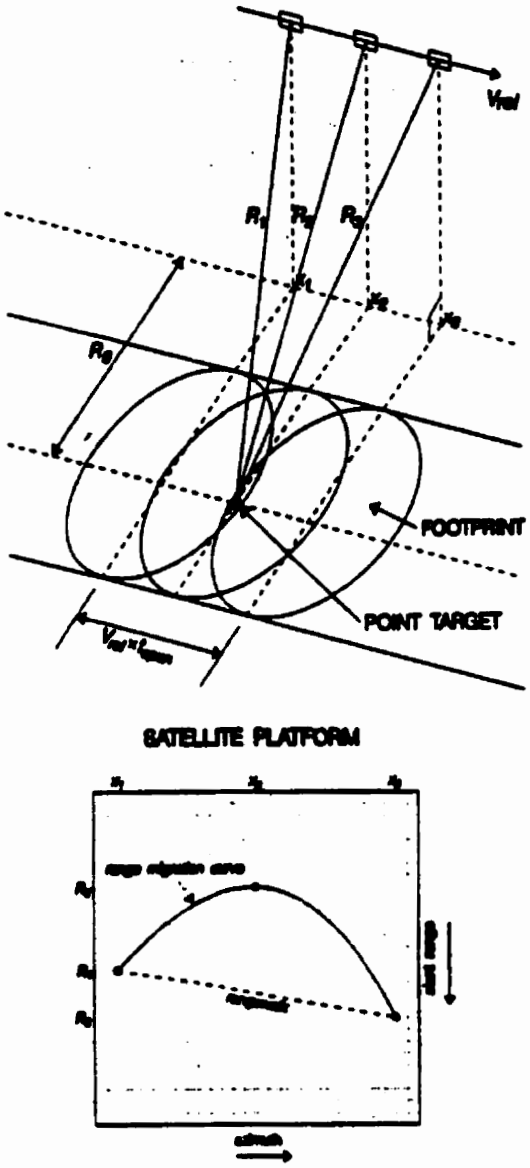

Figure 4.7 Hyperbolic curve traced by a point target in the azimuth-slant range plane (modified from EarthView, 1996a).

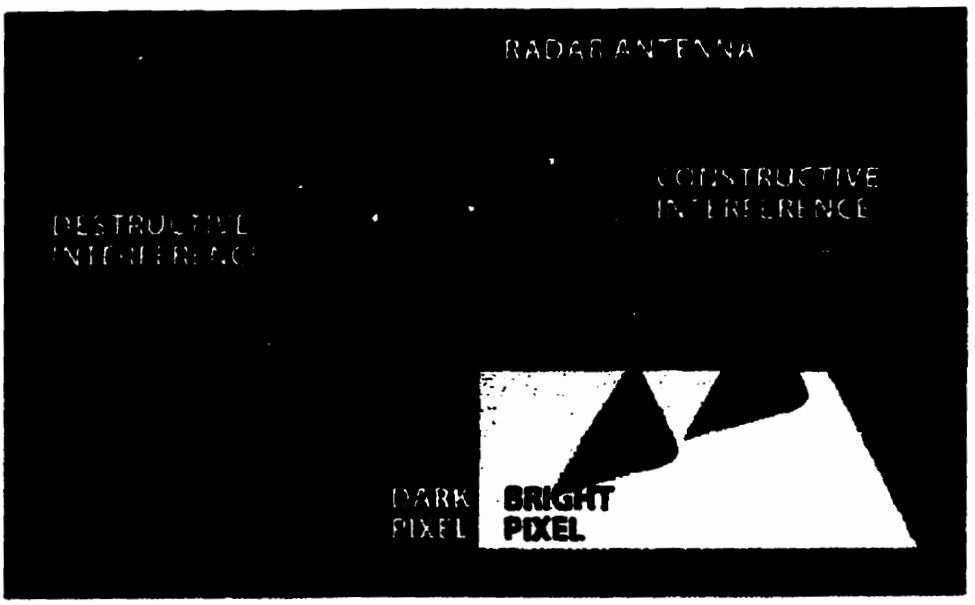

Figure 4.8 Radar reflections from a pair of objects can interfere constructively giving a bright pixel (*right*), or destructively giving a dark pixel (*left*). This will cause speckle in a satellite image (Massonnet, 1997).

vidual reflections can add together to make the overall reflection stronger (constructive interference), or cancel one another out (destructive interference). This phenomenon is called "speckle" and accounts for the grainy appearance of a SAR image.

These reflections combine in unpredictable ways and therefore the phase measurements for a given pixel seem random. However, comparing two radar images taken from roughly the same position but at different times reveals a great deal of information. While the phase itself appears random in either image, the phase difference between corresponding pixels in the two images is not. If two sequential satellite images are taken from exactly the same position, there should be no phase difference between any pair of corresponding pixels. But if the scene on the ground changes, even slightly, between two radar scans the phases of some pixels in the second image will shift.

4.1.4 SAR Applications

Since the early 1970's SAR has become over a valuable tool in remote sensing. This section will briefly mention a few of the areas in which SAR has been used extensively as mentioned in EarthView (1996a).

Polar ice has imbedded salt, brine pockets, and air bubbles; it is an inhomogeneous medium with a low dielectric constant. Thus volume scattering is high which makes SAR sensitive to the different physical properties of the ice. Ice classification is also possible using SAR. First year ice is generally much smoother than multi-year ice and therefore appears

much darker than multi-year ice in a SAR image. Ocean wave modeling using SAR can be carried out by extracting the wave spectra and identifying current patterns.

SAR sensors can also be used in forestry applications such as clear-cut boundary delineation and forest stand inventory updating. Since SAR can penetrate cloud cover, SAR sensors can be particularly valuable in tropical areas where there is almost constant cloud cover.

SAR imagery has been used extensively for structural and lineament geological mapping, lithology mapping, exploration for metals, and for oil and gas deposits. SAR has also been applied to the analysis of quaternary landforms, recent seismic disturbances, and meteorite impact craters. Algorithms for combining radar with geological and geophysical data sets and mineral deposit models are also being tested.

The volumetric content of water in the soil is directly related to the dielectric constant. At a given wavelength, the penetration depth decreases as the soil moisture increases, which results in an increase in the backscattered energy. Thus the returned signal is dependent on both the surface roughness and the moisture content. SAR imagery can also provide a means of discriminating soil moisture patterns in both time and space. Therefore it is possible to infer the distribution of soil moisture and infiltration capacity over large areas. SAR imagery was also used during the 1993 Mississippi River flood and the 1997 Red River flood to monitor and map flood extent and flood damage, and to provide rapid response for flood relief.

SAR can be used as a source of data for applications for determining crop area, size, type, and condition. Also techniques are being developed for using SAR imagery for determining soil moisture and the presence of saline soils. Studies have been performed to assess how the backscatter of various crop types varies with time of day, polarization, and moisture conditions.

The *Magellan* probe has mapped the surface of Venus using an S-band (132.7 m) SAR with a range resolution of 120 m at low altitudes and an azimuth resolution of 120 m at all altitudes. As well a mission is planned for mapping Saturn's moon Titan using SAR operating in the Ku-band (22 cm).

4.2 SAR Interferometry

4.2.1 Introduction

Repeat-pass SAR interferometry (InSAR) is a technique which produces an image from the phase difference between two SAR images acquired over the same region but at slightly different viewing angles. In order to reduce speckle in SAR images the common practice is to average the amplitudes of neighbouring pixels in radar images. However averaging the amplitudes destroys all the phase information of the radar reflections. Graham (1974) first demonstrated that it was possible to take advantage of the phase measured by airborne radar.

Zebker & Goldstein (1986), using a radar system mounted on a NASA CV990 aircraft, first demonstrated that InSAR was practical by generating a DEM of a portion of the San Francisco Bay area.

Airborne InSAR can be carried out in two ways: "along-track" or "cross-track". Along-track interferometry systems measure radar echo phase differences on repeat images separated in time by less than a second so the baselines are very short. The baseline is the distance between the sensor when the two images are acquired. This method is used almost exclusively for ocean surface motion studies such as currents of swell wave spectra (Zebker & Villasenor, 1992). Cross-track interferometry can be done in two different ways. The first method is to use a single antenna on an aircraft and repeatedly fly over the same area on the ground. By taking the phase difference between two images, an interferogram can be generated. The second method, which was used by Zebker & Goldstein (1986) and is also used on the CCRS airborne SAR system (Gray & Farris-Manning, 1993), is to have an antenna attached to the underside of each wing of the aircraft. Since the SAR system is a side-looking radar system, the distance from one antenna to the surface will be greater than for the other antenna. Both the NASA and the CCRS systems have been successfully used to generate DEM's.

Previous studies have shown that the phase difference between a pair of SAR images is related to terrain height (Zebker & Goldstein, 1986; Zebker et. al., 1994; Hagberg et. al., 1995), to surface changes (Zebker & Villasenor, 1992), and to surface feature movements (Gabriel et. al., 1989; Goldstein et. al., 1993; Massonnet et. al., 1993; Massonnet et. al., 1995;

Vachon et. al., 1996). The last category, surface feature movement, includes 2-dimensional mapping of deformation with high accuracy (cm scale) which is the focus of this research. Applications include earthquake deformation detection and monitoring, monitoring of crustal movements, monitoring volcano inflation and subsidence, and monitoring of land slides and land subsidence (EarthView, 1996b).

4.2.2 InSAR Background

As was mentioned in the previous section, SAR systems measure both the amplitude and phase of a scattered wave as it returns to the receiver. Measurement of the phase can be extremely useful as the following example from Massonnet (1997) will show. Suppose, for example, a satellite radar operates at a frequency of 6 GHz, i.e. a wavelength of 5 cm. If the distance from the radar antenna to a target on the ground is, for example, exactly 800 km, the 1600 km round trip will correspond to a very large, but whole, number of wavelengths. Since the returning wave will have just completed its final cycle the phase will be equal to its original condition when it left the satellite. If, however, the distance to the ground is 800 km plus one centimetre the wave will have to cover an additional two centimetres on it round trip which is 40% of the wavelength. As a result the phase of the reflected wave will be off by 40% when it returns to the satellite, an amount which is easily measured.

Radar interferograms produced in this manner show ground displacement using a series of coloured bands, which resemble the interference fringes from a thin film of oil or

soap (Figure 4.9). One complete set of bands represents a shift of half a wavelength in the distance to the ground since the radar wave must complete a two-way trip. The fringes record only the component of ground displacement in the direction of motion of the satellite or directly away from it (Massonnet, 1997).

If two images are taken of the ground from the exact same location then there will be no phase difference between any corresponding pairs of pixels. However if the scene on the ground changes slightly between passes the phases of some pixels in the second image will have shifted allowing minute movements along the ground to be recorded (Figure 4.10). If the satellite does not return to its exact same position in the second pass then the changing geometry, caused by the different viewing angles, will also introduce phase changes. In this way interferometry can act like a pair of stereoscopic aerial photographs in that variations in topography can be recorded. This topographic effect can be removed by calculating the purely topographic effect and subtracting it. If the topographic contribution is not removed than it will not be possible to measure surface displacement since it is not possible to separate fringes that are caused by topography and fringes that are caused by surface displacement. This will be discussed in detail in the following chapter.

4.2.3 InSAR Geometry

The interferometric technique is similar in some ways to stereo-optical imaging in that two images of the same area, viewed at different angles, are combined to produce a topo-

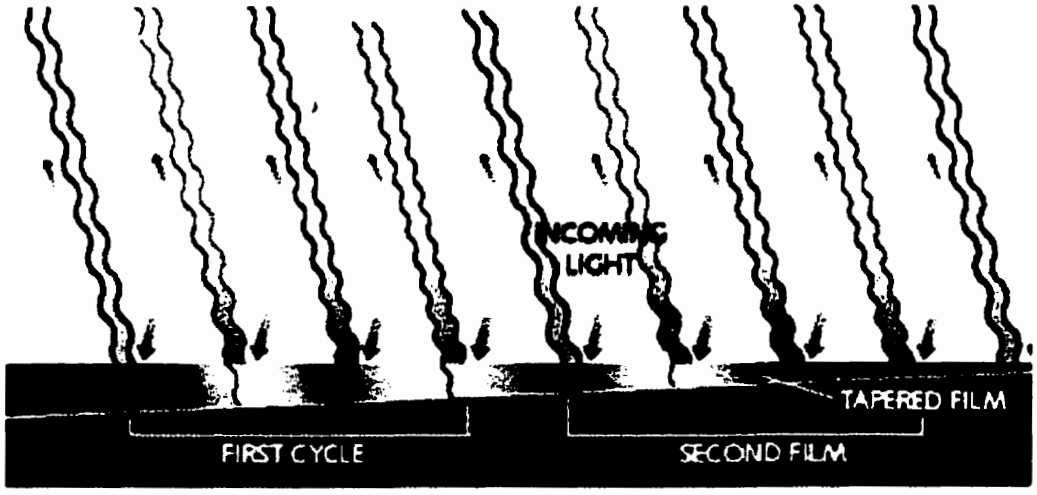

Figure 4.9 Soap film of tapering thickness can separate light into its component colours, each of which corresponds to a particular wavelength of electromagnetic radiation. A fringe of one colour shows where the light rays of that wavelength reflect from the top and bottom surfaces of the thin film and combine constructively (Massonnet, 1997).

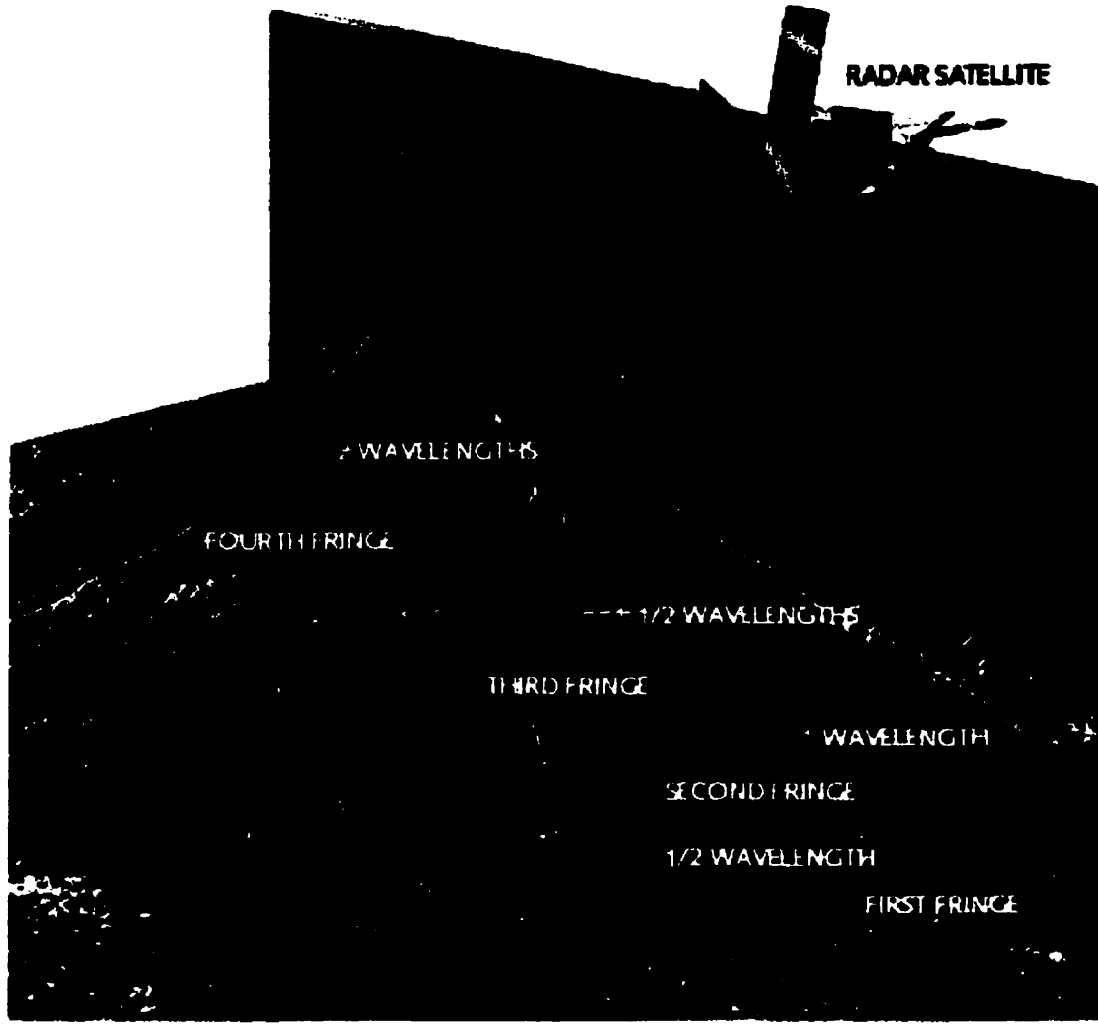

Figure 4.10 Consecutive radar scans from the same position in space create a virtual interference pattern when the crust shifts. Each cycle of coloured fringes corresponds to a change of distance to the satellite of an additional half-wavelength (*detailed enlargements*), which gives one full wavelength in round-trip distance for the radar wave to travel. The fringe patterns shown here draped over the surface indicates a gradual lowering of this mountain (Massonnet, 1997).

graphic image of the surface. The following description of the InSAR geometry and related equations comes from Vachon et. al. (1995). The InSAR geometry in the plane of observation is shown in Figure 4.11. SAR images are acquired at locations 1 and 2 and are processed to complex images $g_1(x, y) = A_1 \exp\{\phi_1\}$ and $g_2(x, y) = A_2 \exp\{\phi_2\}$, where (x, y) represents the azimuth and range coordinates, A_i is the amplitude of SAR signal i, and ϕ_i is the phase of SAR signal i. Also $A_i = A_i(x, y)$ and $\phi_i = \phi_i(x, y)$. Subject to constraints on surface change and orbit separation, which are discussed in Section 4.2.4, the two images may be registered and combined to produce an interferogram

$$s(x, y) = g_1(x, y) g_2^*(x, y) \tag{4.9}$$

where * denotes the complex conjugate.

As mentioned in the previous section, the phase of the interferogram is the phase difference between the two images. The phase Φ is related to the path difference δ between the two imaging locations. Using the geometry of Figure 4.11 the baseline can be defined in terms of the orbit separation B and the tilt angle α. If the baseline is known then the measured difference in the interferogram phase $d\Phi$ between two points may be related to the change in range dR and the change in surface height dz

$$d\Phi = \frac{2kB_n}{R\sin\theta}[dz + \cos\theta dR] = d\phi_z + d\phi_r, \tag{4.10}$$

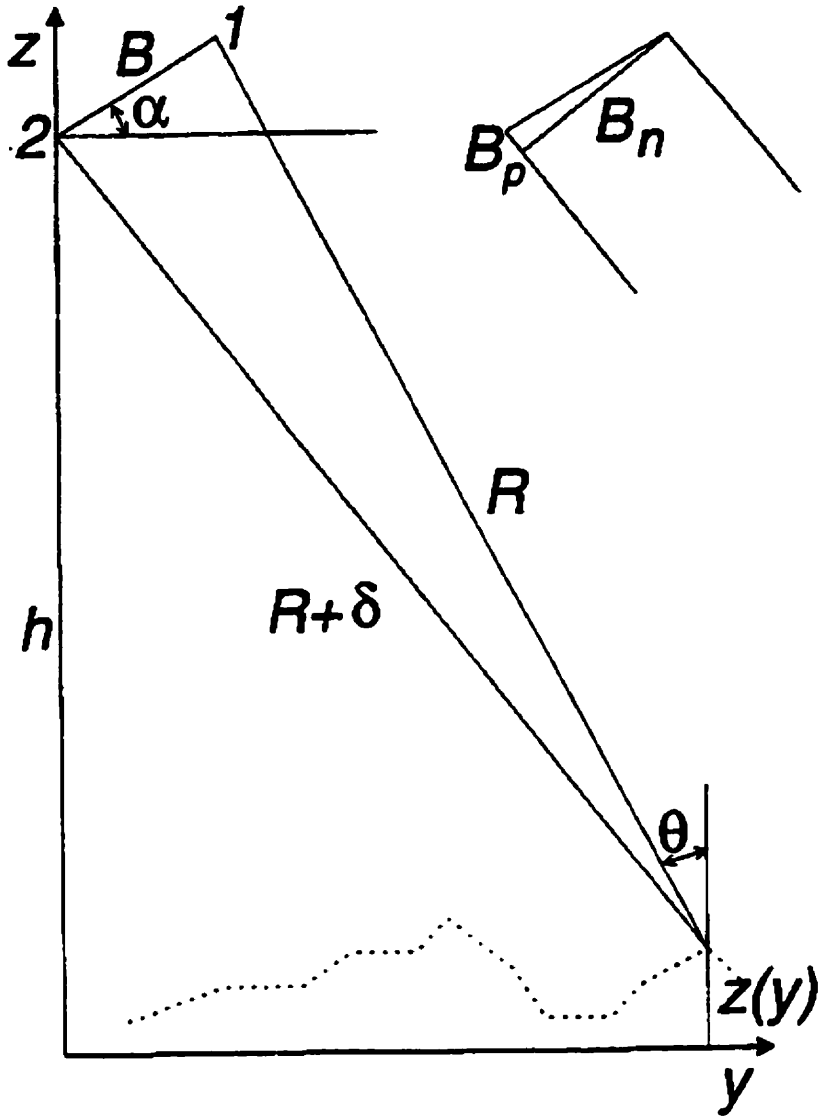

Figure 4.11 Repeat-pass InSAR geometry with a local terrain height of $z(y)$. The inset shows the decomposition of the baseline defined by B and α into its parallel B_p and normal B_n components, under the assumption of parallel rays (Vachon et. al., 1995).

where R is the range to the first point, θ is the local incidence angle, $k = 2\pi/\lambda$ is the radar wavenumber, λ is the radar wavelength, and

$$B_n \sim B\cos(\theta - \alpha) \tag{4.11}$$

is the perpendicular (normal) component of the baseline. The term $d\phi_R$ may be systematically removed from the interferogram leaving only the terrain dependent phase $d\phi_z$. In the interferogram each phase fringe (change in phase from 0 to 2π) represents a relative change in elevation of

$$dz = \frac{\lambda R \sin\theta}{2B_n}. \tag{4.12}$$

4.2.4 Limits for InSAR

Introduction

The primary limitation for InSAR comes from decorrelation (low coherence) between the two images. Radar echoes will be correlated with each other if each represents nearly the same interaction with a scatterer or set of scatterers. Decorrelation can be separated into decorrelation that is dependent on sensor geometry, and decorrelation that is due to actual changes associated with the target. Effects of the sensor geometry will be referred to as spatial in nature and target effects will be referred to as temporal. Of these two types, temporal decorrelation is the one that is of the greatest concern to interferometry. Spatial decorrelation can

be compensated for with the proper orbit geometry but temporal decorrelation is entirely dependent on natural and artificial changes to the earth's surface. These two types of decorrelation can be sub-divided into three sources of decorrelation: decorrelation from surface changes of the individual scattering centres within each resolution element (temporal decorrelation), spatial baseline decorrelation, and spatial decorrelation due to rotation of the targets between observations (Zebker & Villasenor, 1992).

Temporal Decorrelation

To successfully generate an interferogram, the phase between the two images must be well correlated. The coherence is a measure of phase correlation and is defined as

$$\Upsilon(x, y) = \frac{\langle g_1(x, y) g_2^*(x, y) \rangle}{\sqrt{\langle |g_1(x, y)|^2 \rangle \langle |g_2(x, y)|^2 \rangle}} \tag{4.13}$$

where $\langle\rangle$ is the spatial average over a processing window. The coherence lies in the range $0 \leq \gamma \leq 1$. If the coherence is large (close to 1) the phase in the two images is highly correlated, whereas if the coherence is small (close to 0) the phase is not well correlated.

Temporal decorrelation is caused by surface changes between passes which include snowfall, vegetation growth, etc. as well as changes in the electrical and geometrical properties of the surface. Vachon et. al., (1995) studied the effect of temporal decorrelation on scene coherence over two test sites in northern Canada using ERS-1 imagery with a three day repeat period. Vachon et. al., (1995) found that the scene coherence was variable over three day

intervals. The coherence was normally high but for some three day periods it became quite low. Vachon et. al., (1995) also considered the case of increasing the time period between images from three days to 27 days. The coherence was favorable over approximately the first 15 days but then became low after that.

Vachon et. al., (1995) found that the rate of decrease in coherence depends largely on the surface type. Rocky, barren surfaces retained coherence for the longest periods while forested areas showed a rapid decrease in coherence. This can provide information on surface geophysical properties and for land use classification (Askne & Hagberg, 1993). Temporal phase decorrelation can also be caused by low signal-to-noise ratios, phase aberrations in the processing, and heterogeneous atmospheric conditions (Vachon et. al., 1995).

Baseline Decorrelation

While the InSAR method does not require the satellite to return to its exact same position during each pass, it does require that the baseline not be too large. The orbits need to be sufficiently close that the phase interference between different scatterers within one resolution cell change negligibly and speckle no longer limits the possibility of obtaining phase information from each pixel (Askne & Hagberg, 1993). The constraint on the maximum baseline can be expressed in terms of the "celestial footprint" (Prati & Rocca, 1990) and the geometry is shown in Figure 4.12 for flat terrain. The celestial footprint is defined by considering the ground resolution cell as a radiating antenna such that the speckle in the two images

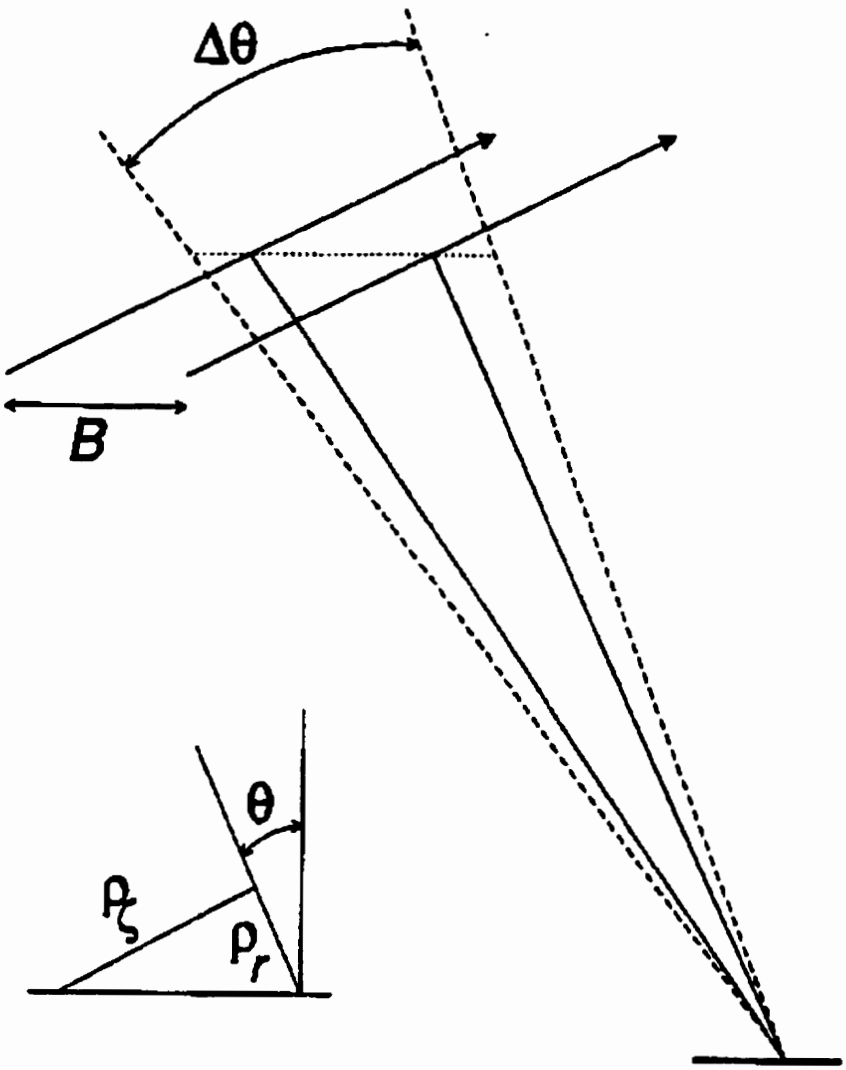

Figure 4.12 The "celestial footprint" for flat terrain. The projection of the slant-range resolution element onto the plane perpendicular to the line-of-sight (shown in the inset) leads to a scattering element of scale ρ_ζ. Both passes must lie within the field of view defined by this radiating element (Vachon et. al., 1995).

remains correlated. This leads to the condition that the trajectory for the two orbits must lie within the angular region defined by

$$\Delta\theta < \frac{\lambda}{2\rho\zeta} \tag{4.14}$$

where $\rho\zeta$ is the size of the resolution cell perpendicular to the radar line-of-sight. Then

$$\rho\zeta = \frac{\rho_r}{\tan\theta} \tag{4.15}$$

where ρ_r is the slant range resolution. Assuming linear FM (chirp) pulse encoding, the compressed slant range resolution is given by

$$\rho_r = \frac{c}{2F} \tag{4.16}$$

where c is the speed of light and F is the chirp bandwidth. The required repeat orbit tolerance is estimated as the maximum normal component of the baseline given by

$$B_n = R\Delta\theta < \frac{\lambda R}{2\rho\zeta} = \frac{\lambda F R \tan\theta}{c} \tag{4.17}$$

(Vachon et. al., 1995).

The phase variation, $\Delta\varphi$, within the interferogram can be given by the following equation

$$\Delta\varphi = \frac{2kB_n}{R\sin\theta}\Delta H + 2k\Delta R + \Delta\Phi + n2\pi \tag{4.18}$$

where R is the slant range distance, B_n is the baseline perpendicular to the line of sight, and θ is the incidence angle. ΔH represents the topographic variations over a reference plane. The second term gives the phase shift due to a small coherent change, ΔR, of the scatterers within a given resolution cell between two acquisitions. $\Delta\Phi$ represents a phase error that is due to randomly changing surface condition, speckle decorrelation due to baseline, volume scattering, and thermal noise. The last term represents the 2π phase ambiguity associated with all interferograms. Eq. 4.18 shows that interferograms made with large baselines will be sensitive to topography, while small baselines will show a high sensitivity to small surface displacements or temporal changes in the phase of the surface reflectivity (Askne & Hagberg, 1993).

Spatial Decorrelation due to Rotation

Decorrelation due to rotation refers to the rotation of targets with respect to the radar look direction i.e. it is not possible to illuminate the same patch on the surface from two different aspect angles and expect the signals to be fully correlated. Consider a resolution element as shown in Figure 4.13. Each scattering centre at polar location (β, γ) rotates to position $(\beta, \gamma + d\gamma)$. Transforming to rectangular coordinates $x = \beta\cos\gamma$, $y = \beta\sin\gamma$ expresses the change in position on the surface as a change in range; if the distance to a point before rotation is $R + \beta\sin\theta\sin\gamma_1$, the distance after a small rotation $d\gamma = \gamma_1 - \gamma_2$ is $R + \beta\sin\theta\sin\gamma_2$, where θ is the incidence angle. As the patch is rotated slightly, the range to and hence phase

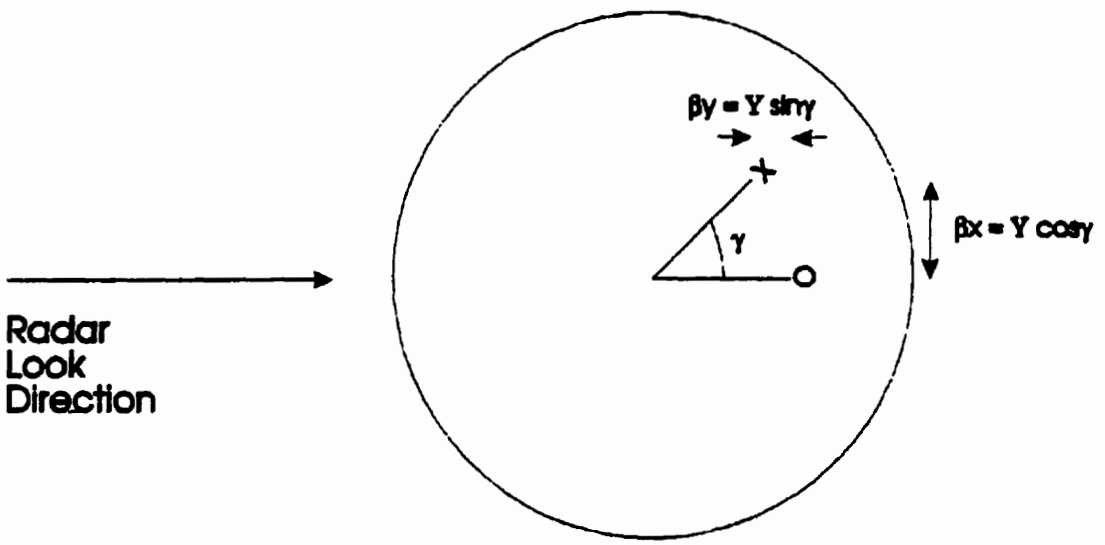

Figure 4.13 Rotation of resolution element by angle γ moves scattering centres from initial position X to new position O. Across-track component of displacement then yields slightly different phase shifts for each scattering centre, resulting in signal decorrelation (modified from Zebker & Villasenor, 1992).

of each scattering centre changes slightly, and the coherence will vary. The following expression for the rotation induced decorrelation can then be used:

$$\Upsilon_{rotation} = 1 - \frac{2\sin\theta |d\gamma| \rho_a}{\lambda} \tag{4.19}$$

(Zebker & Villasenor, 1992).

Surface Slope

To determine the slope sensitivity for a given baseline one can use the following expression for the fringe frequency given by Ulander & Hagberg (1993)

$$\frac{\partial \phi}{\partial R} = \frac{2kB_n}{R\sin\theta} \cdot \frac{\sin u}{\sin(\theta - u)} \tag{4.20}$$

where u is the surface slope in the plane of observation. A measure of the maximum slope, u_{max}, that may be sensed can be derived in terms of the SAR's range resolution ρ_r and the constraint that the rate of change of phase must be adequately sampled - that is, the maximum change in range wavenumber is $2\pi/\rho_r$. Starting from a flat surface ($u = 0$) and tilting the surface toward the radar, the maximum slope that may be unambiguously measured is

$$\tan u_{max} = \frac{\sin\theta}{((2kB_n)/(R\sin\theta))(\rho/(2\pi)) + \cos\theta} \tag{4.21}$$

(Vachon et. al., 1995).

4.2.5 Spectral Misalignment

Surface scattering may be modelled by the complex scene reflectivity, which includes surface properties such as dielectric constant, conductivity, radar wavelength, polarization, surface roughness, and scatterer geometry (Bamler & Schattler, 1993). The SAR data suitable for InSAR are with slightly different imaging geometries. Therefore the SAR data spectra correspond to slightly different frequency bands of the scene reflectivity spectrum (Just & Bamler, 1994). The effect of this spectral misalignment on coherence may be expressed as

$$|\Upsilon_H| = \left(1 - \frac{|\delta f_a|}{F_A}\right) \cdot \left(1 - \frac{|\delta f_r|}{F_R}\right), \tag{4.22}$$

where F_A and F_R are the azimuth and range bandwidths, and δf_a and δf_r are the possible frequency band shifts in azimuth and range (Vachon et. al., 1995) Adaptive bandpass filtering in range and azimuth, as described in the **generate and filter interferogram** processing step in Chapter 5, removes the spectral misalignment decorrelation effect from the interferogram. The has the effect of forcing γ_H to be close to unity.

4.3 SAR Platforms

Currently the four satellites from which we can obtain InSAR data are: RADARSAT (Canadian Space Agency), Japan's JERS-1 (no longer in operation as of October 1998),

and ERS-1 and ERS-2 (European Space Agency). SEASAT also produced SAR data during its brief lifetime but the data was not especially suitable for InSAR applications, although some InSAR studies were carried out using SEASAT data e.g. Gabriel et. al. (1989).

Each satellite has different orbital parameters which are summarized in Table 4.1. RADARSAT and ERS-1/ERS-2 operate with a wavelength of 5.6 cm (C-Band) while JERS-1 SAR operates with a 23.5 cm (L-Band) signal. With a longer wavelength, JERS-1 SAR has better penetration through vegetation canopies than RADARSAT or ERS-1/ERS-2 and has limited penetration through snow. As well the longer wavelength will help increase coherence in JERS-1 images. The repeat orbit period for JERS-1 is however 44 days which greatly increases the chances for temporal decorrelation. In this respect, ERS-1/ERS-2 tandem mode data is the best for interferometry since the images can be obtained only one day apart. However the maximum baseline for ERS-1 and ERS-2 is only about 1 km. RADARSAT has a number of different acquisition modes of which fine beam mode is the most suitable for interferometry. In fine beam mode, the maximum baseline for RADARSAT is about 5 km which is larger than for the other SAR satellites. However, RADARSAT also has a fairly long repeat period, 24 days. This demonstrates that each of the SAR platforms has both advantages and disadvantages for use in InSAR studies.

Parameter			ERS-1 & ERS-2	RADARSAT	JERS-1	SEASAT
platform altitude	h	km	785	798	568	787
wavelength	λ	cm	5.6 (C-Band)	5.6 (C-Band)	23/5 (L-Band)	23.5 (L-Band)
pulse bandwidth	F	MHz	15.55	11.6, 17.3, 30	15	12.75
repeat period		days	1*, 3, 35, or 168 * only available for ERS-1/2 tandem mode	24	44	unknown
maximum base-line	B	km	1	5	4.5	3.3
resolution		m	25	10-100	18	25
swath width		km	100	50-500	75	100
incidence angle	θ		$20° < \theta < 26°$	$20° < \theta < 49°$	35°	23°
polarization			VV	HH	HH	HH

Table 4.1 Table comparing key parameters of ERS-1, ERS-2, RADARSAT, JERS-1, and SEASAT satellite platforms.

CHAPTER 5

Processing of SAR and InSAR Data

5.1 Introduction

A SAR instrument sends out a radar pulse which has various interactions with the ground, some of which scatter the radar back toward the satellite. The backscattered EM pulses are received and digitally sampled by the satellite. The return signal is compared against a reference function (cosine) and the reference function shifted 90° (sine). The results are the in-phase and quadrature components which are distributed as signal data. No corrective processing is performed at this stage so the data is not displayable as an image, it is only raw data (Alaska SAR Facility, 1999).

There are a number of processing steps required in order process raw data to displayable images. These processing steps are complicated and computationally extensive, therefore they will not be described in detail in this thesis. Briefly, the first step is to obtain the preprocessing parameters and convert the slant range distance to ground range. Then processing is carried out in the range and azimuth direction in order to resolve the return signal. Details on these steps can be found in Alaska SAR Facility (1997).

5.1.1 Processing of SAR Data

SAR data are usually delivered in several basic formats once they are processed: scene (SCN), single look complex (SLC), and fully processed. As mentioned in section 4.1.3 speckle is a problem in SAR images due to numerous small reflectors within a particular resolution element on the surface. As was mentioned in section 4.2.1, to overcome this problem the normal method of processing is to reduce statistical noise by averaging the amplitudes of neighbouring pixels. This is known as "taking looks" and the resulting image is referred to as SCN data This will successfully remove a great deal of noise and some simple further processing will remove most of the remaining noise. However averaging destroys the phase information and therefore makes the data sets useless for interferometric applications.

Therefore, for interferometric applications SLC data must be used. For SLC data only one look is used which means that no averaging of the amplitudes of neighbouring pixels is carried out, thereby preserving the phase information. This also means that SLC data are

usually much noisier than the highly processed SCN images. Different processing steps are usually required in order to reduce the amount of noise depending on the application.

5.1.2 Processing of SLC Image Data

To process the SLC image data for this thesis the software package PCIWorks Version 6.2 (PCI, 1997). As mentioned in section 4.2.3 SLC data are complex images, each pixel value has both a real and imaginary component. To reduce the noise in the SLC data the magnitude of the image must be first calculated

$$z = \sqrt{x^2 + y^2} \tag{5.1}$$

where $\bar{z}$ is the magnitude, x is the real component, and y is the imaginary component. The study area image that was processed was a descending mode RADARSAT image acquired on Feb. 19, 1998. Figure 5.1 shows the resulting magnitude image.

Once the magnitude image is obtained, standard speckle filters can be used to filter the data. Many different speckle filters have been developed. For the image in Figure 5.1the enhanced Frost filter was used although similar results could be obtained with any of the standard speckle filters. The algorithm for the Frost filter (Frost et. al., 1982) consists of a circularly symmetric filter with a set of weighting values $m(t)$ for each pixel

$$m(t) = \exp(-A|t|) \tag{5.2}$$

where A is given by,

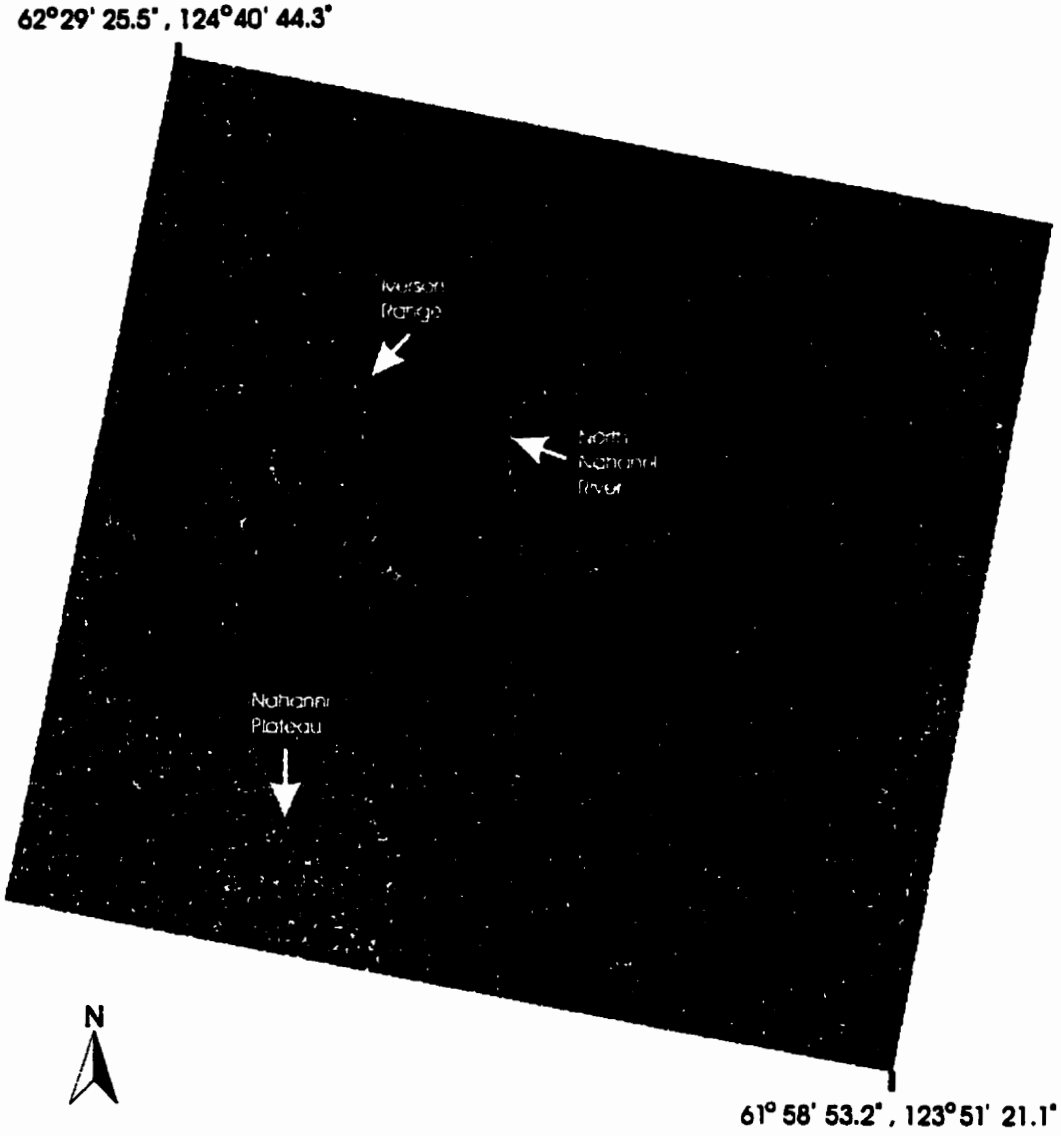

Figure 5.1 Magnitude image of SLC RADARSAT image acquired on Feb. 19, 1998.

$$A = K\frac{Var(z)}{\bar{z}(t)^2} \tag{5.3}$$

where *Var(z)* is the variance of the grey level in the filter window, $\bar{z}(t)^2$ is the square of the mean grey level in the filter window, K is a damping factor, and $|t|$ is the absolute value of the pixel distance from the central pixel to its neighbours in the filter window. The resulting grey level value $\hat{x}(t)$ for the smoothed pixel is

$$\hat{x} = (p_1 m_1 + p_2 m_2 + \ldots + p_n m_n)/(m_1 + m_2 + \ldots + m_n) \tag{5.4}$$

where $p_1 \ldots p_n$ are the grey levels of each pixel in the filter window and $m_1 \ldots m_n$ are the weights for each pixel.

The Frost filter was modified by Lopes et. al. (1990) by dividing the data set into areas belonging to one of three classes. The first of the three classes corresponds to the homogeneous areas in which random noise can be eliminated by applying a low-pass filter. The second class corresponds to heterogeneous areas in which random noise is to be reduced while preserving texture. The third class is areas containing point targets where the filter should preserve the observed value (Shi & Fung, 1994). The model is formulated as follows

$$m(t) = \exp[-Kfunc(C_I(t))|t|] \tag{5.5}$$

where $func(C_I(t))$ is a hyperbolic function of $C_I(t)$ defined as follows (Shi & Fung, 1994)

$$func(C_I(t)) = \begin{cases} 0, for(C_I \le C_v) \\ (C_I(t) - C_v)/(C_{max} - C_I(t)), for(C_v < C_I(t) < C_{max}) \\ \infty, for(C_I \ge C_{max}) \end{cases} \quad (5.6)$$

where C_v and $C_I(t)$ are the variation coefficients of the noise and data set respectively, and C_{max} is the maximum of the noise variation coefficient (Shi & Fung, 1994). The variation coefficients simply measure how homogeneous the area under the filtering mask is. If the variation coefficient is low than the area is homogeneous, if the variation coefficient is high than the area is not homogeneous.

If the enhanced Frost filter is compared with the Frost filter it can easily be seen that at the two extremes (i.e. homogeneous area class and isolated point target class) the output is forced to be equal to the averaged value and the observed value without filtering, respectively. For the heterogeneous class the original filter responses are exaggerated by the hyperbolic function to satisfy the requirement that "the more heterogeneous an area is, the less it has to be smoothed" (Shi & Fung, 1994). Figure 5.2 shows the image from Figure 5.1 filtered using the enhanced Frost filter using a damping factor of 1 and the number of looks set equal to 1. The effect that the speckle filtering had is evident in a comparison of the two images. Fine detail is much more readily discernible in the filtered image, particularly features in the southeast portion of the image.

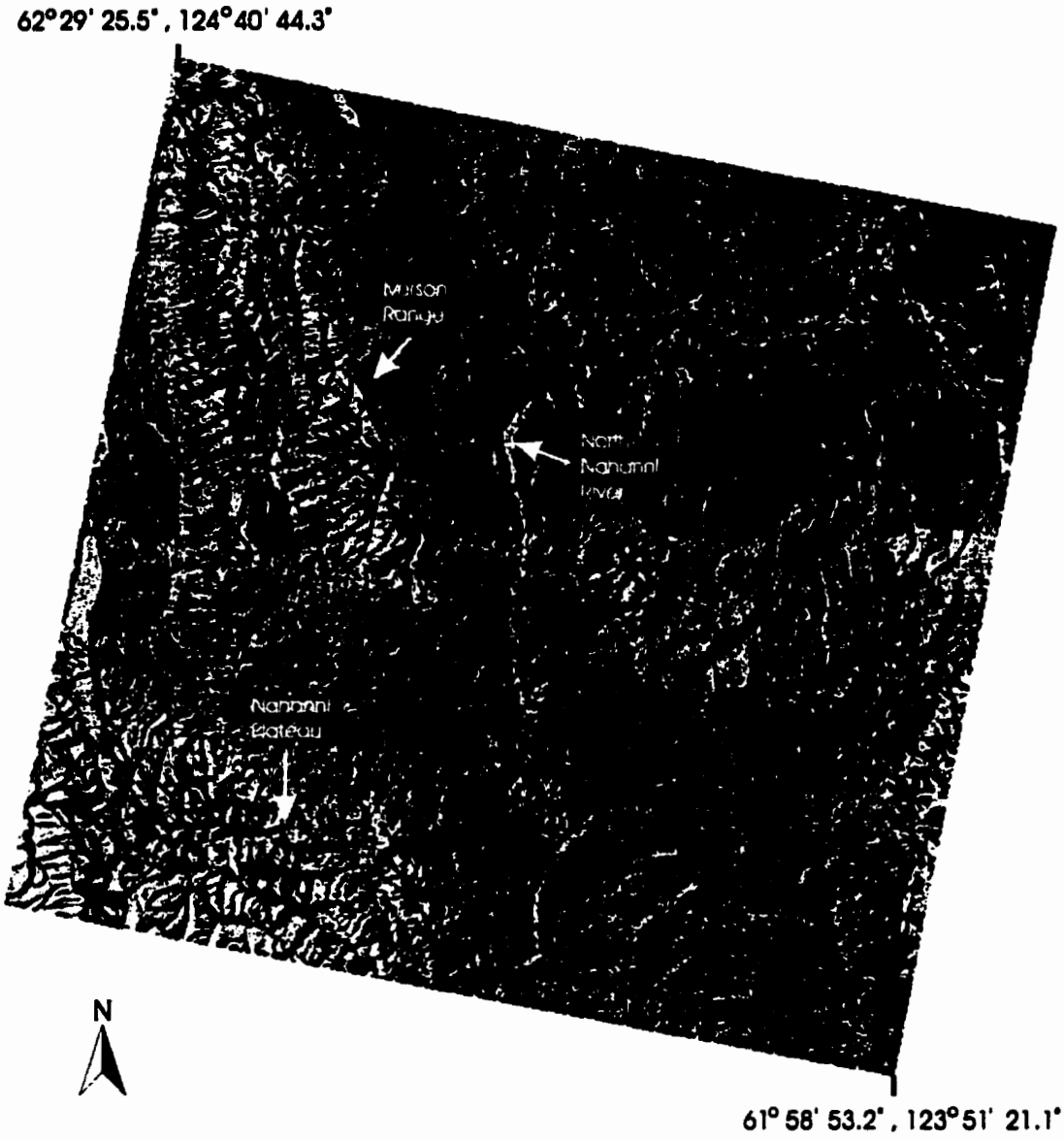

Figure 5.2 Magnitude image from Figure 5.1 filtered using the Enhanced Frost filter.

5.2 Processing of InSAR Data

There is a broad range of application for SAR interferometry. InSAR can be used for highly accurate elevation mapping (creating digital elevation models). InSAR can also be used for monitoring surface changes such as deforestation. Since forests will generally cause low coherence an area that has been heavily deforested will exhibit a much higher coherence that it had when there were trees present. Differential interferometry can be used to monitor cm scale ground displacements due to earthquakes, volcano inflation and deflation, or glacier movement. For differential interferometry the topographic contribution must be removed so that any resulting fringe pattern will be related to surface displacement only.

5.2.1 Introduction

Generating differential interferograms (the interferogram with the topographic contribution removed) and DEM's from SLC data sets involves a number of data processing stages. To process the data sets used in this thesis the software package EarthView Version 4.4.1, developed by Atlantis Scientific Inc. was used. This software package contains the InSAR Version 1.1 software module which contains a set of data processing tools that combine two SLC SAR images to create differential interferograms and DEM's

The processing steps needed to generate DEM's with EarthView are shown in Figure 5.3, and the processing steps required to generate differential interferometry products are

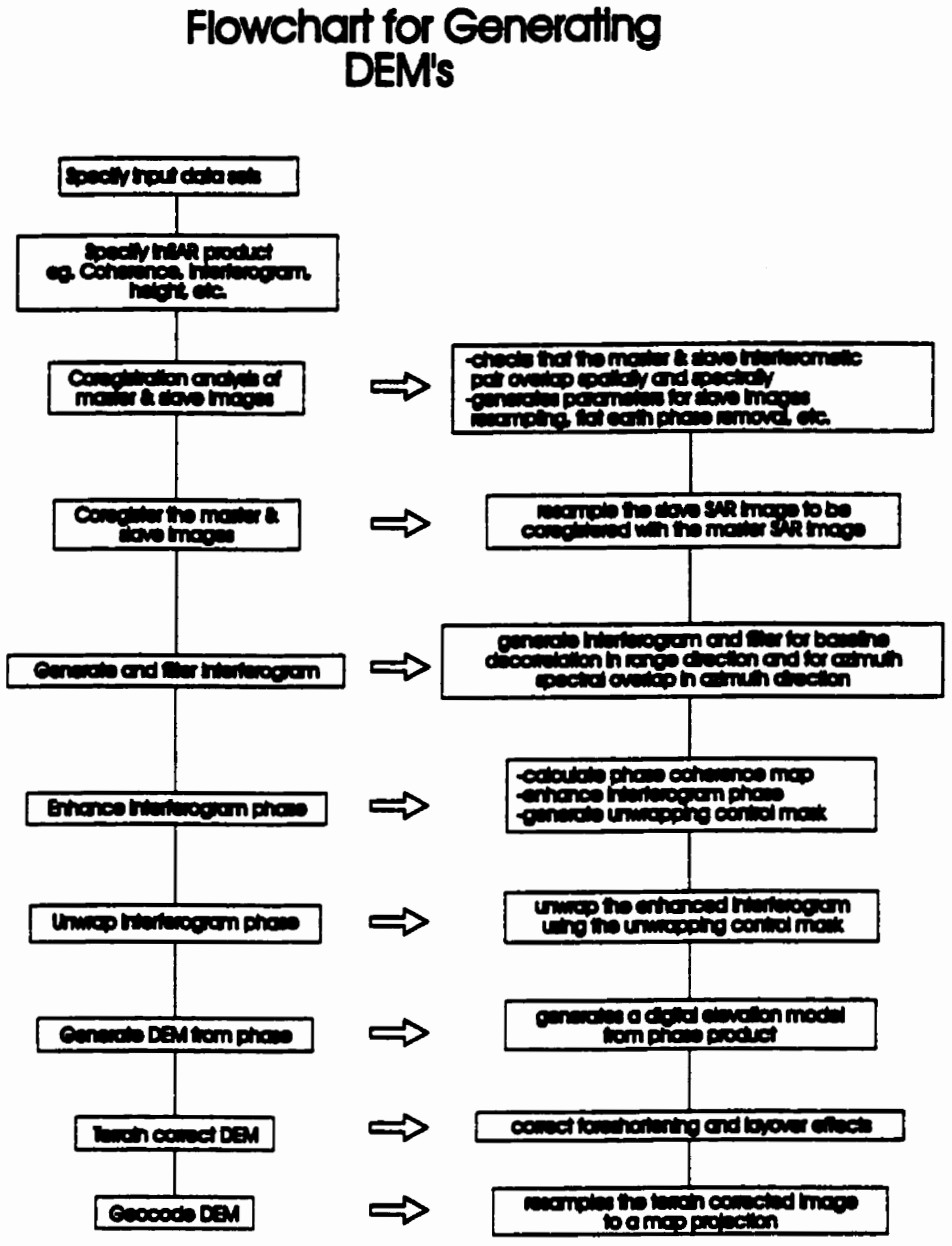

Figure 5.3 Processing steps required for generating DEM's using EarthView (modified from EarthView, 1996b).

shown in Figure 5.4. All of the processing steps required for generating differential interferometry products are the same as the DEM's except for the added step of coregistering the external DEM with the Master SAR image. This section will discuss in detail the processing steps required to generate both a differential interferogram and a DEM.

5.2.2 Processing Steps For Generating Interferograms

The processing steps discussed here will be referred to as in Figure 5.4. In many of the steps there are a number of important details and these will be discussed in each section. There are three different projections to present the data:

- **Slant Range** which is the original slant range/azimuth SAR projection of the master SAR image, no elevation corrections have been made to these data;
- **Terrain Corrected** where the InSAR products will be corrected for SAR image distortions such as layover and foreshortening, however the image is still in slant range/azimuth coordinates and;
- **Geocoded** where the terrain corrected image is resampled to a map projection.

5.2.3 Specify Input Data Sets

The obvious first step in generating an interferogram and a subsequent DEM is to specify the input data sets. Two SLC image data are required to generate phase images and they are arbitrarily referred to as the "master image" and the "slave image". Each SLC data set

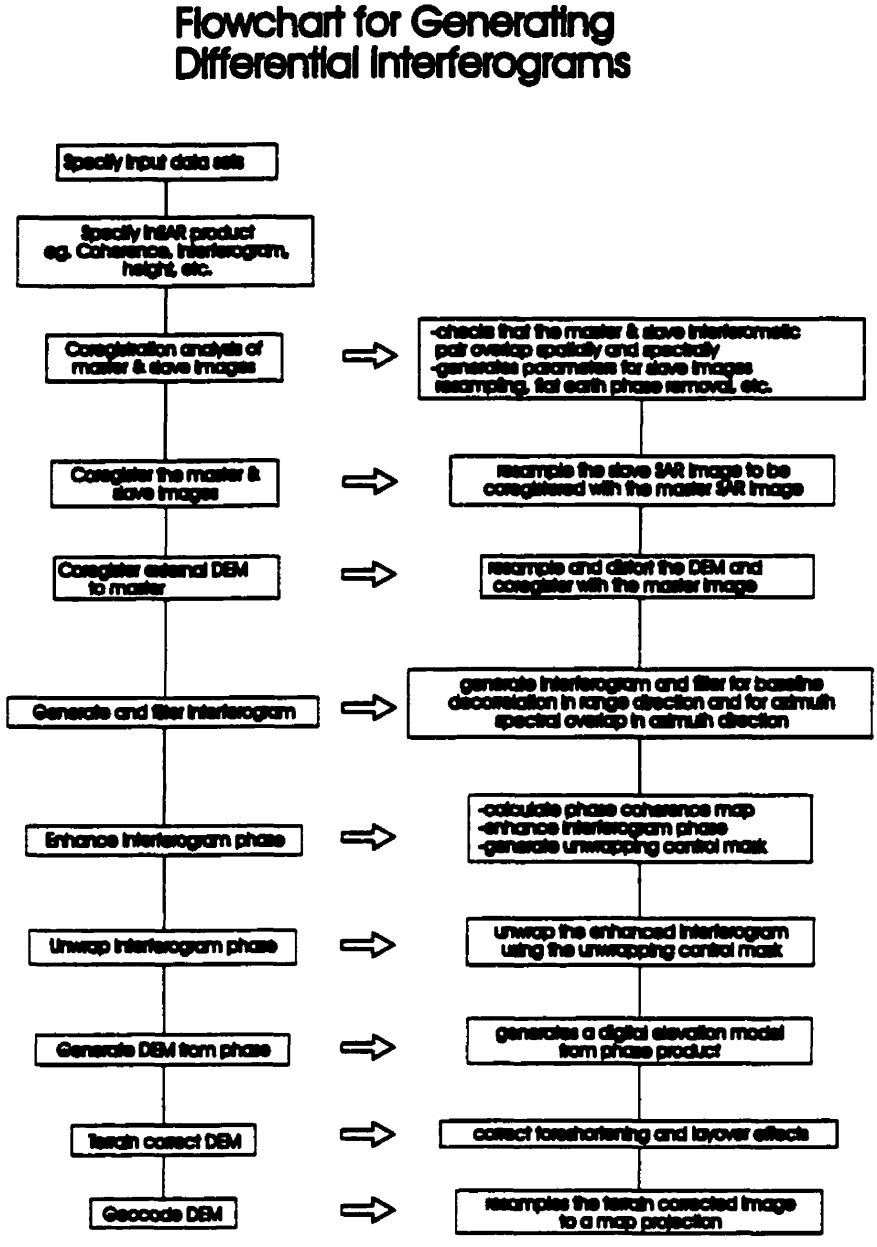

Figure 5.4 Processing steps required for generating differential interferometry products using EarthView. The only step beyond that needed for generating DEM's is the coregistration of the external DEM to the master SAR image (modified from EarthView, 1996b).

consists of four files: the volume file, the leader file, the image file, and the trailer file. The volume file lists the size of the other three files as well as information pertaining to the orbit and the scene location. The leader and trailer files contain in-depth information about the image required for determining the latitude and longitude of each pixel in the image which is necessary for determining tie points and geocoding the image. The image file contains the actual SLC data array.

5.2.4 Specifying of the InSAR Product Option

Next the desired InSAR products must be specified. A number of options are available but the ones most commonly used are the interferogram which displays the actual fringe pattern, the height which displays the height across the area as compared with a reference point, and the coherence which displays the coherence across the selected region.

5.2.5 Coregistration Analysis of the InSAR Data Pair

Coregistration analysis is the step where the processing actually begins. There are three main steps in coregistration analysis. The first is to check the master and slave interferometric data pair for spatial and spectral overlap Overlapping spatially simply means that both images cover the same area on the surface. Spectral overlap depends on the complex scene reflectivity mentioned in section 4.2.5. Coregistration analysis checks to make sure that these

spectra are not too different. If either the percentage of spatial or spectral overlap falls below a certain level specified by the user, coregistration will fail.

The second step in coregistration analysis is to generate a set of bi-cubic spline coefficients for

- resampling the slave image
- removing the flat earth phase (phase changes that are present over a flat area on the surface)
- conversion of phase to height: $(dh)/(d\phi)$
- conversion of slant range to height: $(dR)/(dh)$.

These parameters are calculated over an equally spaced grid of points on the area of overlap between the master and slave images. The predicted coregistration will be $(r2 - r1)(r1, t1)$ and $(t2 - t1)(r1, t1)$ where $(r1, t1)$ and $(r2, t2)$ are as shown in Figure 5.5. The parameters are calculated over a equally spaced grid of points on the area of overlap between the master and slave images. A typical grid is shown in Figure 5.6a. This creates a master point grid where each point is a tiepoint between the two images.

The third step involved in coregistration analysis is coregistration refinement analysis which refines the coregistration bi-cubic spline parameters. To accomplish this a series of patches, centred on each tiepoint, are set up on the master and slave images. A cross-correlation of corresponding patches is carried out to determine the fine coregistration to within a fraction of a pixel and resulting in one true tiepoint for each patch. To avoid phase errors the

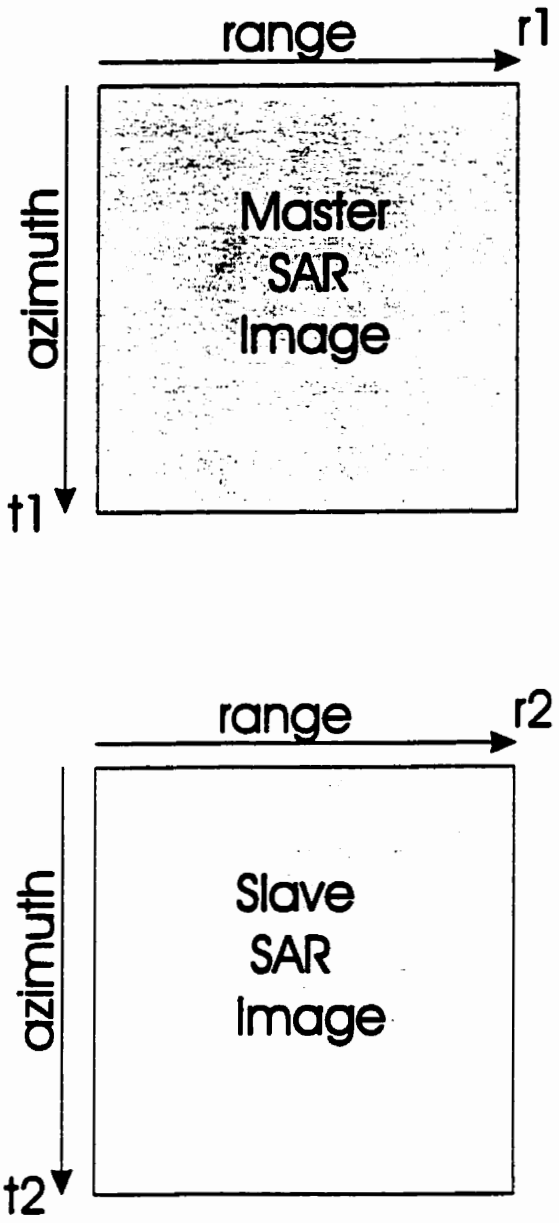

Figure 5.5 ($r1$, $t1$) are the range and azimuth coordinates in the master SAR image and ($r2$, $t2$) are the range and azimuth coordinates in the slave SAR image (modified from EarthView, 1996b).

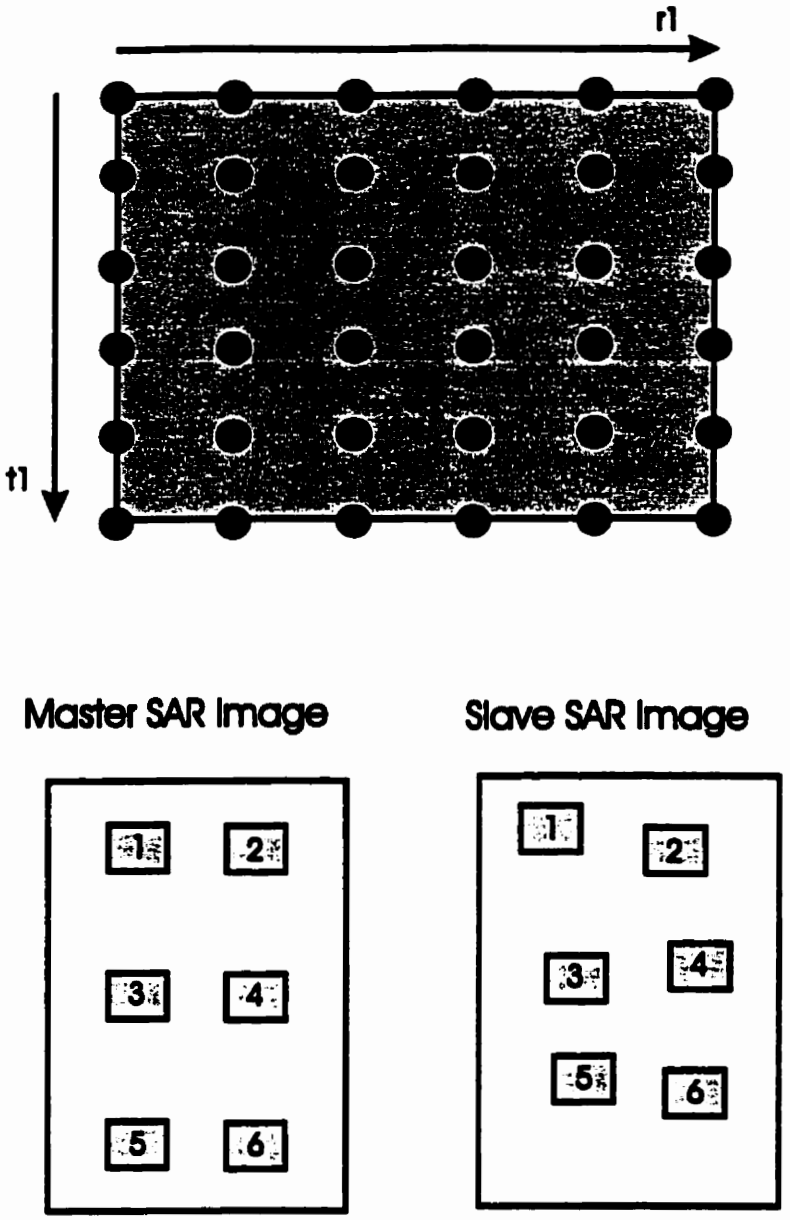

Figure 5.6 (*top*) Typical grid of points used to create tiepoints between the master and slave SAR images. A 6×6 grid is normally sufficient. (*bottom*) A sample patch layout for the master and slave SAR images. Each patch is centred over a tiepoint and a cross-correlation of corresponding patches is carried out to determine the fine coregistration (modified from EarthView, 1996b).

coregistration must be accurate to about 1/4 of a pixel. A sample patch layout is shown in Figure 5.6b. It is important to ensure that there are many tiepoints over coherent areas so a greater number of patches is normally used if there are large areas of low coherence.

Occasionally there arises a problem in which the orbit vector data is not very accurate and there is a large difference between the predicted and the refined image tiepoints. In this case the coregistration refinement may fail due to a insufficient number of tiepoints. There are two possible methods to deal with this. One method is to simply use a manual bias. The relationship between the master and slave images may resemble something like Figure 5.7. The row and column coordinates for the same point on the surface may differ greatly between the two images. The bias can be estimated by viewing the master and slave images and recording the row and column positions for the same point in each of the images. The range bias is then ($r2$ - $r1$) and the azimuth bias is ($t2$ - $t1$) where ($r1$, $t1$) = (col, row) in the master image and ($r2$, $t2$) = (col, row) in the slave image.

The second method is manual image tiepointing. If this option is used then the master and slave images will be displayed and the user can mark a series of control points across the images. Manual tiepointing is a labour intensive process since the user must attempt to locate the same pixel in each image. It can take several hours to locate a number of tiepoints that are spread over the entire image. This option is rarely needed since using a manual bias will normally be sufficient for correcting any orbit vector errors (EarthView, 1996b).

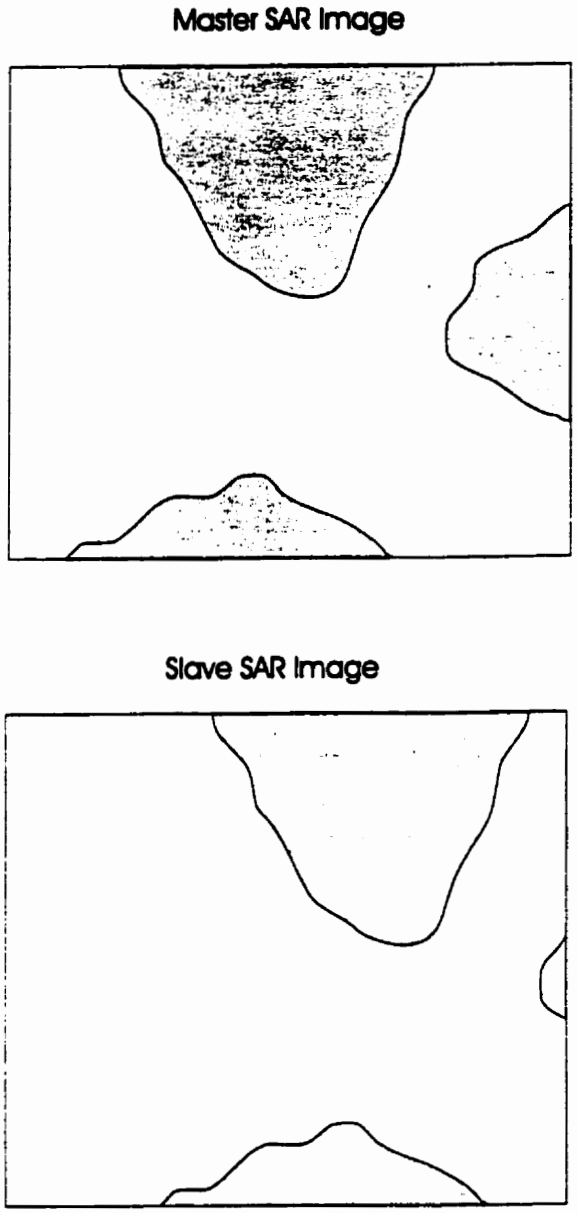

Figure 5.7 Relationship between the master and slave SAR images when a manual bias is required. The row and column coordinates for the same point on the surface may be much different between both images.

5.2.6 Coregistration

Up to this point the master and slave images have been checked for spatial and spectral overlap and parameters have been generated for coregistration. The next step is to resample the slave image and coregister it with the master image. The resampling is carried out in two passes, first in the range direction and then in the azimuth direction. A $(\sin x)/x$ interpolation kernel is used with a length of $(2m + 1)$ where m is set by the user. The interpolation kernels are calculated for fractions of a pixel displacement. One sample interval is divided into $1/N$ subintervals where N is the precision value selected by the user. Each pixel in the slave image is matched with the corresponding pixel in the master image so that the slave image is stretched and warped so that it fits as exactly as possible with the master image.

5.3 Interferograms

At this point the interferogram is ready to be generated. The interferogram is generated by multiplying one complex data set by the complex conjugate of a second complex data set. This will give the phase difference between the two data sets. The resulting interferogram is displayed as a series of coloured fringes. Each cycle of fringes from red through blue will correspond to a change in elevation which depends on the altitude of the satellite, wavelength, baseline, and incidence angle. DEM's can created from interferograms in this manner once the phase has been unwrapped, and if the topographic effect is removed, differential interfero-

grams can be created which will show surface displacement. Coherence levels will affect the quality of interferograms to a large degree. If the coherence is high there will be possible to obtain clear fringes and accurate elevations. If the coherence is low then the interferogram will be noisy and it will not be possible to obtain clear fringes and accurate elevations.

5.4 Summary

Coregistration of the master and slave images is a crucial step for InSAR. The two images must be coregistered pixel by pixel as accurately as possible to avoid any phase errors which will affect the resulting interferogram. If the coherence is low then accurate coregistration becomes even more important in order to reduce the areas of low coherence. In Chapter 6 the remaining processing steps will be described. The external DEM is coregistered with the master SAR image in order to remove the topographic effect and the interferogram is generated. Phase unwrapping is then carried out, this is described in detail in 6.3.4, and then the DEM is generated from the phase. After this the image is corrected for terrain effects and is geocoded.

CHAPTER 6

InSAR Applications

Chapter 5 detailed some of the data processing steps such as the filtering of SLC data in order to remove speckle using the enhanced Frost filter. Chapter 5 also discussed the data processing steps used by EarthView Version 4.4.1 to coregister two SLC images so that each pixel in the slave image is matched with the corresponding pixel in the master image. In this chapter the remaining data processing steps required for generating differential interferograms and DEM's will be first discussed and then are followed by how they can be applied to earthquake related tectonics research.

6.1 Earthquake Tectonic Applications

SAR interferometry has been shown to be a valuable tool in quantitatively monitoring earthquake related surface changes (i.e. Massonnet et. al., 1993, Peltzer & Rosen, 1995) because of its ability to detect centimetre scale ground displacement. Earthquake displacement is traditionally detected using ground based geodetic techniques but these require an extensive survey network to be in place before an earthquake occurs. Satellite data can be collected at regular intervals and therefore can detect co-seismic displacement without advance knowledge of the earthquake's location. In order to detect earthquake related surface changes however the topographic effect must be subtracted so that any fringes that are visible will be due strictly to ground displacement. If the topographic contribution is not subtracted the interferogram can be used to create highly accurate DEM's. This chapter will also discuss coregistering an external DEM with the master SAR image in order to remove the topographic effect, and also other important steps such as phase unwrapping.

6.2 Data Processing

6.2.1 Coregister External DEM to Master SAR Image

This is the only step that is performed for differential interferometry which is not required for generating a DEM. It is one of the most important steps for differential interfer-

ometry. In this step the external DEM is pixel-by-pixel coregistered with the master SAR image in order to remove the topographic effect. The DEM must be resampled, stretched, and warped to have the same layover and foreshortening effects as the master SAR image. Figure 6.1 shows an example of how the master SAR image and the DEM may appear and the DEM has to be coregistered to the master image.

There are three ways to create differential interferograms:

1. Two-pass differential interferometry. Two SLC images are used to create an interferogram, and a geocoded DEM from an external source, i.e. a digitized map, is used to remove the topographic contribution.
2. Three-pass differential interferometry. This method requires a set of three SLC images. Image 1 is acquired at an earlier date than image 2 which is acquired at an earlier date than image 3. Image 1 and image 2 are used to create a DEM, then image 1 and 3 are used to create a differential interferogram using the DEM from image 1 and 2. The resulting differential interferogram will show ground displacement between the times image 2 and image 3 were acquired. In this case the DEM does not need to be geocoded.
3. Four-pass differential interferometry. Two SLC images are used to create a geocoded DEM. A differential interferogram is then created using two other SLC images and the geocoded DEM.

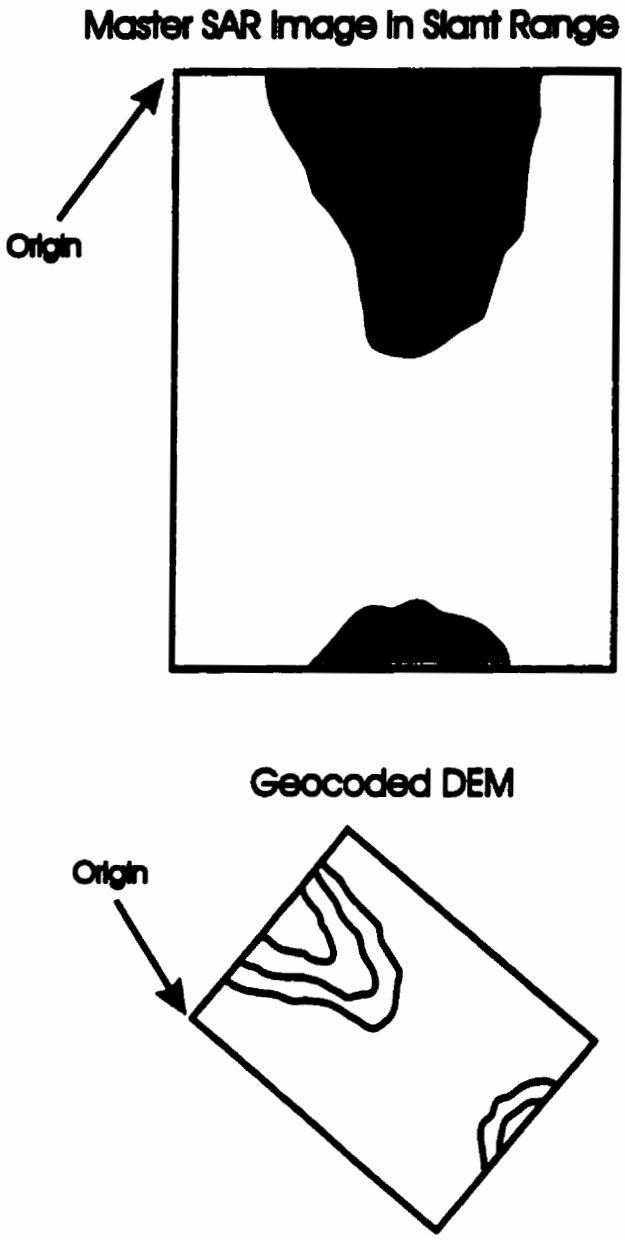

Figure 6.1 Relationship between the master SAR image in slant range/azimuth coordinates and the geocoded DEM. The DEM must be stretched and warped to fit as exactly as possible over the master SAR image (modified from EarthView, 1996b).

The following description applies to the two-pass and four-pass differential interferometry cases. The input external DEM will be in geocoded format where the georeferencing is in the appropriate input data format. Before the coregistration can take place the user must mark a bias tiepoint between the master SAR image and the DEM. This can be difficult if there are no features that are clearly displayed in both the master and the DEM. The coregistration step uses only latitude and longitude information to coregister the external DEM to the master SAR image. There are often significant errors in the georeferencing of the SAR imagery and so it is necessary to do a fine coregistration of the external DEM to the master SAR image. To do this, a synthetic SAR image is created in slant range/azimuth coordinates which can be used to coregister the DEM with the master SAR image. The user selects tiepoints between the master SAR image and the synthetic SAR image or the DEM. This can also be a difficult task if there are no easily recognizable features between the master SAR image and the synthetic SAR image. Often more than one attempt is necessary to try and coregister the DEM with the master SAR image. The registration must be done as accurately as possible in order to remove as much of the topographic effect as possible.

After the topographic effect has been removed it is possible that there may still be some residual topographic information left in the interferogram. This is possible for the two-, three-, and four-pass differential interferometry cases. The residual topographic information may be due to errors in the coregistration of the DEM to the master, or errors in the baseline modelling which resulted in a slightly incorrect $(dh)/(d\phi)$ relationship. There may be some residual flat Earth phase that needs to be removed. Flat Earth phase can be observed in areas

that are known to be flat but contain regular fringe patterns. This can be removed by using the **Residual Phase Correction** tool. Areas dominated by flat Earth phase are marked and the phase gradient is calculated and subtracted. The **Differential Phase Correction** tool is then used to adjust the perpendicular baseline and observe the effect of the topographic phase removal (EarthView, 1996b).

6.2.2 Generate and Filter the Interferogram

Due to the complex scene reflectivity there will be some spectral misalignment between the two images. In the range direction, the shift of the frequency bands caused by the complex scene reflectivity will cause what is known as baseline decorrelation. If the baseline does not exceed the maximum allowed baseline for the particular platform, adaptive bandpass filtering can be carried out in the range direction to remove the baseline decorrelation effect. This will result in identical frequency bands for the ground reflectivity spectrum (Vachon et. al., 1995).

There is a similar situation in the azimuth direction in the case of non-parallel orbit trajectories. Typically the master and slave images will be acquired with different antenna viewing angles and the images will be processed independently using their specific Doppler centroid frequencies. Therefore spectral misalignment in the azimuth direction will result. If the difference in Doppler centroid frequencies is not too large this decorrelation contribution

can be corrected by bandpass filtering the complex image pair using a procedure similar to that carried out for the range direction (Vachon et. al., 1995).

6.2.3 Enhancement of Interferogram Phase

The main functions of enhancing the interferogram phase are to:

- calculate a phase coherence map,
- enhance the interferogram phase in preparation for the phase unwrapping,
- generate an unwrapping control mask (UCM), and
- apply a data reduction.

In the "enhance interferogram phase" step an averaging window is passed over the selected portions of the master and slave SAR images. The data is subsampled, normally only in azimuth, to result in nearly square ground range pixels. This will result in an aspect ratio, k, in azimuth. The coherence, enhanced interferogram, and UCM will be calculated on the new grid. The total number of pixels in the averaging window will be r in range and $r \bullet k$ in azimuth where r is specified by the user and k is the aspect ratio. For low coherence interferograms a large value of r ($r \geq 100$) is needed to get accurate values for the coherence and to distinguish between areas of noise and very low coherence.

The averaging window is adaptively expanded or contracted depending on the local estimate of the phase standard deviation. This controls the phase residue density by keeping it

constant and independent of the phase coherence level. The maximum and minimum window filter size is specified by the user with a larger window size being used for low coherence interferograms. A Gaussian window weighting is also applied to the filter window. The window weights are $e^{-((2x)/(Nr))2}$ where x is the distance from the centre of the window and Nr is the specified window size.

6.2.4 Phase Unwrapping

Phase unwrapping is one of the most important steps in obtaining a DEM from an interferogram. The topography is directly related to the phase however the phase is only measured modulo 2π. The phase diagram, Figure 6.2a, illustrates what is meant by this. If one moves counterclockwise from the origin O to the labelled point you have moved a distance of $\pi/2$. However one could continue moving around the circle for a distance of $(5\pi)/2$ and end up back at the same point. One can continue this for $(9\pi)/2$, etc., i.e. the phase keeps wrapping around on itself. To calculate the elevation of each point in an image the correct number of phase cycles must be added to each phase measurement, i.e. the phase must be unwrapped.

This correction can also be considered in a numerical sense by looking at the one-dimensional sequence of phases in Figure 6.2b. It is clear that one cycle should be added to the last three entries in order to eliminate the discontinuity. This is the essence of phase unwrapping. For interferometry the phase unwrapping must be carried out in two dimensions but the basic idea is the same.

(a)

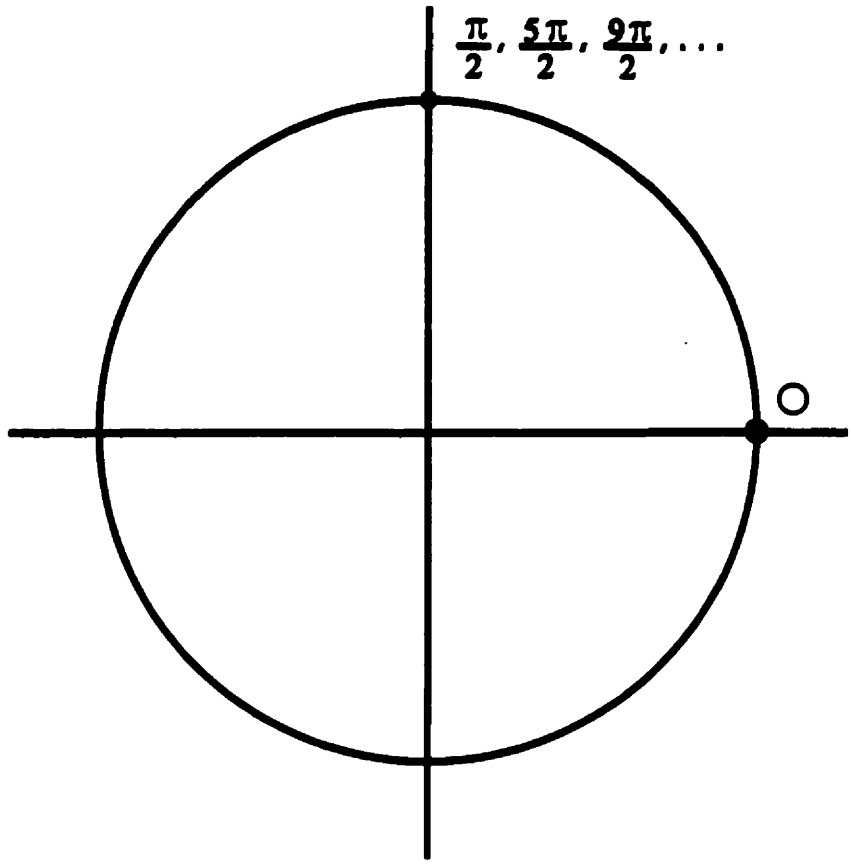

(b)

. . ., 0.5, 0.6, 0.7, 0.8, 0.9, 0.0, 0.1, 0.2, . . .

Figure 6.2 (a) Graphical representation of the phase wrapping around on itself. Starting at the origin O and moving counter-clockwise, moving by $\pi/2$, $(5\pi)/2$, $(9\pi)/2$, etc. will always return you to the same point, i.e. the phase keeps wrapping around on itself. (b) A one-dimensional sequence of phases. One cycle should be added to the last three entries to eliminate the discontinuity

A number of phase unwrapping algorithms have been proposed and can be broadly categorized into integration methods i.e. branch-and-cut method, and Least-Squares (LS) techniques (Just et. al., 1995). Simple integration would give the absolute phase distribution except for the presence of noise and phase jumps of more than $\pm\pi$ in the interferometric signal. These jumps introduce phase inconsistencies which result in absolute phase values which are dependent on the integration path. One method of dealing with these phase inconsistencies or residues is to mark them and try to integrate properly around, but not enclosing, them. This is the standard phase unwrapping technique introduced by Goldstein et. al., (1988) (Just et. al., 1995).

The LS approach to phase unwrapping obtains an unwrapped solution by minimizing the differences between the discrete partial derivatives of the wrapped phase data and the discrete partial derivatives of the unwrapped solution (Pritt, 1995). In other words, phase values that are known to be corrupted due to layover, speckle, temporal decorrelation, etc., are given a weight of zero so they do not affect the phase unwrapping. A LS solution using the Poisson equation is used to unwrap the phase (Pritt, 1995).

The main purpose of the unwrap interferogram phase stage is to phase unwrap the enhanced interferogram using the UCM generated in the "enhance interferogram phase" step. The phase unwrapping algorithm used in EarthView minimizes the length of phase discontinuities in the unwrapped phase image which will minimize the severity of unwrapping errors. The algorithm used is referred to as the Iterative Disk Masking phase unwrapping algorithm.

This method applies circular or elliptical disks centred on phase residues (discontinuities) and pixels of low coherence. A number of phase unwrapping cycles are performed in which the disks are enlarged in the first cycle until no phase unwrapping discontinuities are detected. In the second and subsequent cycles the size of the disk masks are reduced according to specified parameters. The disks are iteratively shrunk until the minimum disk radius as specified by the user is reached.

The image is divided into a number of tiles and each tile is unwrapped separately within a cycle. This is an advantage since if the entire image was unwrapped at once, then one localized area which required large unwrapping disks would cause the entire image to have large disks during the first cycle. It is also more efficient for dealing with large images. The user sets a starting and final coherence threshold such that if a pixel is below the threshold it is masked by a disk of a radius specified by the user. When a low coherence pixel is masked by a disk, the disk's radius is enlarged by an amount specified by the user for each unwrapping cycle. The disk is enlarged until no phase unwrapping errors are found. The disk masks are then shrunk down by a user specified amount for each unwrapping cycle until the minimum radius is reached, after which the disk masks remain constant in size (EarthView, 1996b).

Phase Unwrapping Tool

EarthView allows a manual interaction with the unwrapping control mask to allow the re-unwrapping of image subsections. This allows the user to analyze the quality of the unwrapping result and repair it if necessary. Erroneous discontinuities might occur, particu-

larly in low coherent interferograms or in mountainous terrain. This is especially important for RADARSAT and JERS-1 images over the Nahanni region as well as for ERS-1/ERS-2 images which are not tandem mode images. However, if a large number of discontinuities are present it is likely that the coherence is very low and high quality results will be difficult, if not impossible, to obtain. The time required to carry out the phase unwrapping procedure will depend on the size of the image, the satellite type, and the number of discontinuities present. RADARSAT images take a significantly longer to phase unwrap than ERS images. This is due to the larger incidence angle that RADARSAT uses (B. Armour, per. comm.). ERS images normally require several hours to phase unwrap while RADARSAT images can take up to 2-3 days.

6.2.5 DEM from Interferogram Phase

The final step for the slant range projection is to generate a DEM from the interferogram phase. In this step the phase values are mapped to height values. The phase unwrapping algorithm interpolates over small areas of low coherence so that the interpolated phase areas are also mapped to height. The user selects a coherence threshold and values either above or below the threshold are mapped to height. Normally the coherence threshold is set to 0 and all phase values above the coherence threshold are used. The height and height change are calculated in metres.

6.2.6 Terrain Correction

In this stage foreshortening and layover effects are corrected, however the image is still in slant range/azimuth coordinates. Layover effects are corrected by sweeping up and down the slant range direction and detecting areas of repeating slant range values. These are marked in the mask image. The calculations use the local height of each pixel as obtained from the DEM image. Foreshortening effects can be compensated for by spreading data representing the mountains facing side into more pixels and compacting returns from the back face into fewer pixels.

6.2.7 Geocoding of InSAR Results

The final stage in generating differential InSAR products and DEM's is to geocode the InSAR results. The user has a choice of a number of different map projections which include latitude/longitude (default), stereographic, UPS, LCC, transverse mercator, and UTM. The latitude and longitude for the terrain corrected image is calculated using orbit/earth geometry. Therefore the georeferencing of the final image product will be only as good as the georeferencing of the input image data. The data are normally resampled using a linear interpolation kernel function although other higher order polynomials can be used as well as a cubic spline. The final geocoded product is oriented so that north is straight up to the top of the monitor or page.

6.3 An Alternative Approach: DEM's From Stereo Image Pairs

Computing DEM's from phase unwrapped interferograms is a new approach which is still being developed. At this point, it will be instructional to review the traditional method of obtaining DEM's from stereo image pairs. In the stereo image pair method both optical image data as well as high resolution SAR data can be used. Stereo image pairs requires two airphotos of the same area on the ground taken at slightly different viewing angles. The relative positions of features lying closer to the camera (at higher elevation) will change more between these two views than the positions of features farther from the camera (at lower elevation). This change in relative position is referred to as parallax at can be used to determine object heights and terrain elevations (Lillesand & Kiefer, 1994).

DEM's are created from airphotos using an instrument called an orthoscope which consists of two projectors. Two airphotos are loaded in and are adjusted in their position and angular orientation to duplicate the exact relative positions and orientation of the aerial camera at the instants the two photos were acquired. The stereo model is projected onto a tracing table with contains a floating mark whose elevation can be adjusted and is related to terrain elevations. The orthophotos alone do not convey topographic information however. They are used as base maps for contour line overlays prepared separately. When the contour information is overprinted on the orthophoto a topographic orthophoto is created. This entire process can be carried out digitally in order to create DEM's (Lillesand & Kiefer, 1994).

6.4 Summary

Phase unwrapping is still an area of ongoing research. Many phase unwrapping algorithms have been proposed and are being refined and there will no doubt be new algorithms developed in the future. This is an important research area for InSAR since shadow zones, areas of layover, and low coherence regions will cause discontinuities which will create problems for phase unwrapping. Proper phase unwrapping is vital for creating accurate DEM's and for monitoring surface deformation. Because of these problems, computing DEM's from the interferogram phase image requires further research and development before it can be as robust as the stereo image pair methods.

CHAPTER 7

Discussion

7.1 General Description

Figure 7.1 shows a RADARSAT image of the North Nahanni River area acquired on Feb. 19, 1998. This image gives a good overall view of the study area showing all of the major features. It has been geocorrected so that north is pointing up towards the top of the page. From a SAR image it is generally not possible to determine the species of vegetation cover but the major structural features stand out very well. The study area can be basically divided into two sections by the North Nahanni River. The eastern half of the image consists of the Great Slave Plain which is relatively flat with no significant topographic features. The western half of the image

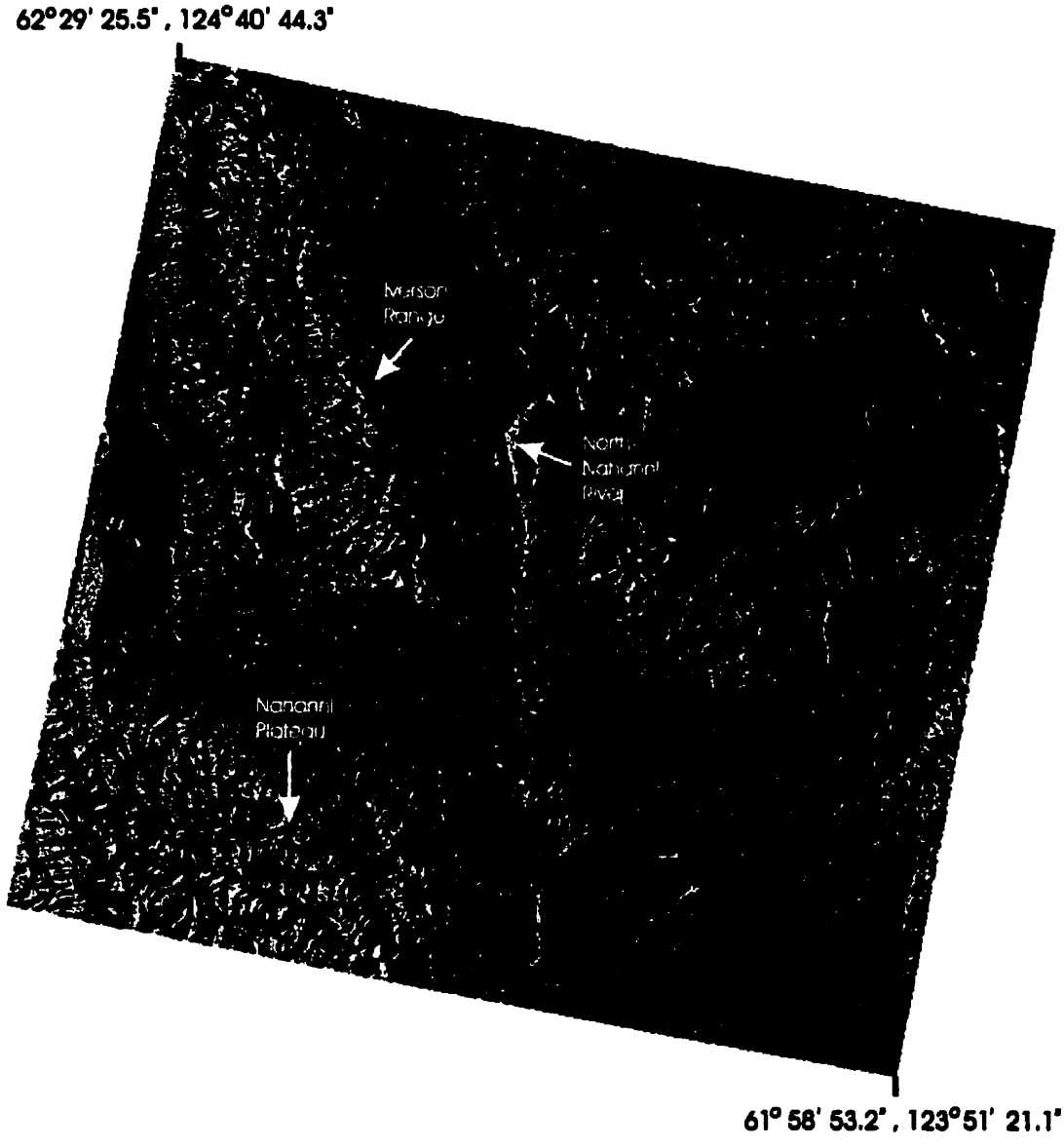

Figure 7.1 RADARSAT image of the North Nahanni River area acquired on Feb. 19, 1998. Some of the major features are indicated on the image.

contains the Iverson Range and the Nahanni Plateau. Here the elevations are much higher than in the eastern half of the image and the terrain is much more rugged. The Mackenzie Mountains are located to the west of the Iverson Range just off of the edge of the image. The rivers in the area generally flow in a north-south or east-west direction.

7.2 DEM Comparison

DEM'S from three different sources were compared with a 1:50 000 map of the North Nahanni River area. The three DEM's used were: a DEM provided by Geomatics Canada (shown in Figure 7.2); a DEM created from a pair of RADARSAT images acquired on Feb. 19, 1998 and Mar. 15, 1998 (the master SAR image is shown in Figure 7.3, the coherence image in Figure 7.4, the DEM in Figure 7.5, and the interferogram in Figure 7.6); and a DEM created from a pair of ERS-1 images acquired on Aug. 12, 1991 and Aug. 15, 1991 (the master SAR image is shown in Figure 7.7, the coherence image in Figure 7.8, the DEM in Figure 7.9, and the interferogram in Figure 7.10). ERS-1 images have a range resolution of 20 m and a azimuth resolution of 30 m which means that the ERS-1 images may appear to be stretched somewhat in the azimuth direction compared with the range direction.

The coherence images show that the ERS-1 image pair has excellent coherence across the entire image. The flat regions in the eastern part of the image have coherence levels around 0.8, on a scale of 0-1, while the mountainous regions have coherence levels around 0.6 with localized areas having much higher coherence values. The few regions with low coher-

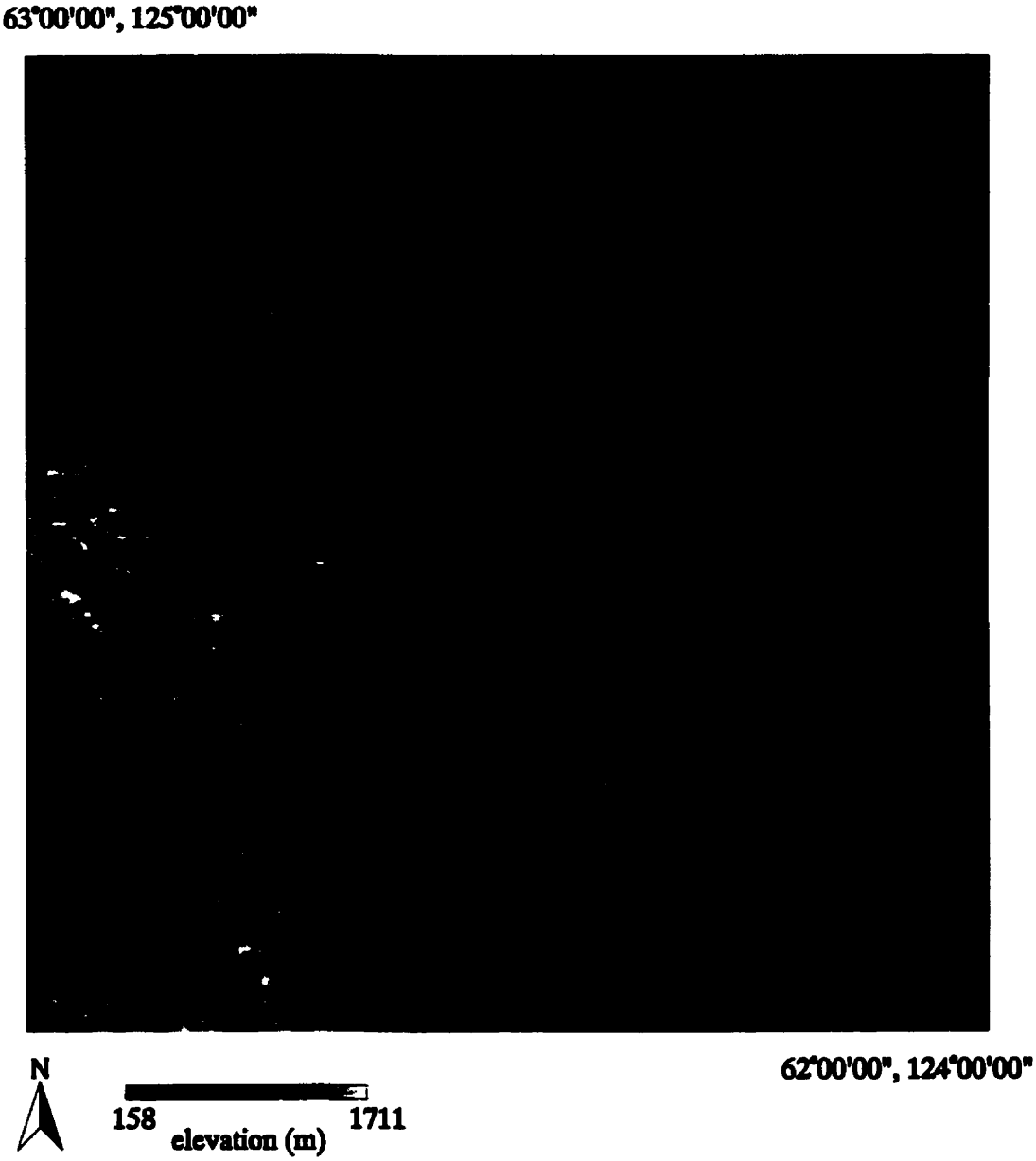

Figure 7.2 DEM provided by Geomatics Canada. Coordinates of the upper left and lower right corners are shown.

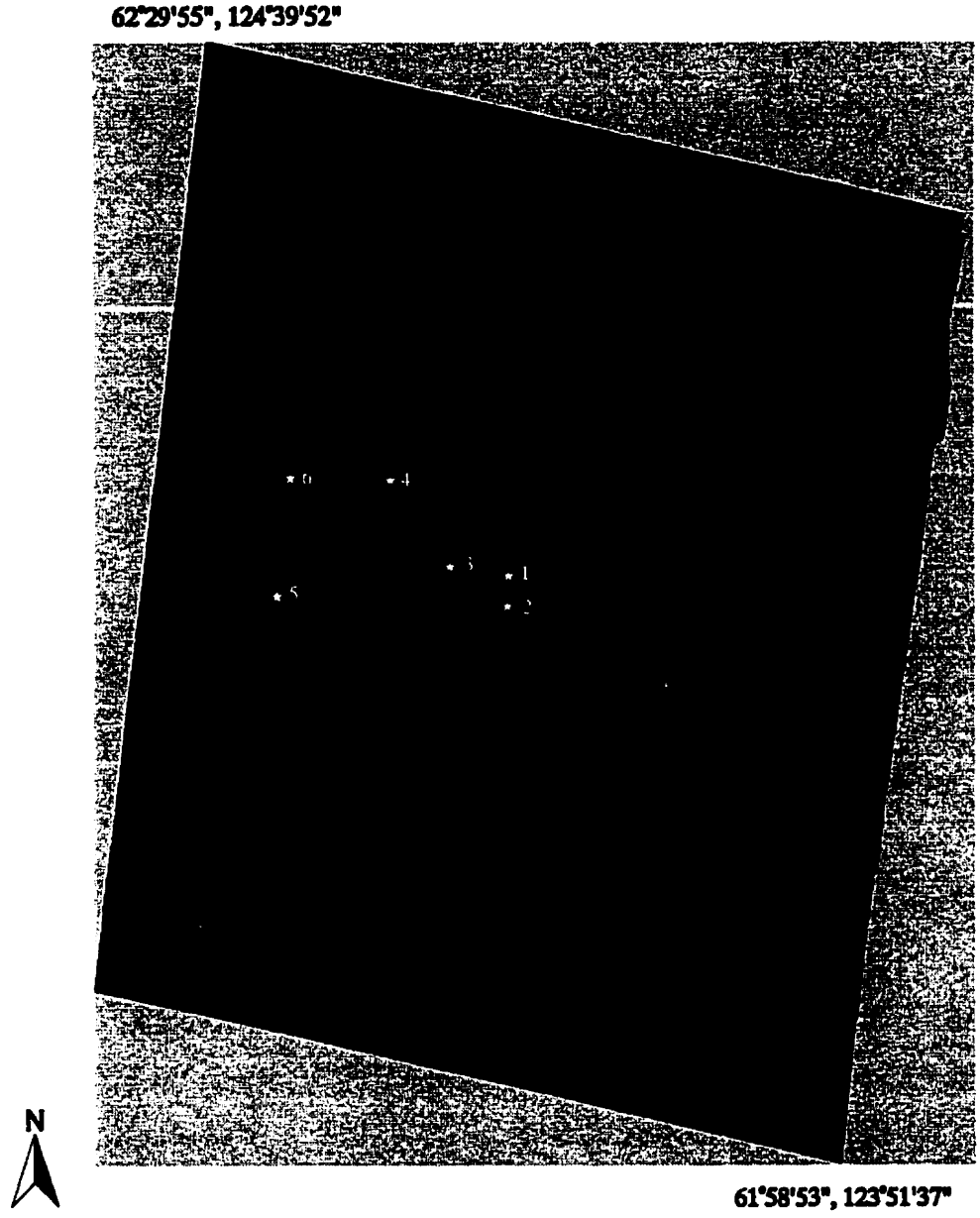

Figure 7.3 Master SAR image for the Feb. 19/Mar. 15, 1998 RADARSAT image pair. Coordinates for the upper left and lower right corners are shown.

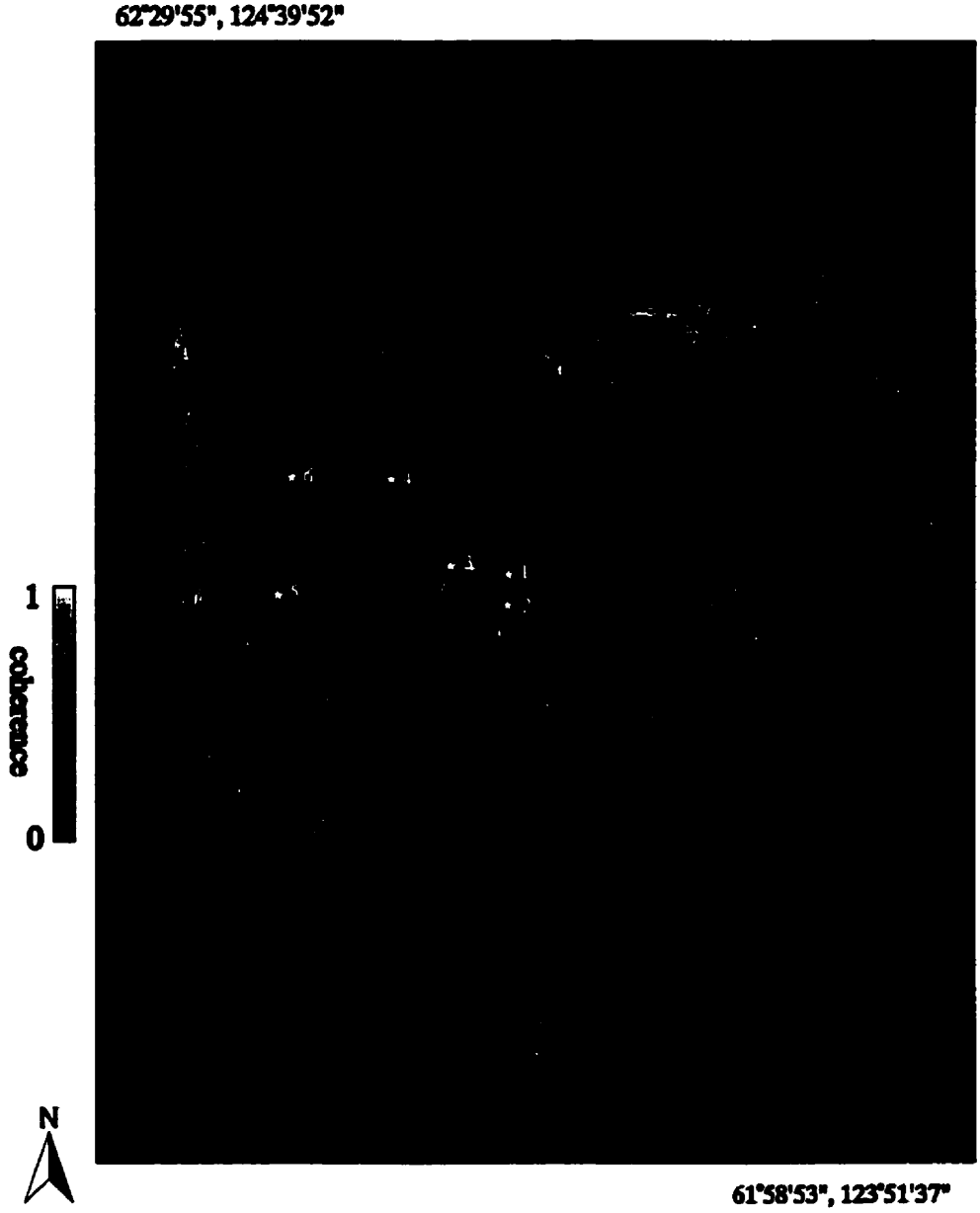

Figure 7.4 Coherence image for the Feb. 19/Mar. 15, 1998 RADARSAT image pair.

Figure 7.5 DEM created from the Feb. 19/Mar. 15, 1998 RADARSAT image pair.

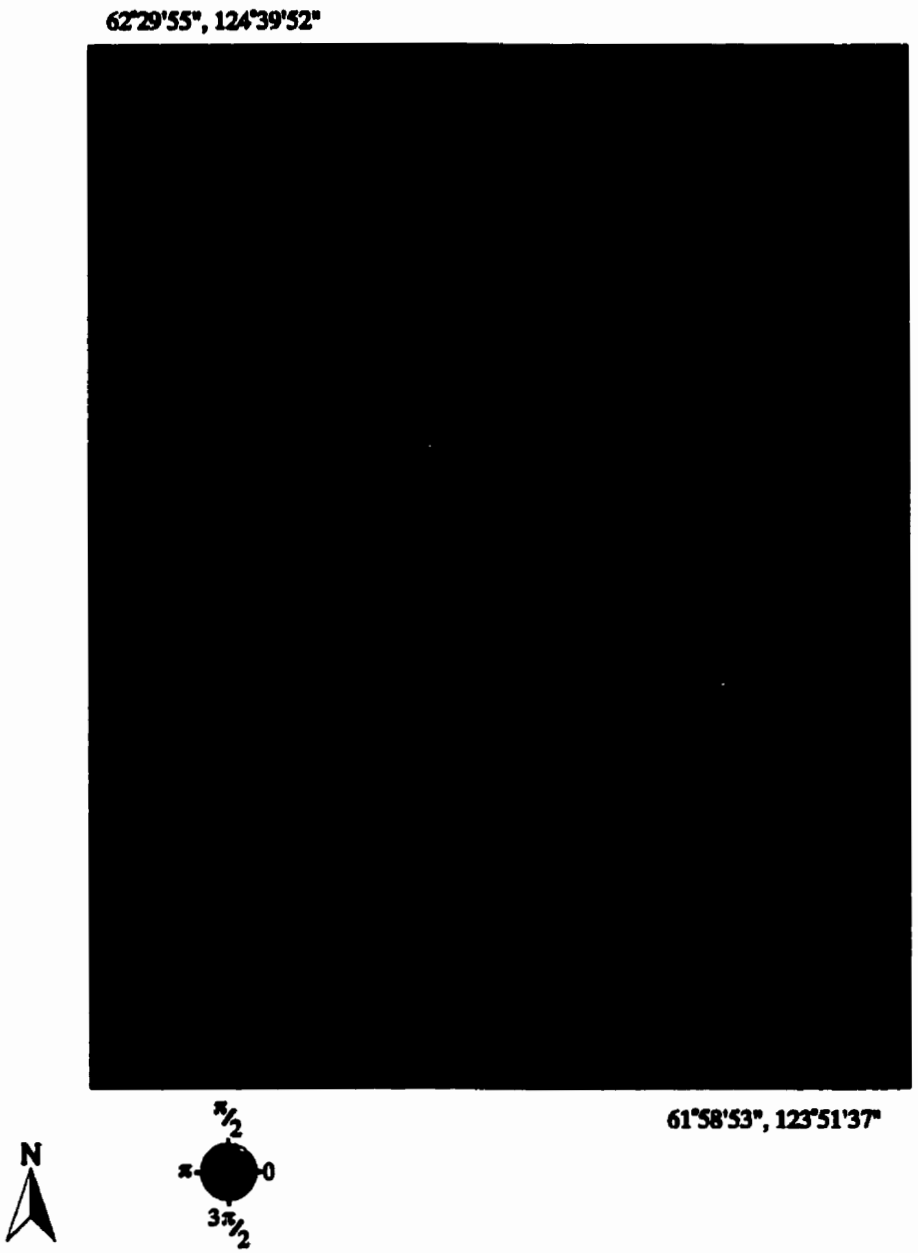

Figure 7.6 Interferogram created from the Feb. 19/Mar. 15, 1998 RADARSAT image pair.

62°53'59", 123°50'33"

N

61°42'03", 124°58'22"

Figure 7.7 Geocoded master SAR image for the Aug. 12/Aug. 15, 1991 ERS-1 image pair. Coordinates for the upper right and lower left corners are shown.

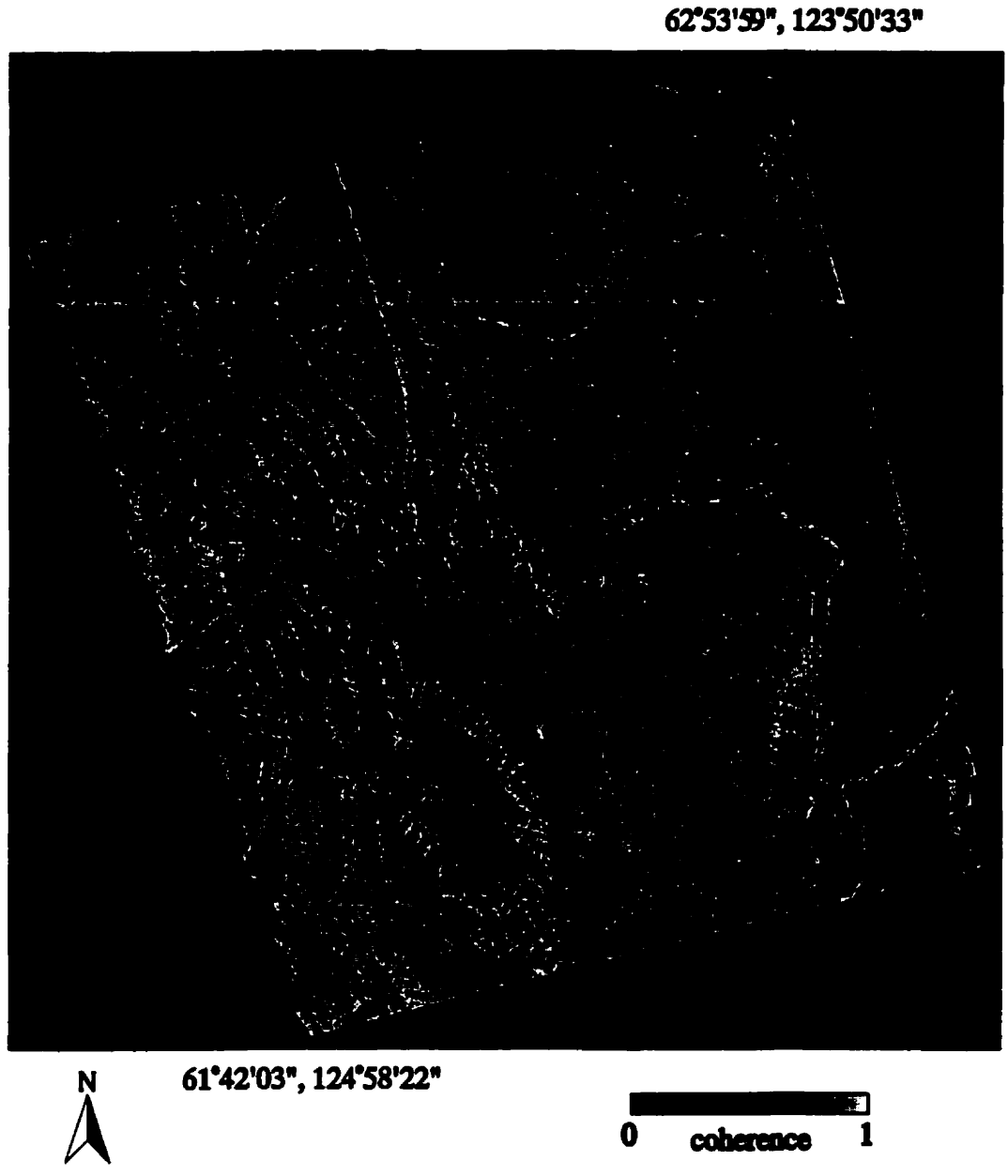

Figure 7.8 Coherence image for the Aug. 12/Aug. 15, 1991 ERS-1 image pair.

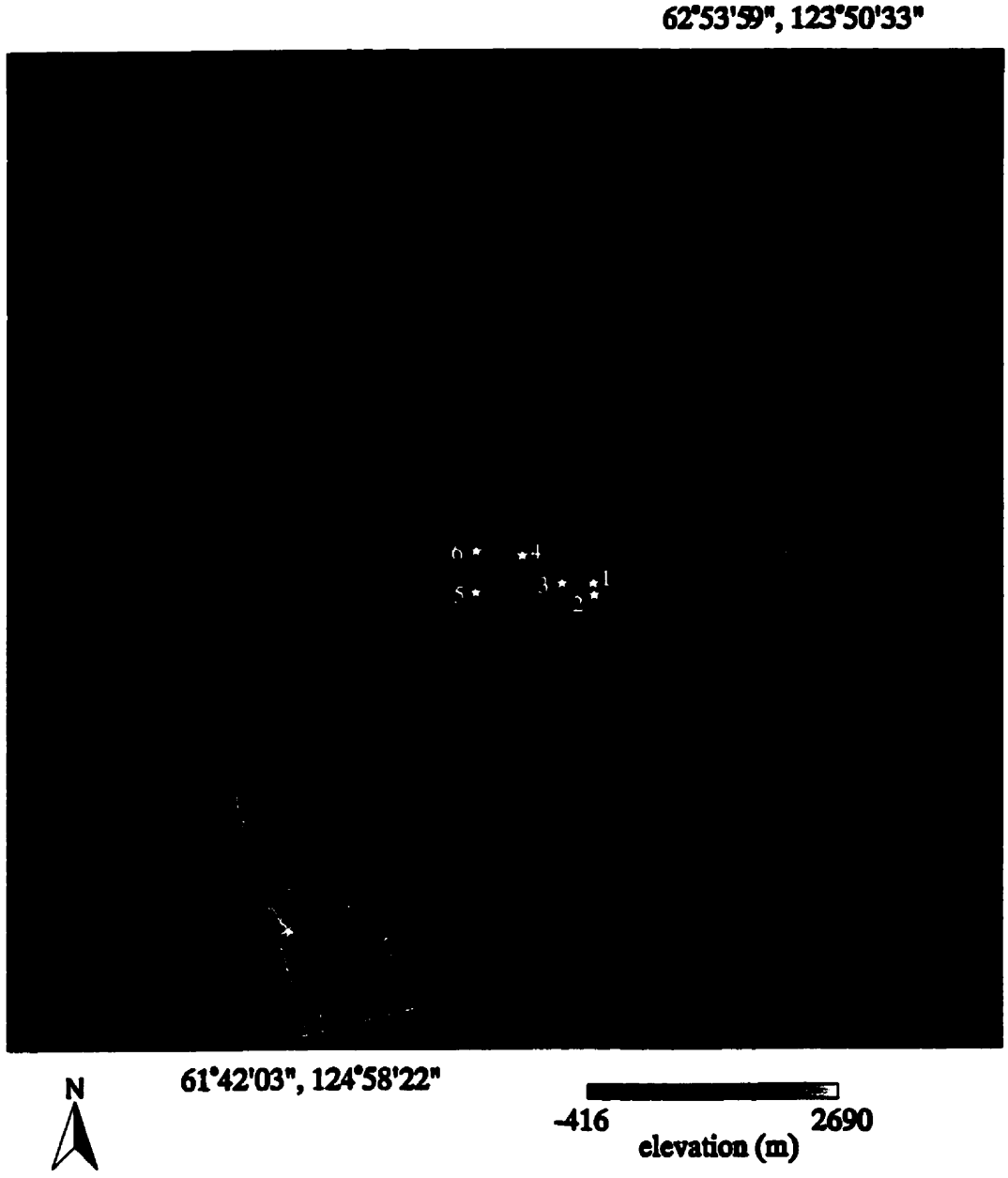

Figure 7.9 DEM created from the Aug. 12/Aug. 15, 1991 ERS-1 image pair.

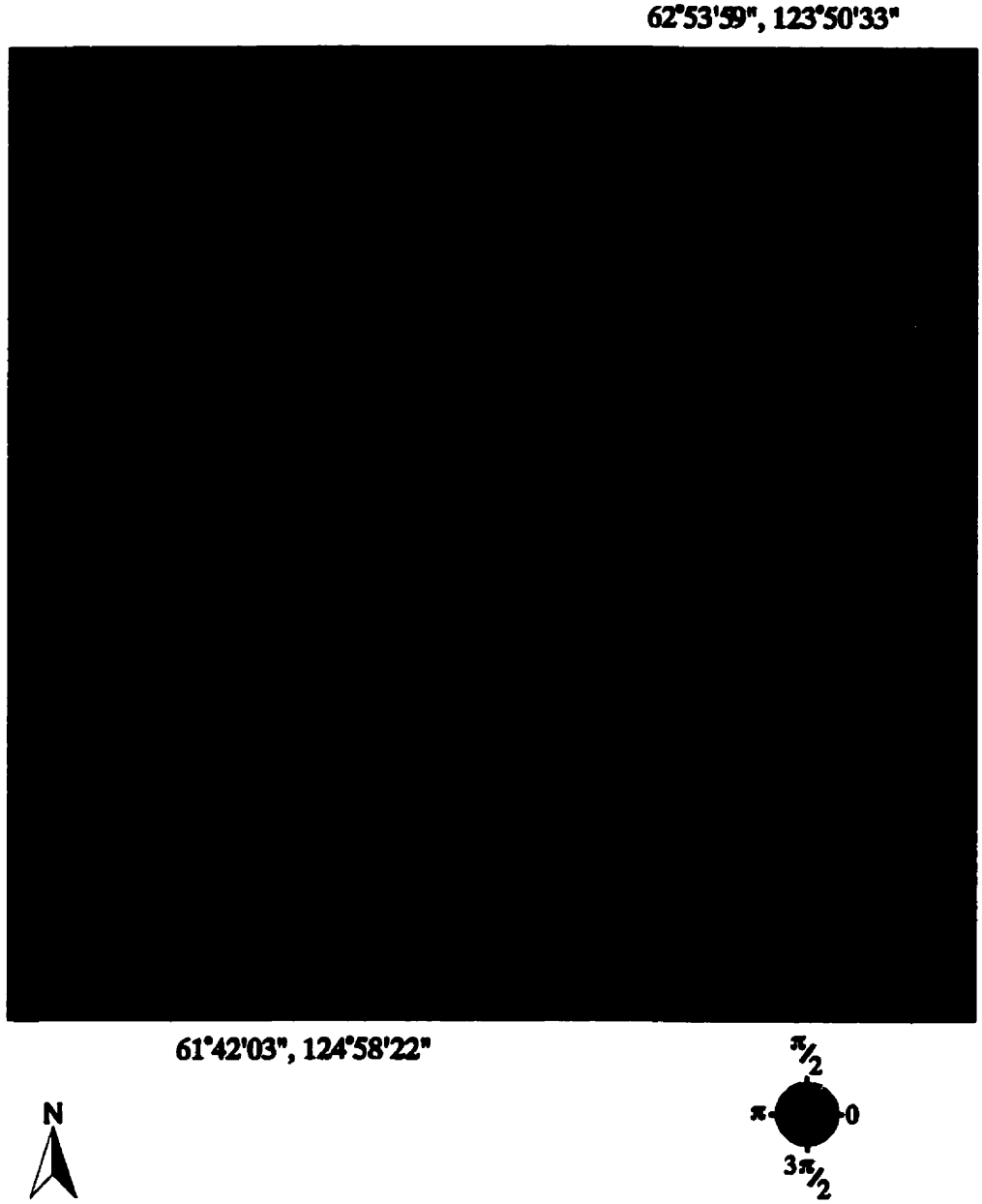

Figure 7.10 Interferogram created from the Aug. 12/Aug. 15, 1991 ERS-1 image pair.

ence levels, around 0.2, are lakes, rivers, and swamps or marshes. These areas have coherence levels around 0.15. The RADARSAT image pair has good coherence in some areas and poor coherence in others. The flat regions in the eastern and south-central parts of the image have coherence levels around 0.4 - 0.5. The coherence in the mountainous regions is particularly low for the RADARSAT pair. In the mountainous regions the coherence levels fall to around 0.1 or lower. The high coherence area in the northeastern part of the image is the North Nahanni River. Normally water exhibits low coherence but since the images were acquired in the winter the river would have been frozen which would account for the higher coherence levels. RADARSAT does not have a onboard global positioning system (GPS) and consequently the orbit determination is poor. The only times that its position is known precisely is during the orbit boosting periods and this is when images for interferometry studies must be ordered. Therefore images have to often times be acquired during periods when there is a much greater chance for temporal decorrelation.

As was mentioned in section 4.2.3 each phase fringe in the interferogram represents a relative change in elevation which depends on the wavelength, altitude, incidence angle, and baseline. Table 7.1 shows the change in elevation across each fringe, calculated using Equation 4.12, for the RADARSAT and the ERS-1 image pairs. For the RADARSAT pair one fringe (change in phase from 0 to 2π) equals a 19 m change in elevation, for the ERS-1 pair one fringe is equal to a change in elevation of 190 m. The RADARSAT interferogram has good fringes in the regions that correspond to regions of good coherence but in the mountain-

Platform	Repeat Period (days)	Altitude (km)	Perp. Baseline (m)	Incidence Angle	Wavelength	Change in Elevation (m)
RADARSAT	24	798	799.8	42.4°	5.6	19
ERS-1	3	785	46.0	23.4°	5.6	190

Table 7.1 Table showing the relative change in elevation that one fringe corresponds to for the RADARSAT and ERS-1 image pairs.

ous regions the interferogram is extremely noisy. The ERS-1 interferogram has good fringes across the entire interferogram.

It is readily apparent from Figures 7.7 and 7.9 that a portion of the western part of the ERS-1 image and DEM are missing. Figure 7.11 shows a visual representation of the associated true slant range/azimuth range values for the ERS-1 images. R_n is a fixed value and is the slant range distance from the first pixel in the image to the satellite antenna. If a height reference value is added e.g. +2000 m, then the whole generated DEM in true slant range space is effectively shifted up by 2000 metres if the original height reference was 0 m. This means that the image pixels mode to smaller slant range positions because the positions of the pixels are now closer to the satellite. Since the Atlantis InSAR package does not allow for a change in slant range offset R_n, the portion of the image, as well as the DEM, interferogram, etc., that should be at ranges small than R_n are lost (B. Armour, 1998, per. comm.). The same effect can also be seen along the eastern edge of the RADARSAT results although the problem is much less severe. This may be due to the larger incidence angle of the RADARSAT system compared with the ERS-1 system. The ERS-1 system, with its smaller incidence angle, also has some problems with layover and foreshortening effects in the mountainous regions. There were more problems with the phase unwrapping which accounts for the somewhat noisy appearance of the mountainous regions. RADARSAT did not have any significant problems with layover and foreshortening effects in the mountainous terrain.

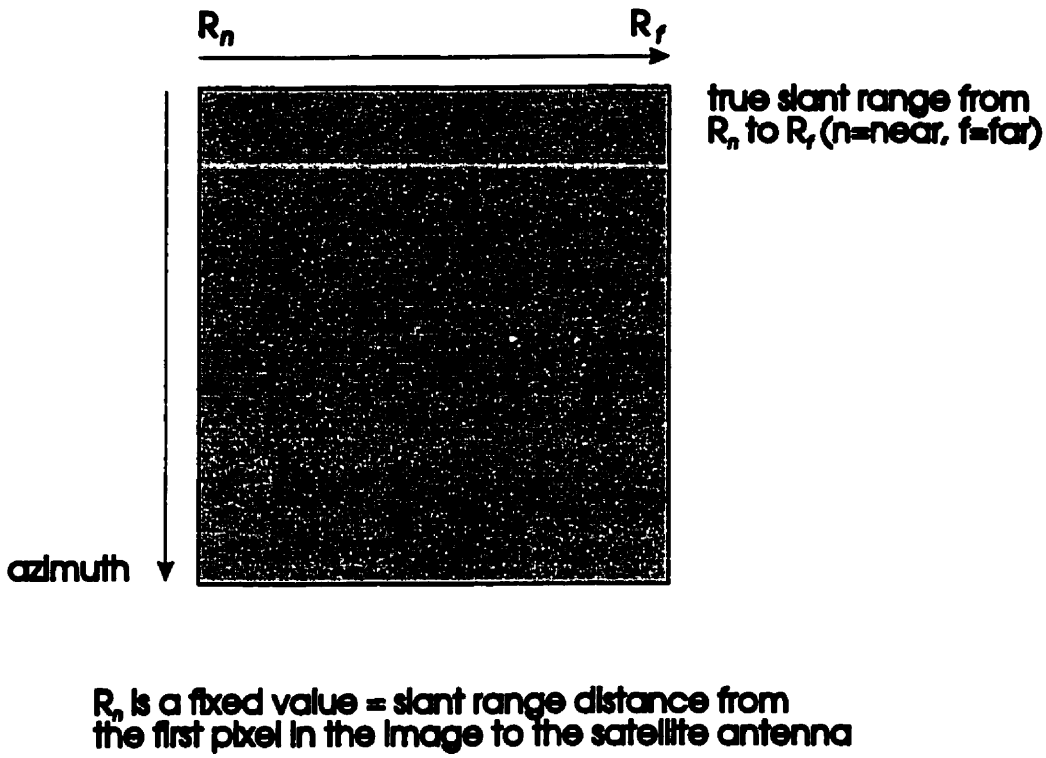

Figure 7.11 Visual representation of the associated true slant range/azimuth range values.

To analyze the quality of the DEM's two different methods, which are discussed in Zebker et. al. (1994), were used. The first method was to choose several control points from the DEM's and 1:50 000 topographic maps and compare the elevations and latitudes and longitudes of those points. The locations of the control points are shown in the master SAR image, DEM, and coherence image for the RADARSAT and ERS-1 image pairs. The results are shown in Table 7.2. The accuracy of this method is somewhat limited since it is difficult to find the same point in both the DEM's and the 1:50 000 maps.

The elevations from the map are approximately estimated by using interpolation between the 100 ft contours on the map. Therefore the elevation values taken from the map will not be very accurate. As a result it is not possible to reach any firm conclusions on the basis of these results. It is apparent however that the RADARSAT DEM is not accurate at all in the mountainous regions. The coherence for the RADARSAT images is much lower than for the ERS-1 images, particularly in the mountainous regions as can be seen by comparing Figures 7.3-7.6 with Figures 7.7-7.10. The low coherence areas should be masked out because the phase is not sufficiently correlated to produce accurate fringes. To reduce the amount of masked out area in the DEM, these areas were interpolated over. However, since the areas of higher coherence on either side of the mountainous regions are much flatter and lower in elevation, the interpolation is not very accurate. As a result the mountainous regions are interpreted to much lower than they really are.

The comparison method is useful however for determining the accuracy of the latitude/longitude coordinates for the six sites. In Table 7.3 the latitude and longitude coordinates

	Geomatics DEM			RADARSAT		
Site	Latitude	Longitude	Elevation (m)	Latitude	Longitude	Elevation (m)
1	62.25146°	124.30067°	509	62.25067°	124.28248°	473
2	62.24062°	124.29650°	509	62.23889°	124.28661°	590
3	62.25480°	124.35738°	524	62.25507°	124.36084°	511
4	62.29566°	124.46164°	1339	62.29216°	124.43589°	675
5	62.24145°	124.58924°	622	62.24119°	124.57941°	768
6	62.29900°	124.57089°	808	62.29289°	124.55793°	786
	ERS-1			MAP		
Site	Latitude	Longitude	Elevation (m)	Latitude	Longitude	Elevation (m)
1	62.24398°	124.27781°	606	62.2518°	124.2901°	533
2	62.23580°	124.28402°	515	62.2377°	124.2912°	533
3	62.25079°	124.36379°	441	62.2515°	124.3589°	533
4	62.29121°	124.45864°	1425	62.2949°	124.4598°	1219
5	62.23898°	124.56944°	815	62.2391°	124.5867°	570
6	62.29211°	124.56412°	802	62.2898°	124.5713°	716

Table 7.2 Latitude, longitude, and elevation values for the control points from the Geomatics DEM, RADARSAT DEM, ERS-1 DEM, and a 1:50 000 map. The site numbers correspond to those in Figure 7.3.

	Geomatics DEM		RADARSAT DEM		ERS-1 DEM	
Site	δ Latitude	δ Longitude	δ Latitude	δ Longitude	δ Latitude	δ Longitude
1	0.0003	0.0106	0.0011	0.0076	0.0078	0.0123
2	0.0029	0.0053	0.0012	0.0046	0.0019	0.0072
3	0.0033	0.0015	0.0036	0.0019	0.0007	0.0049
4	0.0008	0.0018	0.0027	0.0239	0.0559	0.0012
5	0.0024	0.0025	0.0021	0.0073	0.0001	0.0173
6	0.0092	0.0004	0.0031	0.0133	0.0023	0.0072

Table 7.3 Latitude and longitude differences between each of the DEM's and the 1:250 000 map. δ is the absolute value of the difference.

for each of the DEM's is compared with the latitude and longitude from the 1:50 000 maps. δ is simply the absolute value of the difference between the latitudes and longitudes. The δ latitude values are generally below 0.005^{o} and the δ longitude values are generally below 0.01^{o} which correspond to errors of around 500 m. This means that the latitude and longitude positions of each of the points is accurate to around 500 m. Considering that the pixel resolution is on the order of 20×20 m^2 and that it is generally not possible to be more accurate than a few pixels in picking a certain point on the DEM, this accuracy is quite good. Also on a map it is difficult to precisely measure the latitude and longitude of a particular point. The JPL Topographic SAR (TOPSAR) satellite has a accuracy of 50 - 100 m so the results obtained in this study is within an acceptable limit.

The second method used to compare the DEM's was to compute the statistical errors based on examination of points in flat areas to ascertain whether all the chosen points have the same elevation. This method only works for determining the elevation accuracy and not the latitude/longitude accuracy of the DEM's. In this case, three flat areas were chosen in the RADARSAT and ERS-1 DEM's and a number of points were chosen within those areas. The areas were a lake located in the southeastern part of the study area, along the top of the Iverson Range where the elevations are fairly constant, and along the North Nahanni River. The rms errors were then calculated to see how closely the elevations remained to a constant value. Table 7.4 shows the results of the rms calculations.

	Lake		Iverson Range		North Nahanni River	
Platform	**rms error (m)**	**coherence**	**rms error (m)**	**coherence**	**rms error (m)**	**coherence**
RADARSAT	2.606	0.33	17.481	0.09	2.887	0.65
ERS-1	5.090	0.20	5.169	0.92	3.259	0.32

Table 7.4 rms errors for the three flat areas chosen in the RADARSAT and ERS-1 images.

It would be expected that the area where the elevations would be the closest to being constant would be lake. The rms error for the RADARSAT DEM for the lake was 2.606 m and for the ERS-1 DEM it was 5.090 m. The coherence around the lake was approximately 0.33 for the RADARSAT images and 0.20 for the ERS-1 images. Zebker et. al., (1994) note that a coherence of 0.25 corresponds to a 7.5 m height error for ERS-1 images so the rms error obtained for the lake is comparable to what would be expected or better.

For the points chosen along the Iverson Range the ERS-1 DEM has almost the same rms error (5.169 m) as for the lake although the coherence is much higher (0.92). Zebker et. al. (1994) also note that areas with higher elevations tend to show a greater degree of height error which may account for this result. The rms error for the RADARSAT DEM is however much larger, 17.481 m. The much larger rms error for the RADARSAT DEM over the Iverson Range is most likely due to the coherence level being only 0.09 and the interpolation problem discussed above. Therefore elevations along the Iverson Range in the RADARSAT DEM are most likely not very accurate. For the third case, along the North Nahanni River, the RADARSAT DEM has a rms error of 2.887 m and a coherence level of 0.65. The ERS-1 DEM has a rms error of 3.259 m and a coherence level of 0.32. With the exception of the points in the RADARSAT DEM along the Iverson Range, the errors agree well with those of Zebker et. al., (1994) which were determined using ERS-1 images. These results show that it is possible to create topographic maps with errors of 5 m rms from interferometric data collected by ERS-1 or RADARSAT if the coherence is high enough. This ability would be especially useful in

areas such as the North Nahanni River area where there is little or no topographic information available.

7.3 Differential Interferograms

In this thesis both two-pass differential interferometry using ERS-1and RADARSAT imagery, and three-pass differential interferometry using ERS-1 imagery was carried out in order to detect surface displacement. There was also ERS-1/2 tandem mode imagery, acquired on Jan. 08, 1996 and Jan. 09, 1996, available which could have been used for two-pass differential interferometry. It was decided to use only ERS-1 data in order to better compare the two-pass and three-pass results. The spatial scale of surface deformation that it should be possible to measure is on the order of several centimetres.

7.3.1 Two-pass Differential InSAR

Two-pass differential interferometry was done using both ERS-1 and RADARSAT imagery. The ERS-1 images were acquired in late summer on Aug. 12, 1991 and Aug. 15, 1991 and the RADARSAT images were acquired in late winter on Feb. 19, 1998 and Mar. 15, 1998. To remove the topographic contribution a geocoded DEM provided by Geomatics Canada Centre for Topographic Information was used. The DEM is based on National Topographic System (NTS) maps at a scale of 1:250 000. This is the same DEM used in the

comparison in section 7.2 and shown in Figure 7.2. To co-register the DEM with the master SAR image a bias tiepoint must be marked on both as described in 5.2.7. Then a series of tie-points must be selected across the master SAR image and the synthetic SAR image using the procedure which was also described in 5.2.7. The bias tiepoint coordinates and co-registration tiepoints used for the ERS-1 calculation are listed in Table 7.5, and for the RADARSAT calculation they are listed in Table 7.6.

ERS-1 Results

The geocoded master SAR image for the Aug. 12, 1991 ERS-1 image is shown in Figure 7.12. The SAR image covered a larger surface area than the DEM so only a portion of the SAR image was used. The coordinates for the upper left and lower right corners are shown on the figure. The Iverson Range and the North Nahanni River are indicated on the image and the Iverson thrust fault runs along the east side of the Iverson Range. The western edge of the image shows the problem caused by a change in slant range distance as is discussed in Section 7.2. Figure 7.13 shows the coherence image obtained for the ERS-1 image pair, bright regions are areas of high coherence and dark regions are areas of low coherence. The ERS-1 pair has excellent coherence, > 0.8 in the flat regions and > 0.6 in the mountainous regions, across the entire area with only small, localized regions of lower coherence. The low coherence areas are lakes, rivers, and swamps or marshes and these have coherence levels of around 0.2.

Figure 7.14 shows the differential interferogram created from the ERS-1 pair and using the Geomatics Canada DEM to subtract the topographic contribution. Most of the topo-

Tiepoint Number	Master Image		DEM	
	Row	Column	Row	Column
bias point	753	4150	836	896
1	587	925	544	976
2	172	197	124	170
3	734	136	697	105
4	101	1810	89	1760
5	612	1610	582	1570
6	1180	1760	1150	1730
7	1210	1520	1180	1490
8	239	4390	219	4360
9	194	11300	172	11200
10	883	12500	848	12400
11	326	13000	296	12900
12	333	15700	311	15600
13	804	15800	785	15700
14	476	20500	444	20400
15	221	6940	200	6910

Table 7.5 Row and column coordinates for the bias point and tiepoints used to coregister the Aug. 12, 1991 ERS-1 master SAR image with the Geomatics DEM. The first point listed is the bias point and the remaining points are the tiepoints.

Tiepoint Number	Master Image		DEM	
	Row	Column	Row	Column
bias point	1620	4890	838	901
1	1650	4680	1540	4730
2	1630	4960	1480	5080
3	3290	5350	3160	5430
4	5190	5560	5040	5680
5	4580	5490	4430	5610
6	3570	2630	3440	2750
7	3540	3440	3390	3530
8	1460	2740	1350	2890
9	4720	2650	4590	2760
10	4700	7910	4540	8000
11	3170	8530	3010	8690
12	2040	8850	1860	8940

Table 7.6 Row and column coordinates for the bias point and tiepoints used to coregister the Feb. 19, 1998 RADARSAT master SAR image with the Geomatics DEM. The first point listed is the bias point and the remaining points are the tiepoints.

Figure 7.12 Geocoded master SAR image for the Aug. 12/Aug. 15, 1991 ERS-1 image pair. Coordinates for the upper right and lower left corners are shown.

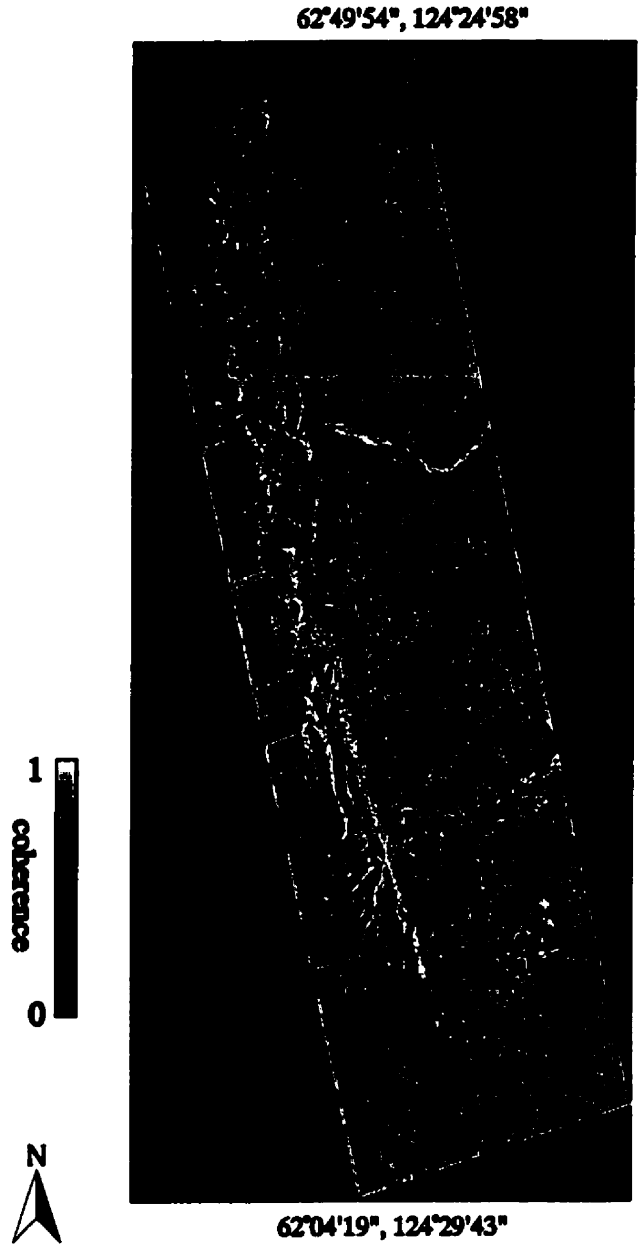

Figure 7.13 Coherence image for the Aug. 12/Aug. 15, 1991 ERS-1 image pair.

Figure 7.14 Differential interferogram for the Aug. 12/Aug. 15, 1991 ERS-1 image pair using the Geomatics DEM to remove the topographic contribution.

graphic effect has been removed from the interferogram however there are still some residual fringes left. The flat areas in the eastern part of the interferogram have a lower concentration of fringes than in the mountainous area in the western part. This is most likely due to the flat areas have a lower concentration of fringes before the topographic effect was removed. The residual fringes are mostly likely caused by the Geomatics DEM and the DEM created from the ERS-1 pair not matching exactly.

If the fringes were due to some type of surface deformation we would expect to see a concentrated fringe pattern instead of the random pattern that is present. However, ideally it would be expected that if there was no surface deformation there would be just a constant phase across the entire interferogram. No large earthquakes are known to have occurred over the time periods that the images were acquired. It is possible that if a large earthquake had occurred between the time periods that the two images were acquired that enough of the topographic effect may have been subtracted to make detection of the surface displacement possible. Meyer et. al., 1996 mapped surface displacements of > 50 cm caused by a M_s 6.6 normal earthquake in northern Greece while still having some residual fringes in the interferograms. In the Nahanni region the amount of displacement due to a large earthquake is likely comparable to previous studies so it should be possible to detect ground displacement. The residual fringe pattern may make it difficult though to accurately determine the amount of ground displacement.

RADARSAT Results

The geocoded master SAR image for the Feb. 19, 1998 RADARSAT image is shown in Figure 7.15. As was the case with the ERS-1 image, the RADARSAT image covered a larger surface area than the DEM so only a portion of the SAR image was used. The coordinates for the upper left and lower right corners are shown on the figure. The Iverson Range and the North Nahanni River are indicated on the image.

Figure 7.16 shows the coherence image obtained for the RADARSAT image pair, bright areas are areas of high coherence and dark areas are areas of low coherence. The coherence of the RADARSAT pair is much lower than for the ERS-1 pair with about equal areas of high and low coherence. The flat regions have coherence levels around 0.4 - 0.5 and the mountainous regions have coherence levels as low as 0.1. This was expected since the images were acquired in the winter and 24 days apart. However the coherence is still higher than was expected with some regions showing coherence as high as the ERS-1 pair. The area along the North Nahanni River has coherence levels of around 0.8 while some areas along the western edge have coherence levels around 0.6. This indicates that useful interferometry results are possible from RADARSAT imagery acquired in northern regions even when the images are acquired in the winter.

Figure 7.17 shows the differential interferogram created from the RADARSAT image pair using the Geomatics DEM to subtract the topographic contribution. Removing the topographic contribution can sometimes improve the coherence (B. Armour, 1998, per.

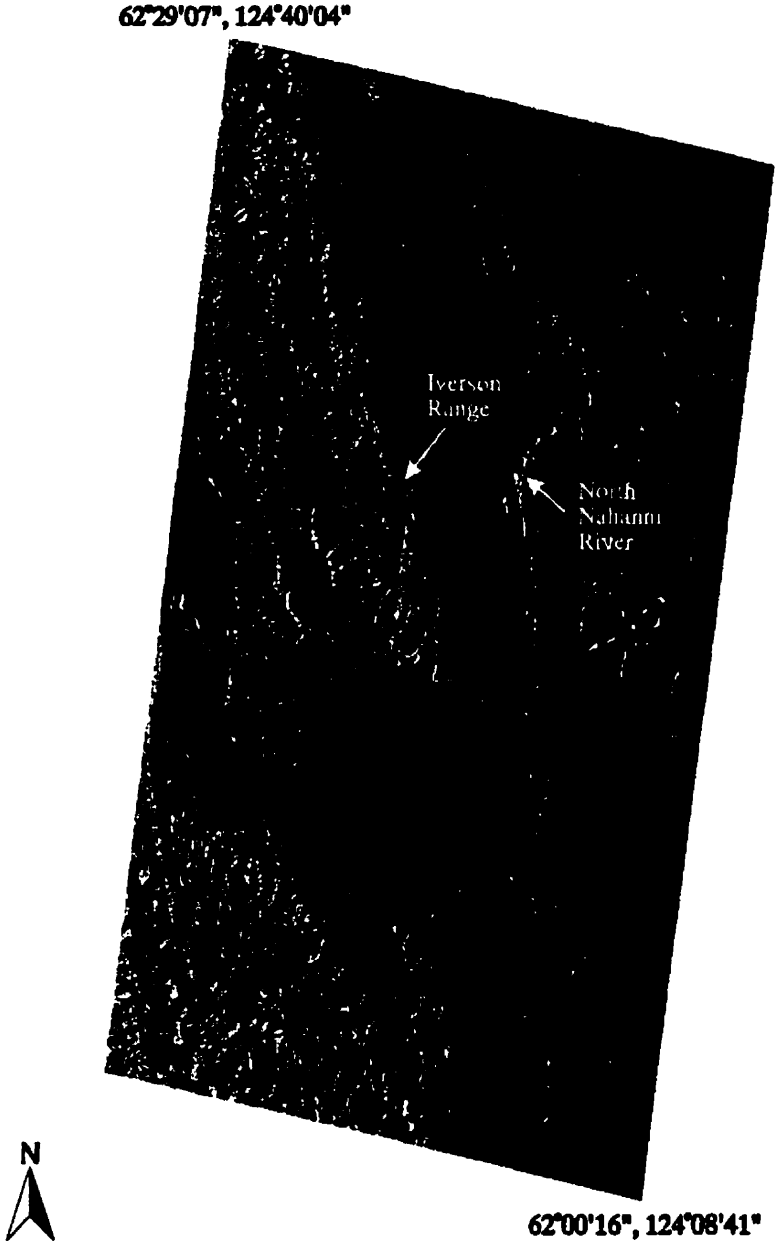

Figure 7.15 Geocoded master SAR image for the Feb. 19/Mar. 15, 1998 RADARSAT image pair. Coordinates for the upper right and lower left corners are shown.

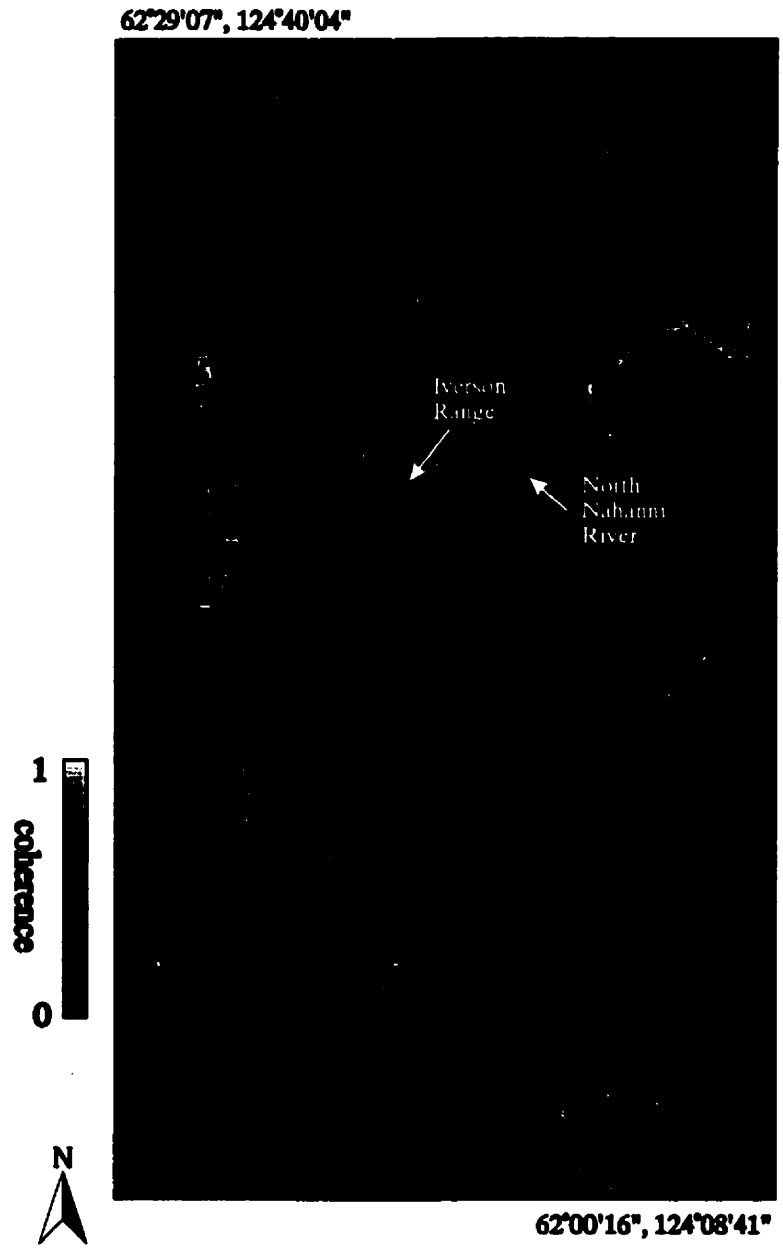

Figure 7.16 Coherence image for the Feb. 19/Mar. 15, 1998 RADARSAT image pair.

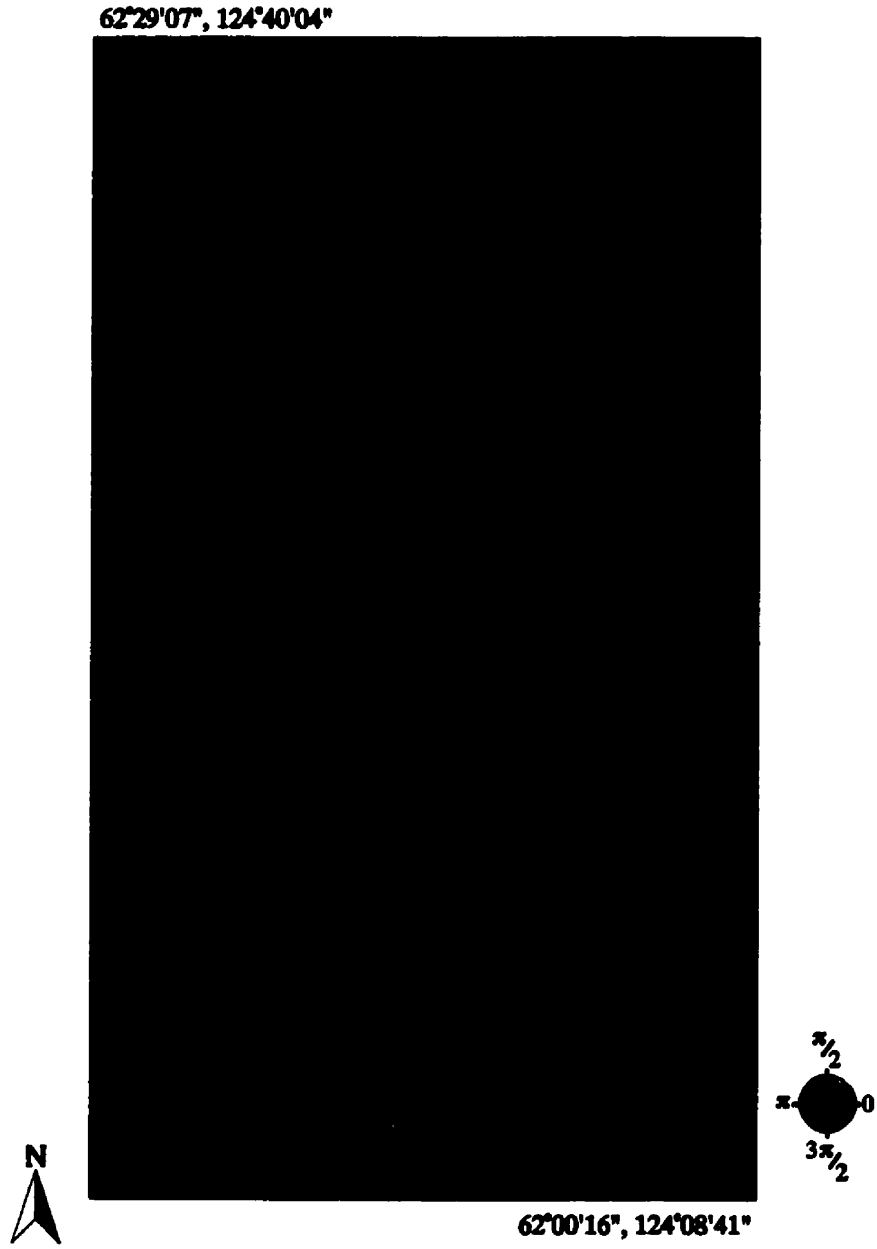

Figure 7.17 Differential interferogram for the Feb. 19/Mar. 15, 1998 RADARSAT image pair using the Geomatics DEM to remove the topographic contribution.

comm.) but it does not appear to have helped significantly in this situation. The black regions are areas that were masked out because the coherence was too low. The minimum coherence was set at 0.1. The interferogram contains quite a bit of noise, particularly in the mountainous regions in the western half of the interferogram, and a few fringes in the flat regions in the eastern half. In the low coherence regions the coherence is not high enough to generate coherent fringe patterns. This is why fringes are only observed in the high coherence regions. As was the case with the ERS-1 results, this is due to the Geomatics DEM and the DEM created from the RADARSAT pair not matching exactly. The low coherence in the RADARSAT pair is likely the cause of this problem. With better coherence it is possible that results would have been similar to those obtained for the ERS-1 images.

7.3.2 Three-pass Differential InSAR

Three-pass differential interferometry requires three SLC images where coherence is maintained over the time span in which all three images are acquired. For this thesis the images used were ERS-1 SLC images acquired on Aug. 12, 1991, Aug. 15, 1991, and Sep. 05, 1991. It was anticipated that since this period was in was late summer/early fall that there would be good coherence over this time span. To create the three-pass differential interferogram, the images acquired on Aug. 12 and Aug. 15 were used to create a DEM in slant range/ azimuth coordinates. This is the same DEM that was used in 7.2 for the DEM comparison. A differential interferogram was then created from the Aug. 12 and Sep. 05 pair, using the DEM created from the Aug. 12/Aug. 15 pair to remove the topographic contribution. This procedure

will have the effect of showing any ground displacement that occurred between Aug. 15 and Sep. 05 since any ground displacement that may have occurred between Aug. 12 and Aug. 15 will be cancelled out.

The master SAR image, coherence image, DEM, and interferogram for the Aug. 12/Aug. 15, 1991 image pair, can be seen in Figures 7.7-7.10. These have been discussed previously in 7.2. The coherence image for the Aug. 12/Sep. 05, 1991 differential image pair is shown in Figure 7.18. The coherence for this pair is significantly lower than for the Aug. 12/ Aug. 15, 1991 image pair. Typical coherence levels are near 0.1 with some isolated areas in the mountainous regions with coherence levels up to 0.5. The images were acquired 24 days apart during the late summer and early fall which will result in a much higher probability for temporal decorrelation. There most likely was significant changes in vegetation cover between the dates that the images were acquired i.e. leaves falling off trees, and grasses and other surface vegetation dying as winter approaches. The North Nahanni River and other rivers in the area have fairly high coherence which might be expected if the poor coherence is caused by vegetation changes. The higher coherence levels in the mountainous regions would likely due to these areas being above the tree line.

The differential interferogram for the Aug. 12/Sep. 05, 1991 image pair is shown in Figure 7.19. As a result of the low coherence between the two images there is not much useful information in the differential interferogram. As was the case with the RADARSAT image pair in 7.2, in order to decrease the amount of the image that is masked out the coherence thresholds were set lower (starting coherence = 0.15, final coherence = 0.11) and a larger inter-

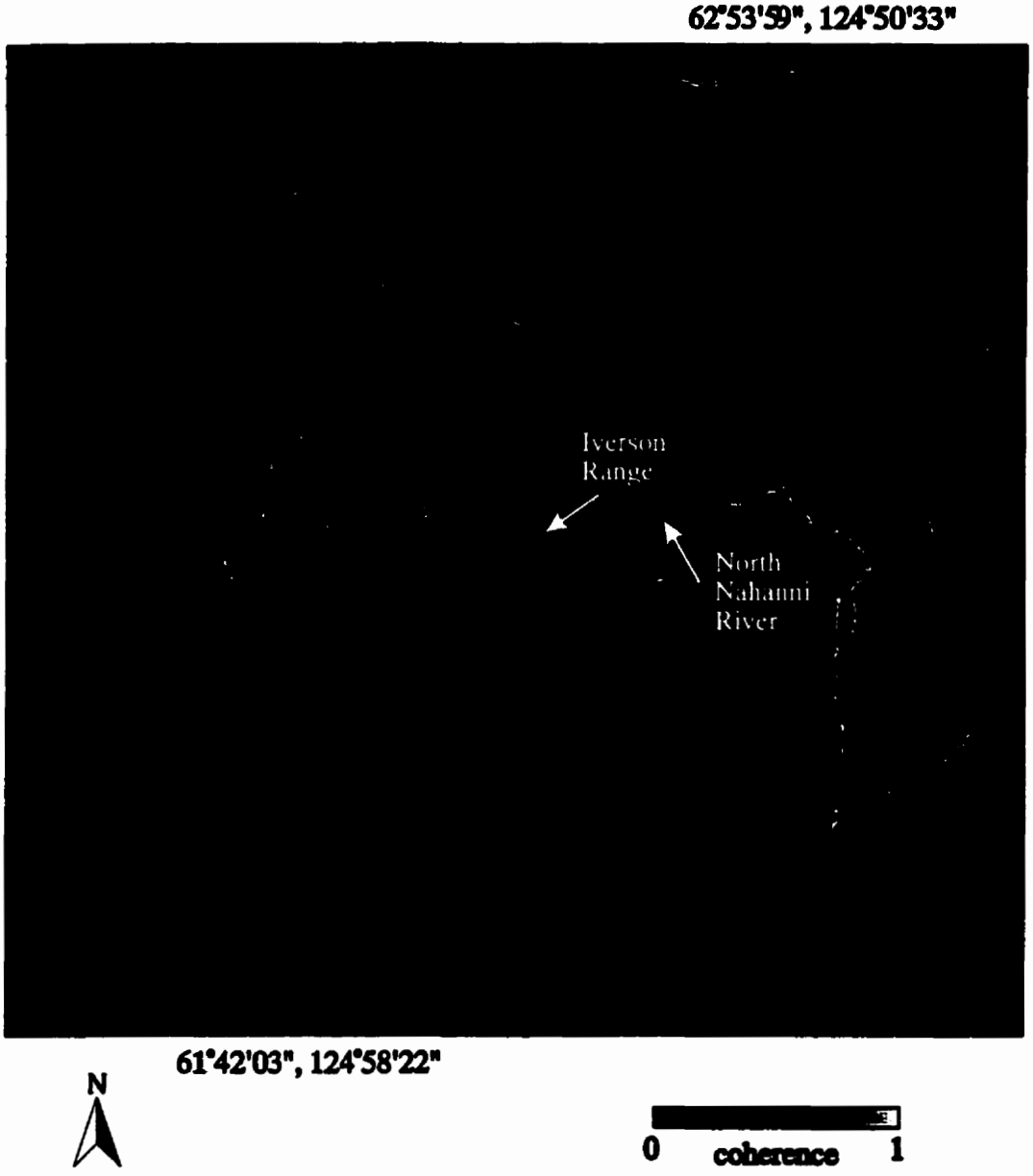

Figure 7.18 Coherence image for the Aug. 12/Sep. 05, 1991 ERS-1 image pair.

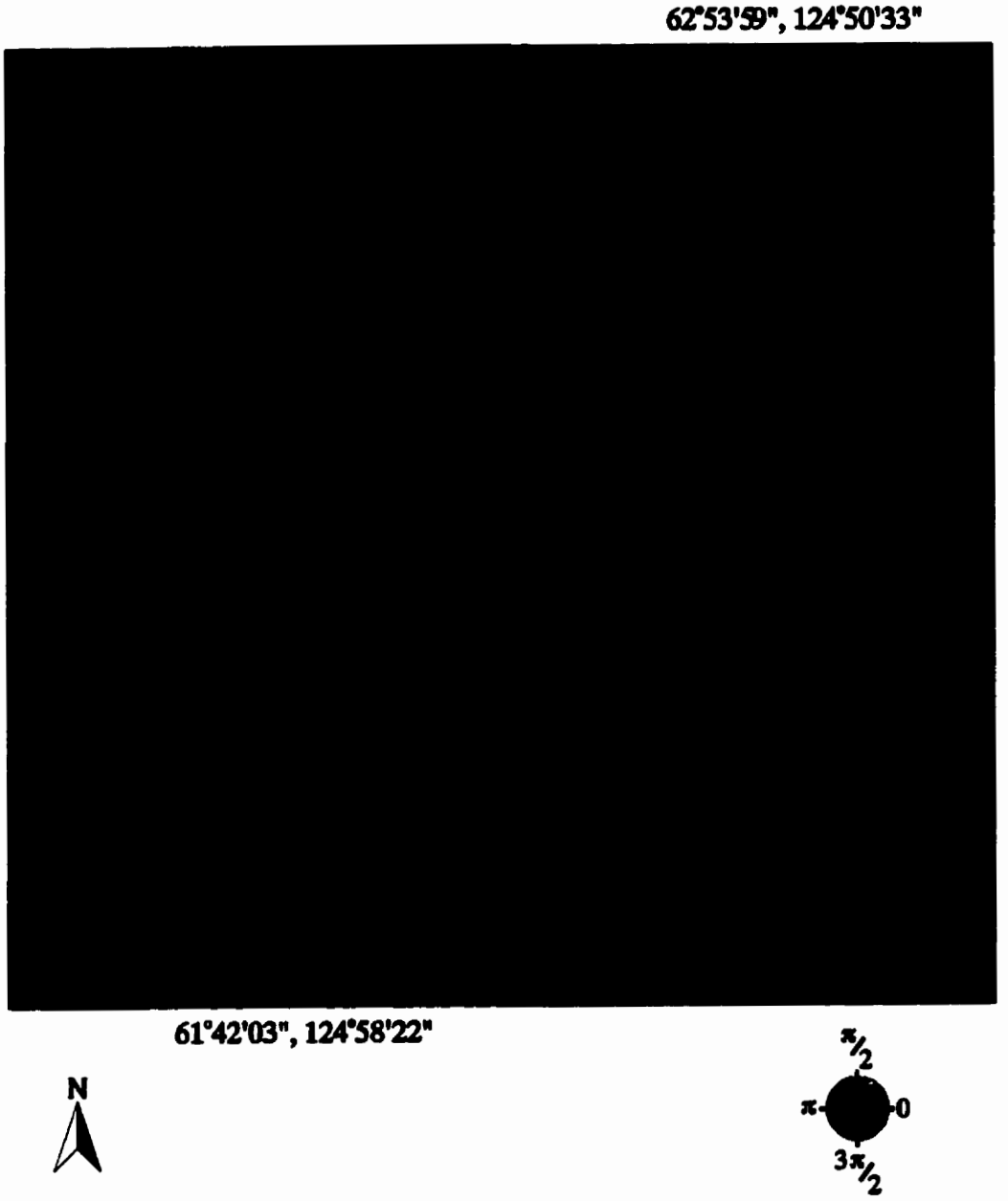

Figure 7.19 Differential interferogram for the Aug. 12/Sep. 05, 1991 ERS-1 image pair.

polation distance was used (300 pixels). This will lead to inaccuracies in the DEM similar to those seen for the RADARSAT pair in 7.2. As a result of having a poor DEM created from the Aug. 12/Sep. 05, 1991 image pair the topographic contribution will not be properly eliminated. As a result the differential interferogram appears extremely noisy and it is not possible to determine if there was any surface movement between the dates that the images were acquired. In fact it is unlikely that even if there had been a large earthquake that it would be possible to detect any surface displacement.

7.3.3 General Discussion of Differential InSAR Results

For this study there was a limited number of images available with many acquired under conditions that are not favorable for differential interferometry studies. For the two-pass differential InSAR cases if there had been a large earthquake between the time periods when two of the images were acquired it may have been possible to detect surface displacement. Enough of the topographic effect may have been subtracted to allow this result. For the three-pass differential InSAR case it is unlikely that detection of surface displacement would have been possible with the coherence being as low as it was, although difficult to draw significant conclusions on the basis of the data sets available. These results do show some encouraging signs since the coherence is high for some of the image pairs.

Massonnet et. al. (1993), Massonnet et. al. (1996), and a number of other groups, have carried out differential interferometry studies in strike-slip environments and Meyer et.

al. (1996) have mapped displacements due to earthquakes in normal faulting environments using differential interferometry. Displacements of 50 cm or more have been detected in these studies. The Meyer et. al., (1996) results show that displacements can be mapped in environments other than strike-slip faults. The Massonnet et. al. (1993) and Massonnet et. al. (1996) studies were carried out in rugged terrain in California showing that displacements can be mapped in mountainous areas as well as flat areas. The results from these previous studies, along with the results obtained in this thesis, show that further research into differential Interferometric studies in the Nahanni area would be valuable.

CHAPTER 8 Conclusions

This thesis examined the potential of SAR Interferometry to create DEM's and detect centimetre scale surface displacements in the Nahanni earthquake region. This method can be extremely valuable for studying active tectonic areas that are logistically difficult to access such as the Nahanni region.

The two SAR platforms that were used in this thesis were the Canadian RADARSAT (C-band) and the European ERS-1 (C-band). Both systems use the same wavelength but have different repeat periods and imaging incidence angles. RADARSAT utilizes a larger incidence angle which makes it superior for imaging in mountainous regions however its

repeat period of 24 days can lead to significant problems with coherence. ERS-1 has a repeat period of 3 days which is much more suitable for interferometry in terms of coherence but its smaller incidence angle can lead to phase unwrapping problems in mountainous terrain.

DEM's were created from RADARSAT images acquired on Feb. 19, 1998 and Mar. 15, 1998, and from ERS -1 images acquired on Aug. 12, 1991 and Aug. 15, 1991. These were compared with a DEM provided by Geomatics Canada Centre for Topographic Information and a 1:250 000 map of the Nahanni region. The two comparison methods used were 1.) to select several control points in each of the DEM's and the 1:50 000 map and compare the elevations and latitude/longitude coordinates and 2.) to compute the rms error over flat areas in the RADARSAT and ERS-1 DEM's and see how close the points remain to a constant value.

The latitude values were generally within 0.005^{o} of each other and the longitude values were within 0.01^{o} of each other. This corresponds to a error of around 500 m which is quite good considering the pixel resolution is 20×20 m^2 and it is generally not possible to be more accurate than a few pixels in picking a certain point on the DEM's. The rms errors for the flat areas were around 5 m or less in both the RADARSAT and ERS-1 DEM's when the coherence was around 0.20 or higher. This shows that it is possible to create DEM's with errors of 5 m rms from interferometric data collected by RADARSAT or ERS-1 if the coherence is high enough.

Both two-pass differential interferometry using ERS-1 and RADARSAT imagery and three-pass differential interferometry using ERS-1 imagery were attempted. For the two-

pass differential InSAR trials the Geomatics DEM was used to subtract the topographic contribution. The ERS-1 images used were acquired on Aug. 12, 1991 and Aug. 15, 1991 for the two-pass trial, and a third image acquired on Sep. 05, 1991 was used for the three-pass trial. The RADARSAT images used were acquired on Feb. 19, 1998 and Mar. 15, 1998.

It was possible to remove most of the topographic contribution for the ERS-1 trial but some residual fringes remained which were likely caused by poor matching of the Geomatics DEM and the DEM created from the ERS-1 pair. Enough of the topographic effect was removed however that if there had been surface displacement due to a large earthquake it may have been possible to detect it, although the residual fringe pattern may make it difficult to accurately determine the amount of ground displacement. The RADARSAT image pair had much lower coherence than the ERS-1 pair making it much more difficult to remove the topographic contribution. The RADARSAT differential interferogram contained a great deal of noise a few fringes. The fringes are also likely due to the Geomatics DEM and the RADARSAT DEM not matching exactly. The low coherence would make it difficult to detect surface displacement due to small earthquakes that my have occurred, but it may be possible to detect displacements due to a large earthquake e.g. $M_s > 6.0$. With better coherence it is possible that the results would have been comparable to those obtained for the ERS-1 images.

In the three-pass differential interferometry attempt there was extremely low coherence for the Aug. 12/Sep. 05, 1991 image pair. As a result of the low coherence it was not possible to obtain useful results. The low coherence results in a extremely noisy differential

interferogram where it is highly unlikely that it would be possible to determine any surface displacement even if a very large earthquake had occurred.

There was a limited number of images available for this study and many of them were acquired under conditions not favorable for interferometry. However, in some situations the coherence between images was still fairly high (0.6 or greater) which provided good quality DEM's and interferograms. This is an encouraging sign since the North Nahanni River region is a difficult region to access and satellite interferometry can provide a potentially inexpensive method of creating DEM's and continuous monitoring of remote regions that are prone to tectonic activity.

Investigation of earthquake related tectonics using space-borne SAR interferometry is a new approach and this thesis explored the methodological aspect of the technique. Some of the difficulties realized in this thesis include

- poor orbit determination of RADARSAT which limited the number of available images suitable for interferometry
- obtaining images with baselines appropriate for interferometry
- temporal decorrelation problems, particularly in the winter.

References

Adams, J., (1985), "Canadian crustal stress data: a compilation to 1985", *Earth Physics Branch Open-File Report 85-31*, 81 p.

Adams, J., and Basham, P.W., (1989), "The seismicity and seismotectonics of Canada east of the Cordillera", *Geoscience Canada*, **16**, 3-16.

Alaska SAR Facility, (1996), "Electromagnetic Spectrum, Radar Bands", <URL: http://www.asf.alaska.edu/reference_documents/datacenters_references/em_spectrum.html>, Oct., 11, 1996.

Alaska SAR Facility, (1997), "ASF SAR Processing Algorithm", <URL: http://www.asf.alaska.edu/reference_documents/datacenters_references/sar_processing.html>, May, 09, 1997.

Alaska SAR Facility, (1999), "ASF Data Products", <URL: http://www.asf.alaska.edu/daac_documents/avail_data.html#sar_complex_images>, July, 19, 1999.

Askne, J., and Hagberg, J.O., (1993), "Potential for interferometric SAR for classification of land surfaces", *Proceedings, 1993 International Geoscience and Remote Sensing Symposium (IGARSS '93)*, August 18-21, Tokyo, Japan, 985-987.

Avery, T.E., and Berlin, G.L., (1992), "Fundamentals or remote sensing and airphoto interpretation", 5th ed., *Macmillan Publishing Co., New York*, 472 p.

Bamler, R., and Schattler, B., (1993), "SAR data acquisition and image formation", *SAR Geocoding: Data and Systems*, (G. Schreier, ed.), chapter 3, pp 53-102, Herbert Wichmann Verlag Gmbh, Karsruhe, Germany.

Canadian Oil and Gas Lands Administration, unpublished data, 1969.

Cannon, P.J., (1980), "Applications of radar imagery to arctic and subarctic problems", *Radar Geology: An Assessment*, **JPL Publication 80-61**, Pasadena, California: Jet Propulsion Laboratory, 265-274.

Choy, G.L., and Boatwright, J., (1988), "Teleseismic and near-field analysis of the Nahanni earthquakes in the Northwest Territories, Canada", *Bulletin of the Seismological Society of America*, **78**, 1627-1652.

de Wit, R.E.C., Gronberg, E.C., Richards, W.B., and Richmond, W.O., (1973), "Tathlina Area, District of Mackenzie", *in* The Future Petroleum Provinces of Canada, (T.G. McCrosson, ed.), *Canadian Society of Petroleum Geologists*, **Memoir #1**, 187-212.

EarthView, (1996a), "Users Guide", version 1.0.2, Atlantis Scientific Group Inc., Ottawa, Ontario, Canada, 393 p.

EarthView, (1996b), InSAR User's Manual", version 1.0.2, Atlantis Scientific Systems Group Inc., Ottawa, Ontario, Canada, 156 p.

Frost, V.S., Stiles, J.A., Shanmugan, K.S., and Holtzman, J.C., (1982), "A model for radar images and its application to adaptive digital filtering of multiplicative noise", *IEEE Transactions on Pattern Analysis and Machine Intelligence*, **PAMI-4**, 157-165.

Gabriel, A.K., Goldstein, R.M., and Zebker, H.A., (1989), "Mapping small elevation changes over large areas: differential radar interferometry", *Journal of Geophysical Research*, **94**, 9183-9191.

Goldstein, R.M., Engelhardt, H., Kamb, B., and Frolich, R.M., (1993), "Satellite radar interferometry for monitoring ice sheet motion: application to an Antarctic ice stream", *Science*, **262**, 1525-1530

Goldstein, R.M., Zebker, H.A., and Werner, C.L., (1988), "Satellite radar interferometry: two-dimensional phase unwrapping", *Radio Science*,**23**, 713-720.

Graham, L.C., (1974), "Synthetic interferometer radar for topographic mapping", *Proceedings of the IEEE*, **62**, 763-768.

Gray, A.L., and Farris-Manning, P.J., (1993), "Repeat-pass interferometry with airborne synthetic aperture radar", *IEEE Transactions on Geoscience and Remote Sensing*, **31**, 180-191.

Hagberg, J.O., Ulander, L.M.H., and Askne, J., (1995), "Repeat-pass SAR interferometry over forested terrain", *IEEE Transactions on Geoscience and Remote Sensing*, **33**, 331-340.

Harger, R.O., (1970), "Synthetic Aperture Radar Systems: Theory and Design", Academic Press, New York, 240 p.

Herron, E.M., Dewey, J.F., and Pitman, W.C., III, (1974), "Plate tectonic model for the evolution of the Arctic", *Geology*, **2**, 377-380.

Horner, R.B., Wetmiller, R.J., Lamontagne, M., and Plouffe, M., (1990), "A fault model for the Nahanni earthquakes from aftershock studies", *Bulletin of the Seismological Society of America*, **80**, 1553-1570.

Just, D., Adam, N., Schwabisch, M., and Bamler, R., (1995), "Comparison of phase unwrapping algorithms for SAR interferograms", *Proc. IGARSS '95*, Firenze, Italy, 767-769.

Just, D., and Bamler, R., (1994), "Phase statistics of interferograms with applications to synthetic aperture radar", *IEEE Transactions on Geoscience and Remote Sensing*, **31**, 180-191.

Koyama, J., (1997), "The complex faulting process of earthquakes", Kluwer Academic Publishers, The Netherlands, 194 p.

Lay, T., and Wallace, T.C., (1995), "Modern Global Seismology", Academic Press Inc., San Diego, 521 p.

Leblanc, G., and Wetmiller, R.J., (1974), "An evaluation of seismological data available for the Yukon Territory and Mackenzie Valley", *Canadian Journal of Earth Science*, **11**, 1435-1454.

Lee, J.S., (1981), "Refined filtering of image noise using local statistics", *Computer Graphics and Image Processing*, **15**, 380-389.

Lewis, D., (1976), "Geoscience applications of imaging radar systems", *Remote Sensing of the Electromagnetic Spectrum*, **vol. 3**.

Li, B., (1993), "Application of remote sensing techniques for the seismo-tectonic study of Nahanni earthquake area", M.Sc. Thesis, the University of Manitoba.

Lillesand, T.M., and Kiefer, R.W., (1994), "Remote sensing and image interpretation", 3rd ed., John Wiley & Sons Inc., New York, 750 p.

Lopes, A., Touzi, R., and Nezry, E., (1990), "Adaptive speckle filters and scene heterogeneity", *IEEE Transactions on Geoscience and Remote Sensing*, **28**, 992-100.

Lowman, P.D., Jr., (1976), "Geological structures in California: three studies with Landsat-1 imagery", *California Geology*, **29**, 75-81.

Lowman, P.D., Jr., McDivitt, J.A., and White, E.H., II, (1967), "Terrain photography on the Gemini IV mission, preliminary report", *NASA Technical Note D-3982*.

Massonnet, D., (1997), "Satellite radar interferometry", *Scientific American*, **Feb. 1997**, 46-53.

Massonnet, D., Briole, P., and Arnaud, A., (1995), "Deflation of Mt. Etna monitored by space-borne radar interometry", *Nature*, **375**, 567-570.

Massonnet, D., and Feigl, K.L., (1995), "Satellite radar interferometric map of the coseismic deformation field of the M = 6.1 Eureka Valley, California earthquake of May 17, 1993", *Geophysical Research Letters*, **22**, 1541-1544.

Massonnet, D., Feigl, K.L., Vadon, H., and Rossi, M., (1996), "Coseismic deformation field of the M = 6.7 Northridge, California earthquake of January 17, 1994 recorded by two radar satellites using interferometry", *Geophysical Research Letters*, **23**, 969-972.

Massonnet, D., Rossi, M., Carmona, C., Adragna, A., Peltzer, G., Feigl, K.L., and Rabaute, T., (1993), "The displacement field of the Landers earthquake mapped by radar interferometry", *Nature*, **364**, 138-142.

McCauley, J.F., Schaber, G.G., Breed, C.S., Grolier, M.J., Haynes, C.V., Issawi, B., Elachi, C., and Blom, R., (1982), "Subsurface valleys and geoarchaeology of the Eastern Sahara revealed by shuttle radar", *Science*, **218**, 1004-1019.

Meyer, B., Armigo, R., Massonnet, D., de Chabalier, J.B., Delacourt, C., Ruegg, J.C., Achache, J., Briole, P., and Papanastassiou, D., (1996), "The 1995 Grevena (Northern Greece) earthquake: fault model constrained with tectonic observations and SAR interferometry", *Geophysical Research Letters*, **23**, 2677-2680.

Moon, W.M., Won, J.S., Li, B., Slaney, V.R., and Lamontagne, M., (1991), "Application of airborne C-SAR and SPOT image data to the geological setting of the Nahanni earthquake area", *Canadian Journal of Remote Sensing*, **17**, 272-278.

O'Leary, D., Friedman, J.D., and Pohn, H.A., (1976), "Lineament, linear, and lineation: some proposed new standards for old terms", *Geological Society of America Bulletin*, **87**, 1463-1469.

PCIWorks, (1997), version 6.2, PCI, Richmond Hill, Ontario, Canada.

Peltzer, G., and Rosen, P., (1995), "Surface displacement of the 17 May 1993 Eureka Valley, California, earthquake observed by SAR interferometry", *Science*, **268**, 1333-1336.

Prati, C., and Rocca, F., (1990), "Limits to the resolution of elevation maps from stero SAR images", *International Journal of Remote Sensing*, **11**, 2215-2235.

Pritt, M.D., (1995), "Multigrid phase unwrapping for interferometric SAR", *Proc. IGARSS '95*, Fierenze, Italy, 562-564.

Reid, H.F., (1911), "The elastic-rebound theory of earthquakes", *University of California Publ. Geol. Sci.*, **6**, 413-444.

Richards, J.A., (1986), "Remote sensing digital image analysis: an introduction", 281 p.

Rogers, G.C., and Ellis, R.M., (1979), "The eastern British Columbia earthquake of Ferbruary 4, 1918", *Canadian Journal of Earth Science*, **15**, 1484-1493.

Scholz, C., (1990), "The mechanics of earthquakes and faulting", Cambridge University Press, Cambridge, 439 p.

Scholz, C.H., Sykes, L.R., and Aggarwal, Y.P., (1973), "Earthquake prediction: a physical basis", *Science*, **181**, 803-810.

Shi, Z., and Fung, K.B., (1994), "A comparison of digital speckle filters", *Proceedings of IGARSS '94*, 2129-2133.

Skolnik, M.I., (1980), "Introduction to Radar Systems", 2nd ed., McGraw-Hill Inc., New York, 581 p.

Stacey, F.D., (1992), "Physics of the earth", 3rd ed., Brookfield Press, Brisbane, 513 p.

Ulander, L.M.H., and Hagberg, J.O., (1993), "Use of InSAR for radiometric calibration over sloping terrain", *CEOS SAR Calibration Workshop Proceedings*, Sept. 20-24, ESTEC, ESA, WPP-048, Noordwijk, The Netherlands, 147-159.

Vachon, P.W., Geudtner, D., Gray, A.L., and Touzi, R., (1995), "ERS-1 synthetic aperture radar repeat-pass interferometry studies: implications for RADARSAT", *Canadian Journal of Remote Sensing*, **21**, 441-454.

Vachon, P.W., Geudtner, D., Mattar, K., Gray, A.L., Brugman, M., and Cumming, I., (1996), "Differential SAR interferometry measurements of Athabasca and Saskatchewan glacier flow rate", *Canadian Journal of Remote Sensing*, **22**, 287-296.

Wehner, D.R., (1987), "High Resolution Radar", Artech House, Norwood, MA, 472 p.

Wetmiller, R.J., Drysdale, J.A., Horner, R.B., and Lamontagne, M., (1989), "Canadian earthquakes - 1985-1986", *Geological Survey of Canada Paper 88-14*, **Seismological Series Number 97**.

Wetmiller, R.J., Horner, R.B., Hasegawa, H.S., North, R.G., Lamontagne, M., Weichert, D.H., and Evans, S.G., (1988), "An analysis of the 1985 Nahanni earthquakes", *Bulletin of the Seismological Society of America*, **78**, 590-616.

Wheeler, J.O., and Gabrielse, H., (1972), "The Cordilleran structural province", *in* Variations in Tectonic Styles in Canada, Price, R.A., and Douglas, R.J.W., ed., *Geological Association of Canada, Special Paper 11*, 81 p.

Wu, P., and Hasegawa, H.S., (1996), "Induced stresses and fault potential in eastern Canada due to a realistic load: a preliminary analysis", *Geophysical Journal International*, **127**, 215-229.

Zebker, H.A., and Goldstein, R.M., (1986), "Topographic mapping from interferometric synthetic aperture radar observations", *Journal of Geophysical Research*, **91**, 4993-4999.

Zebker, H.A., and Villasenor, J., (1992), "Decorrelation in interferometric radar echoes", *IEEE Transactions on Geoscience and Remote Sensing*, **30**, 950-959.

Zebker, H.A., Werner, C.L., Rosen, P.A., and Hensley, S., (1994), "Accuracy of topographic maps derived from ERS-1 interferometric radar", *IEEE Transactions on Geoscience and Remote Sensing*, **32**, 823-836.

Publications

Ristau, J.P., and Moon. W.M., (submitted), "Adaptive filtering of random noise in 2-D geophysical data", *Geophysics*.

Ferguson, I.J., Ristau, J.P., Maris, V.G., and Hosain, I., (1999), "Geophysical imaging of a kaolinite deposit at Sylvan, Manitoba, Canada", *Journal of Applied Geophysics*, **41**, 105-129.

Moon, W.M., Ristau, J., and Vachon, P., (1998), "Feasibility of applying space-borne SAR interferometry for earthquake tectonic investigation", *Geoscience Journal*, **2**, 78-87.

Hosain, I.T., Ferguson, I., Ristau, J., and Cassels, J., (1995), "Geophysical surveys for kaolin - Sylvan area, Manitoba", Report of Activities 1995, *Manitoba Energy and Mines*, Geological Services, 140-147.

Conference Abstracts

Ristau, J.P., Moon, W.M., and Vachon, P.W., (1998), Differential SAR interferometry for earthquake tectonic study", Geological Association of Canada Abstract Volume, Geological Association of Canada, A-156.

Moon, W.M., Ristau, J., Singhroy, V., Yamaguchi, Y., Lamontagne, M., and Kuoda, R., (1997), "Integrated imaging of RADARSAT and other SAR data for earthquake tectonic investigation of the Nahanni earthquake area in Northwest Territories, Canada", *International Association of Seismology and Physics of the Earth's Interior.*

Ristau, J.P., and Moon, W.M., (1997), "Digital filtering of 2-D spatial data using modified local statistics", 23rd Annual Scientific Meeting of the CGU, Canadian Geophysical Union, Program and Abstracts, 44.

Ristau, J.P., and Moon, W.M., (1997), "Digital filtering using modified local statistics", CSEG National Convention, Canadian Society of Exploration Geophysicists, Technical Abstract Book, 218-219.

Moon, W.M., Ristau, J., Yamaguchi, Y., and Singhroy, V.., (1997), "Tectonic investigation of Nahanni earthquake area NWT, using space-borne SAR (synthetic aperture radar)", 23rd Annual Scientific Meeting of the CGU, Canadian Geophysical Union, Program and Abstracts, 39.

Moon, W.M., Ristau, J.P., Vachon, P., Tanaka, A., and Yamaguchi, Y., (1997), "Investigation of Nahanni earthquake tectonics using space-borne SAR techniques", Proceedings, 2nd International InSAR Workshop, Tsukuba, Japan, Nov. 1997.